University of Nottingham



School of Mathematical Sciences

Inertial Effects on Thin-Film Wave Structures with Imposed Surface Shear

Mithilan Sivapuratharasu, BSc (Hons), MSc

A thesis submitted to The University of Nottingham for the degree of

Doctor of Philosophy

2017

In memory of the late Henry Power - professor, mentor and friend.

Abstract

This thesis provides a depth-averaged analytical and numerical approach to the mathematical simulation of thin-film flow on a flat inclined plane relevant to gravity-driven flows subject to high surface shear. Motivated by modelling thin-film structures within an industrial context, wave structures are investigated for flows with moderate inertial effects and small film depth aspect ratio ε. Approximations are made assuming a Reynolds number, Re $\sim \mathcal{O}\left(\frac{1}{\varepsilon}\right)$ and a depth-averaged approach used to simplify the governing Navier-Stokes equations. A classical, parallel, Stokes flow is expected in the absence of any wave disturbance based on a local quadratic profile; in this work a generalised approach, which includes inertial effects, is solved.

Flow structures are identified and compared with studies for Stokes flow in the limit of negligible inertial effects. Both two-tier and three-tier wave disturbances are constructed to study film profile evolution subject to shear at the free surface. An evaluation of film profiles is given from a parametric study for wave disturbances with increasing film Reynolds number. An evaluation of standing wave and transient film profiles is undertaken which identifies new profiles not previously predicted when inertial effects are neglected. A revised integral boundary layer model incorporating a more general cubic velocity profile is also introduced, to better capture fluid recirculation associated with a capillary region, and is developed to provide a better understanding of the internal flow dynamics within the thin-film layer. Notably, the wavelength and amplitude of the capillary ripples are analysed.

The effect of the boundary conditions between the fluid and the plane is undertaken to simulate slip properties of various substrates over which the fluid may flow. A Navier slip condition is proposed at this boundary and its effect on the wave structure is examined both with and without

the inclusion of inertia. The corresponding film dynamics are analysed with increased slip at the fluid-plane boundary and the effect on the wave structures formed are discussed.

In a subsequent chapter solitary wave structures are investigated through a study of gravity-driven flow structures as associated with an oscillating inlet. The effects of increasing the film Reynolds number of these flows is evaluated together with an investigation of the stability characteristics relevant to inlet frequency and inertial effects. The effect of surface shear on solitary waves is examined, both as a stabilising and a destabilising factor on perturbations introduced at the inlet. A final section provides an overview of the outcomes from this study.

Acknowledgements

First and foremost, I would like to show my appreciation for the invaluable guidance and immeasurable time my supervisors Stephen Hibberd, Matthew Hubbard and the late Henry Power at the University of Nottingham have invested in this research. I would also like to acknowledge the many teachers of mathematics who have inspired me to study this subject, including the late Andrew Cliffe.

This PhD was carried out at the University Technology Centre within the Gas Turbine and Transmissions Research Centre and I would like to thank Rolls Royce plc for their financial support. I would also like to thank the University of Nottingham for access to their High Performance Computing Facility.

My very profound gratitude goes to my parents and my family for providing me with unfailing support throughout my years of study. Finally, to my beloved fiancée Neera, for her endless encouragement and support, and for keeping me sane through the process of researching and writing this thesis. This accomplishment would not have been possible without you. Thank you.

CONTENTS

Nomenclature vii

1 INTRODUCTION 1
- 1.1 The motivation for this study 1
- 1.2 Review of thin-film modelling literature 5
- 1.3 Overview of the thesis 19

2 THIN-FILM MODEL FORMULATION INCLUDING INERTIAL EFFECTS 22
- 2.1 Nusselt solutions for uniform flow on an inclined plane . . . 26
- 2.2 Thin-film flow at moderate Reynolds numbers 27
- 2.3 An integral boundary layer model 28
- 2.4 Numerical methods 31
  - 2.4.1 Initial and boundary conditions 32
  - 2.4.2 Finite difference method 34
  - 2.4.3 Transient solver 37

3 INERTIAL EFFECTS ON SHEAR-DRIVEN FILM FLOW 40
- 3.1 Film evolution equations using a quadratic velocity profile . . 40
- 3.2 Classification of film profiles 45
- 3.3 Shear-driven film profiles using a quadratic velocity profile . 46
  - 3.3.1 Smoothing effects of inertia 48
  - 3.3.2 Formation of new fronts 59
  - 3.3.3 Near-vertical film profiles 63
- 3.4 Film evolution equations using a cubic velocity profile 69
  - 3.4.1 Shear-driven film profiles using a cubic velocity profile 71
- 3.5 Overview of the chapter 83

4 SHEAR-DRIVEN FLOW WITH A NAVIER SLIP BOUNDARY CONDITION 86
4.1 Modelling slip flow 89
4.1.1 Film profiles from multiple Nusselt solutions 90
4.1.2 Film profiles from a single Nusselt solution 98
4.2 Overview of the chapter 106

5 MODELLING OF SOLITARY WAVES ON AN INCLINED PLANE 108
5.1 Validation and comparison with experimental profiles 111
5.2 Effects of increasing Reynolds number of solitary waves . . . 118
5.3 Stability characteristics of solitary waves 126
5.4 Shear-imposed solitary waves 132
5.5 Overview of the chapter 137

6 THESIS SUMMARY, CONCLUSIONS AND FUTURE WORK 140

A ANALYTICAL JACOBIAN FORMULATION 148

Bibliography 155

NOMENCLATURE

α	Dimensionless slip length
λ	Dimensionless gravitational parameter
μ	Fluid viscosity
Ca	Capillary number
Re	Film Reynolds number
Re^*	Reduced Reynolds number
ρ	Fluid density
σ	Coefficient of surface tension
τ	Surface shear
θ	Angle of plane inclination
ε	Depth-aspect ratio
g	Gravitational acceleration
h	Film depth
h_1	Lowest Nusselt height
h_2	Intermediate Nusselt height
h_3	Highest Nusselt height
h_l	Height of film at the left hand side of the domain
h_m	Height of film in the central tier of the initial profile (if applicable)

h_r Height of film at the right hand side of the domain

p Fluid pressure

p_a Atmospheric pressure

q Fluid flux

t Time

u Fluid velocity parallel to the plane

v Fluid velocity perpendicular to the plane

x Coordinate direction parallel to the plane

y Coordinate direction perpendicular to the plane

1

INTRODUCTION

This introduction provides the industrial context behind the modelling process associated with an aerospace application together with an overview of the corresponding modelling strategy adopted. Relevant studies of thin-film modelling are identified, including alternative strategies adopted by other authors. An outline is given into the modelling approach adopted in this thesis and the structure of the thesis.

1.1 THE MOTIVATION FOR THIS STUDY

Oil films on the internal surfaces of an aeroengine bearing chamber are a primary mechanism in removing heat from the chamber as oil is continuously collected, externally cooled and recycled. The research undertaken was informed based on collaboration with Rolls-Royce plc. through the University of Nottingham Technology Centre within the Gas Turbine and Transmissions Research Centre (G2TRC). Ongoing research is linked to the development of the next generation of engines, with a view to understanding and overcoming the associated transmission challenges though the validation and demonstration of numerical models. Outcomes obtained will be transferred for use in informing further design. Mathematical models and subsequent numerical implementation play a vital role in the accurate simulation of thin-film wave structures in an aeroengine environment. Research carried out within the G2TRC informs optimal engine heat management

and cooling, reducing transmission power losses and improving engine efficiency. Continued development of mathematical models and testing of new configurations can inform future engine core architectures. Current issues include the greening of air transport and the competitiveness of the sector.

A generic bearing chamber is that of the Rolls-Royce Trent series, schematics of which are shown in figures 1 and 2. A simplified aeroengine bearing chamber consists of two rotating shafts, a high speed intermediate pressures (IP) shaft, rotating at speeds of up to 7000rpm, surrounding by an outer cylinder wall, known as the high pressure (HP), shaft which itself may rotate at up to 10000 rpm [56]. Oil is present in the chamber to act as a lubricant for the bearings as well as a coolant for the hot metal surfaces. The motion of an oil film within the bearing chamber is influenced strongly by a shearing airflow created through the rotation on the inner shaft, and so investigation of shear-driven flow is integral to this thesis in order to gain a better understanding the dynamics of the oil film. Of particular interest is the formation and evolution of wave structures within the oil film present on the inside of the outer shaft, acting as a cylinder wall, since dry or stagnant patches may leading to overheating, and in extreme cases lead to coking on the bearing chamber walls [56].

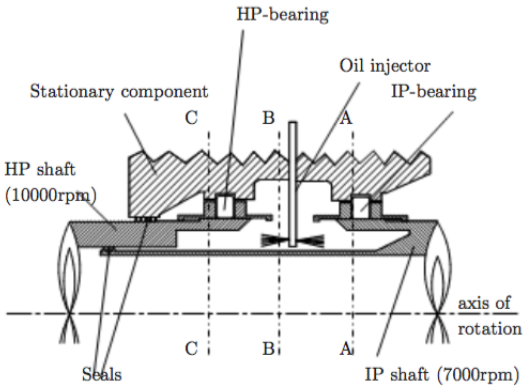


Figure 1.: Schematic of a section of the Trent 800 aeroengine bearing chamber [56].

The radius of the bearing chamber is approximately 180mm [11]. The thickness of the oil film for a high speed shaft motion ranges from 0.6mm

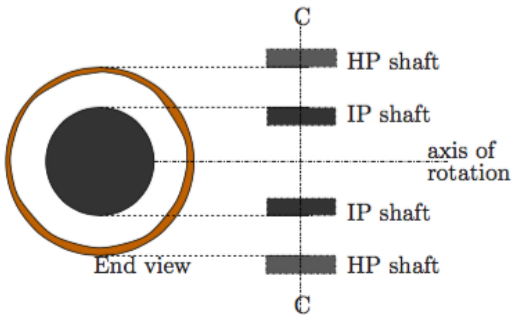


Figure 2.: Formation of oil film on the outer cylinder between the rotating shafts [56].

to 1.5mm; lower shaft speeds within the bearing chamber lead to increased film thickness [20]. A comparison of film thickness to shaft radius prompts the flow to be investigated locally as a thin film on an inclined plane. Such a plane can be considered tangential to a point on the surface of the bearing chamber, with variable angle of inclination. A parameter $\varepsilon \ll 1$ is assumed for the ratio film thickness to typical geometric length scale of disturbances of the flow.

Additionally within a bearing chamber the film flow may be subject to a strong shear air flow. The film velocity in the direction perpendicular to the plane is generally much smaller than the circumferential flow velocity along the plane, typically driven by the rapidly rotating IP engine shaft. In an experimental chamber test rig detailed by Gorse et al. [20], oil is supplied at up to a maximum rate of 400 litres per hour and at temperatures of up to 423 Kelvin. A illustrative example of a thin-film flow subject to surface shear is to consider flow rainwater films on the windscreen of a moving car. The airflow along the windscreen acts as a shearing force opposing gravity and more complex wave structures may become possible as the fluid is forced to travel up the plane. When considering thin-films involving a free surface on an inclined plane, the effects of surface tension, especially in relation to smoothing, may become significant in any steep wave formation and must feature within the model.

There are many branches of industry in which both shear-driven and gravity-driven thin-film flows appear; examples include the flow behaviour of paints and other surface coatings, chemical and nuclear reactor designs, agrochemical applications, as well as other biofluid applications including thin films on the cornea and in the lungs [35]. Thin-film lengthscales vary from a few millimetres in cooling processes of electronic components, to about 10m in thin-film evaporators in the food and chemical industries [46]. Thin films are also associated with coating flows as a collective term for the flows utilized in the coating process itself as well as the incidental flows that occur after coating and before immobilization [55]. In the case of a bearing chamber, oil sheds from bearing rotational elements as droplets which impact on the wall of the bearing chamber creating and enhancing an oil film. Droplet impact is itself an interesting aspect for investigation and is the focus in studies such as [25, 56]. Kay et al. [25] describe the process within the bearing chamber as the oil droplets forming and sustaining a continuous film on the chamber walls. Such film flows are subject to gravity, the momentum from the impacting droplets and the shearing airflow to a sump region of the chamber where it is collected and recycled.

Instabilities of the free surface of the film may play a crucial role in industrial processes by introducing wavy regimes that are known to enhance mass or heat transfer and may lead to film rupture. In coating applications, it is crucial to be able to predict flow behaviour in order to avoid "slides", a term used to describe flow along the external surface of the die which leads to degraded coating uniformity. Additionally Marangoni effects, or more generally, thermo-capillary convection, can provide mass transfer via surface tension gradient, induced by a decreasing temperature in the majority of fluids [14], and is present in many studies [33, 46, 49]. Munch [33] investigates the Marangoni effect on the free surface through an experimental set-up which simulates a shearing force induced by a temperature gradient. With reference to a bearing chamber environment, flow is modelled and numerically simulated in this thesis subject to a constant shearing airflow at

the free surface. Gatapova et al. [18] study a combination of the two factors through investigating shear-driven flow subject to local Marangoni effects; this author assumes inertia to have a negligible effect on the flow.

Other studies [44, 45] typically vary conditions on the fluid-plane boundary to investigate the effects of film flow on a porous substrate. This changes the behaviour of the flow at the boundary and, for cases where the velocity of the flow in the porous medium is small in comparison to the fluid medium, this can effectively be modelled as the fluid slipping, to some extent, over the plane. This is discussed in greater detail in the next section.

The mechanism of evolution of instabilities in this film is also an area of interest, with the formation of various types of wave structures. One interesting class of surface waves is solitary waves - these are structures which propagate with no temporal evolution in shape or size when viewed in a reference system moving with the velocity of the wave. Solitary waves, in the context of thin-film flow on an inclined plane, are repeating structures which grow from inlet perturbations to reach a steady height, dependent on various factors such as the oscillating frequency of the inlet and the film Reynolds number. This is of concern to many of the applications of thin films discussed above, where it is beneficial to be aware of not only the depth of film present, but also the flow dynamics. Experiments with falling thin films have shown that the presence of waves on the surface of a liquid film enhances the mass transfer rates substantially [34], affecting the cooling properties of the oil film which is of significant engineering interest for oil flow in an aeroengine bearing chamber.

1.2 REVIEW OF THIN-FILM MODELLING LITERATURE

Lubrication theory is a common approximation used to model general thin-film flows. Many lubrication theory models are used for film modelling on a plane as Stokes flow models. These correspond to the film Reynolds number, the dimensionless ratio of the inertial forces to the viscous forces

within the film, tending to zero. For film surfaces subject to a high surface shear, the inertial effects at leading order may have a substantial impact in modifying high-speed film profiles. This can provide a general smoothing effect on the film profiles, mathematically extending the range of existing film solutions and physically forming possible new film profiles. Craster et al. [14] refer to comparisons between the predictions of the lubrication equations and Stokes flow equations and experimental data showing that lubrication theory is in error by 15% in the most extreme cases; in this instance the fluid is flowing over step topography rather than a flat inclined plane. Recent studies [23, 25] within a cylindrical geometry demonstrate that modified thin-film wave structures are predicted on including inertial effects into a lubrication formulation, as illustrated in Figure 3. Comparison of the film profiles for $\mathrm{Re}^* = 0.01$ and $\mathrm{Re}^* = 10$ shows a smoothing of the primary peak with increasing film Reynolds number, whilst the capillary region exhibits larger amplitude and shorter wavelength ripples.

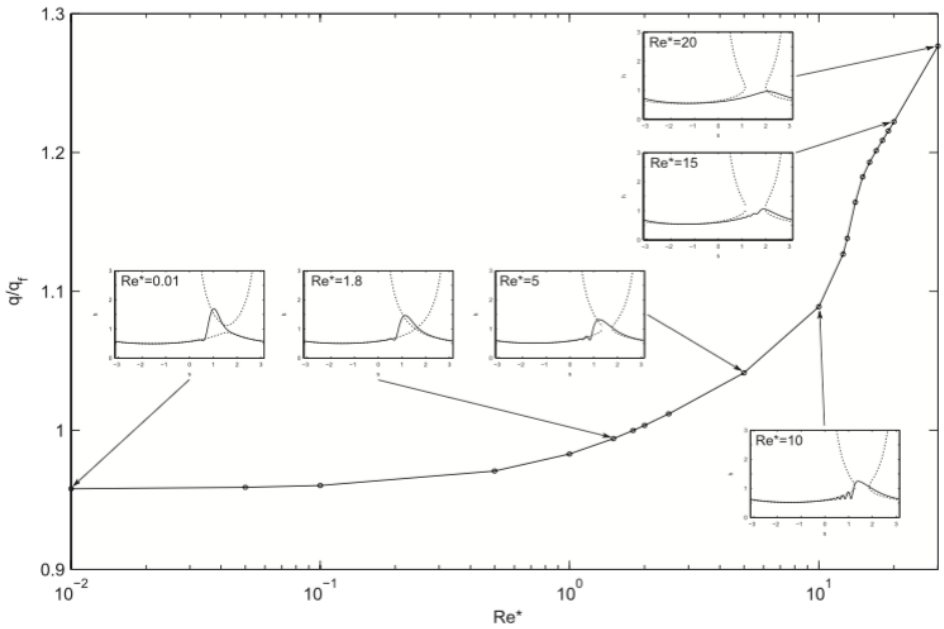


Figure 3.: Examples of film profiles for increasing film Reynolds number [23].

Previous studies, for example [49], for shear-driven flow on an inclined plane describe wave structures depending on their initial profiles as well as uniform upstream and downstream boundary conditions. Figure 4 depicts the evolution of two film profiles, with mirroring boundary conditions. The film on the left evolves into a steady wave structure within a moving frame of reference, whereas the one on the right is a transient profile, evolving with time. These highlight the important part that boundary and initial conditions play in the evolution of the wave structures, and are investigated in great detail within this thesis.

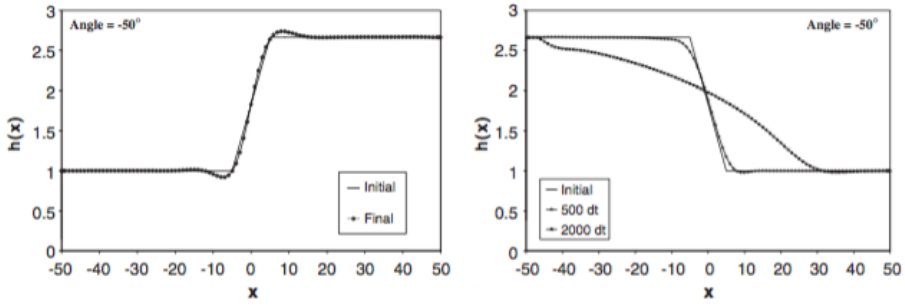


Figure 4.: Example of film profile solutions for Stokes flow [49].

Much of previous thin-film flow modelling has neglected inertia, commonly known as Stokes flow or creeping flow, where the inertial forces within the fluid are considered small compared to the viscous forces. The significant shearing forces within an aerospace application however can provide non-negligible effects. The Reynolds number, a comparison of inertia against viscosity, is taken as small enough to be neglected by assuming a slow fluid velocity and satisfies the Stokes equations for incompressible Newtonian flow

$$\begin{aligned} \mu\nabla^2\mathbf{u} - \nabla p + \mathbf{f} &= 0, \\ \nabla \cdot \mathbf{u} &= 0, \end{aligned} \tag{1.2.1}$$

where p is the pressure within the fluid, ρ is the fluid density and $\mathbf{u}$ the fluid velocity. $\mathbf{f}$ is commonly taken to be the force of gravitation in the associated thin-film literature. The inclusion of Coriolis forces may be relevant

to rotational flow within a bearing chamber enviroment, however Craster et al. [14] claim that these play an analogous role to gravity. Jahn [21] develops equations for describing the pressure variations in a thin film with the inclusion of centrifugal acceleration, and describes the possibility of a buoyancy-like effect caused by differences in centrifugal forces which have the potential to create secondary re-circulations vortices in the film. However Jahn also states that there is a continuous and significant exchange of momentum between the upper and lower layers, which leads to an averaging of the velocity profile. This is the approach taken within this thesis, and so circumvents the need for inclusion of centrifugal acceleration within the model equations. Gravity is to be retained as the sole body force and enables direct comparison to other thin-film studies on an inclined plane. A Stokes flow formulation is commonly used to model situations where the fluid velocities are very slow, or the viscosities are very large. Stokes flow is used to understand lubrication theory arising from the (relative) computational ease with which the resulting thin-film equations may be solved. Although Stokes flow models are useful in predicting potential wave structures on an inclined plane, this simple model of a bearing chamber environment is unlikely to provide the detail seen in experimental work [29], especially at the high fluid velocities experienced in a bearing chamber environment.

Two common approaches for modelling thin films are the long wave model, arriving at the Benney equation, and the integral boundary layer model, leading to the Shkadov equations. Extensive literature exists on both these models as well as proposals for improving their respective shortcomings. For describing falling films, the long wave equation, and other similar models, are derived. These use a perturbation expansion method for the stream function and then used with the surface kinematic boundary condition. An early publication using this method by Benney [5] derives a single evolution equation for film thickness in the nonlinear regime at low Reynolds numbers; corresponding to where flow is dominated by viscosity

and surface tension. For a vertically free-falling film on an inclined plane, the Benney equation is given in [34] as

$$\frac{\partial h}{\partial t} + 3h^2\frac{\partial h}{\partial x} + \frac{\partial}{\partial x}\left(\frac{3}{10}\,\mathrm{Re}\,h^6\frac{\partial h}{\partial x} + \frac{1}{12}\,\mathrm{Re}\,\mathrm{We}\,h^3\frac{\partial^3 h}{\partial x^3}\right) = 0, \tag{1.2.2}$$

where Re is the Reynolds number, the ratio of inertial to viscous forces, and We is the Weber number, the ratio of inertia to surface tension. h denotes the thickness of the film and x the spatial coordinate in the direction parallel to the plane.

The Benney equation is able to predict the linear stability threshold for the long-wave hydrodynamic instability in agreement with the Orr-Sommerfeld equation. It has, however, been criticised as predicting unrealistic wave profiles as the wave amplitude increases [34], as well as leading to finite-time singularities [45, 46, 47]. Pumir et al. [39] state that this behaviour takes place beyond a critical Reynolds number, a shortfall of the Benney equation. A physical blowup may relate to dry patch formation or film rupture and be promoted by the thinness of the film, whereas this behaviour is observed numerically with thicker films [46].

The integral boundary layer model takes the full Navier-Stokes equations and applies a thin-film assumption, leading to neglecting several terms. The Kármán-Polhausen depth-averaging technique can be applied involving integrating throughout the thickness of the film. This technique is used by Kay et al. [23] amongst many others to reduce the dimensionality of the system. A local velocity profile, typically quadratic, is assumed e.g. [10, 34, 46], is then substituted into this thin-film model, leading to a form commonly referred to as the Shkadov model. The quadratic choice of a local film velocity profile is a natural one, as this is the exact profile for fully developed uniform flow on an inclined plane. The Shkadov model is expressed by Nguyen et al. [34] as a coupled set of two partial differential equations

$$\begin{aligned}\frac{\partial q}{\partial t} + \frac{6}{5}\frac{\partial}{\partial x}\left(\frac{q^2}{h}\right) &= \frac{12}{\mathrm{Re}}h - \frac{12}{\mathrm{Re}}\frac{q}{h^2} + \mathrm{We}\,h\frac{\partial^3 h}{\partial x^3},\\ \frac{\partial q}{\partial x} + \frac{\partial h}{\partial t} &= 0,\end{aligned} \tag{1.2.3}$$

in the variables q for film flux and h for film depth, both functions of space x and time t. The surface tension term $h\frac{\partial^3 h}{\partial x^3}$ is notable in this set of equations and is believed to smooth the film profile against the formation of shocks. Numerical stability of attaining solutions is enhanced as a consequence of the physical stability that is provided by the inclusion surface tension.

The Shkadov model also has its shortcomings, predominantly that it does not predict the Hopf bifurcation, necessary to foresee the formation of periodic waves on uniform thickness film flow on inclined planes [34]. Ruyer-Quil et al. [40] claim that fluid films in a moving frame of reference flowing down an inclined plane are unstable against waves when their thickness becomes larger than a specified threshold value $h_{Nc} = (3\,\mathrm{R}_c)^{\frac{1}{3}}$, R_c being a critical Reynolds number. The critical Reynolds number is given by Cheng and Chang [13] as $\mathrm{R}_c = \cot\theta$ who claim that periodic forcing applied at the inlet leads to disturbances propagating downstream whilst growing in amplitude - this happens at Reynolds numbers larger than critical [38]. Correspondingly, there has been research into the stability analysis of numerical models and benchmarking against experimental data. A key area of concern for lower order and depth-averaged models, such as the Skhadov model, is the onset of instability, with numerical simulations showing solutions as stable where perturbations in the experimental counterpart develop into a sequence of solitary waves.

Extensive literature exists on instabilities in gravity-driven thin-film flow within various flow regimes. Numerous studies involve flow on an inclined plane range from near-horizontal flows [53] to vertical falling films [9, 10, 34]. Figure 5 illustrates the growth of instabilities from the inlet boundary into fully formed solitary waves in a vertical falling film - a solution obtained within a numerical simulation study. Others such as Ruyer-Quil et al. [40] analyse the stability conditions for such wave formations, with a view to obtaining a stability curve for various numerical models and comparison against experimental data.

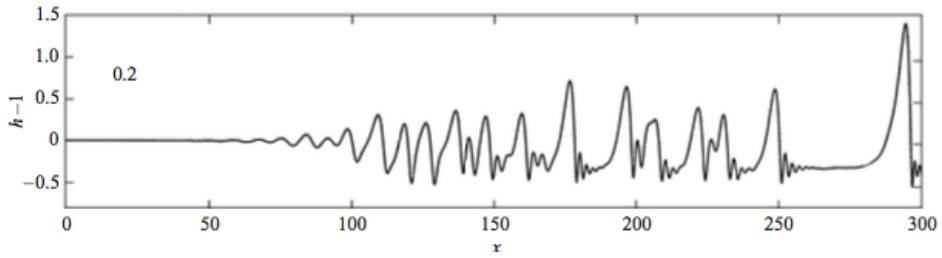


Figure 5.: Plot of surface profile highlight the growth of solitary wave instabilities in a vertical falling film [10].

Ruyer-Quil et al. [40] compare several numerical approaches and show that Shkadov's model predicts the onset of instability at higher Reynolds numbers than observed in the experiments conducted by Liu and Gollub [29]. Ruyer-Quil et al. [41] claim that there are limitations to the Shkadov model deriving from the lack of freedom in the description of the hydrodynamic fields, due to the nature of the depth-averaging technique. Notably, the simplification has the benefit of reduced computational cost on reducing the dimensionality of the Navier-Stokes equation. Indeed, an essential assumption of this model concerns the degree of the polynomial used to approximate the crosswise distribution of the streamwise velocity. A study by Malamataris et al. [32] observes that a self-similar quadratic profile provides a good approximation of the velocity field in regions where deviations are small, but also concludes that there is a change of behaviour around the region in front of a wave hump. Computed velocity profiles with backflow are depicted in Figure 6 [32], with potential inflexion points which could indicate that a higher order polynomial may be a more suitable velocity profile approximation in this region. This is in agreement with work by Samanta et al. [45], who conclude that in a nonlinear regime, the backflow phenomenon is shown to be intensified by a no-slip condition enforced between the fluid and the plane. Backflow in the region near the base of the main wave structure, which we refer to as the capillary region, is investigated experimentally by Dietze et al. [15]; these authors observed negative values of the streamwise velocity component near the wall. It should also

be noted that Malamataris et al. [32] comment on a quadratic profile, which is the exact solution of uniform film flow, enabling the problem analytically tractable. Studies by Prokopiou et al. [38] and Yu et al. [57] extend the Shkadov model in order to allow for higher order description of film profiles relevant at higher Reynolds numbers. Referred to as the second-order boundary layer model, this retains terms of $\mathcal{O}(\varepsilon^2)$, where ε is the film depth-aspect ratio; the modified model includes additional viscous terms, tangential and normal stress conditions and pressure variations across the film.

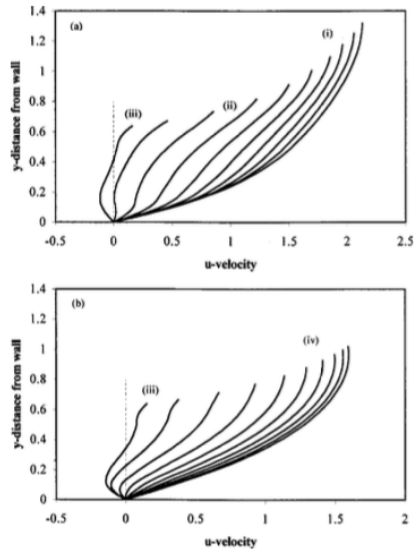


Figure 6.: Streamwise velocity profiles at successive locations from the primary peak of a wave structure to the capillary region [32].

Thin-film flows having free surface shock structures are well-known to form capillary ripples in the region at the base of the shock. In some cases, breakdown of the numerical results can occur in the simulation of Shkadov models due to over-prediction of capillary wave amplitudes, resulting in very thin film thickness. The accuracy of the Shkadov model in predicting capillary ripples is shown to decrease with increasing Reynolds number, with larger than actual capillary waves being predicted e.g. Figure 7. We will show later in Chapter 3, the inclusion of surface shear decreases the capillary wave amplitudes while increasing their wavelength. This will allow

the prediction of wave profiles with shock structures and concurrent front capillary ripples at moderate Reynolds number with the use of Shkadov depth-averaged models.

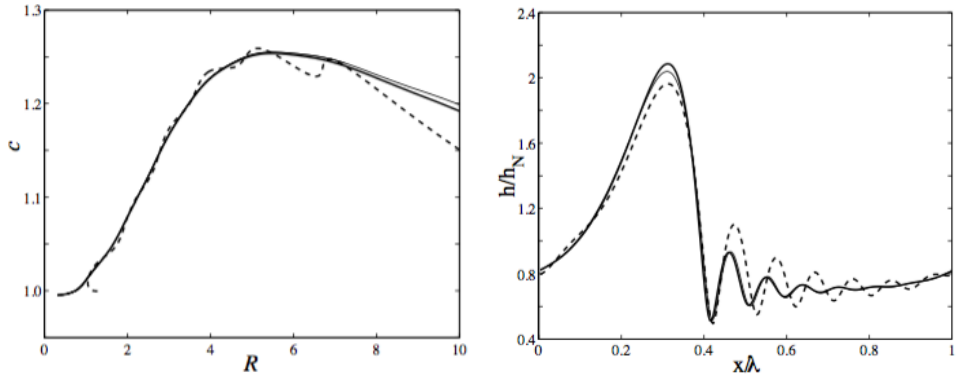


Figure 7.: Comparison of full second-order model (thick, solid), simplified second-order model (thin) and first-order model (dashed) [41]. Left: wave speed c vs Reynolds number R. Right: Film profile in dimensionless coordinates for $R = 10$.

An investigation of travelling wave solutions on an inclined plane by Benilov [4] describes a depth-averaged approach based on neglecting inertial effects. It is suggested in this study that the model can be extended with a term accounting for surface tension by inclusion of the capillary component of the expression for pressure. It should be noted that profiles given in [49], also based on a Stokes flow study, do not exhibit the capillary waves known to physically exist, illustrated in experiments by Liu and Gollub [29], amongst others.

In this thesis, we develop a Shkadov-type integral boundary layer model and investigate the types of wave structures formed on an inclined plane in both moving and stationary frames of reference. Profile development is investigated with the inclusion of inertial terms through the incremental increase of the film Reynolds number up to an order of magnitude acceptable for the approximations made in the derivation of the governing equations. Profiles with the inclusion of surface shear are initially studied with the imposition of a no-slip boundary condition between the fluid and the plane.

The model equations are then extended to include a slip length between the fluid and plane. This, in a physical sense, can be thought of as simulating a substrate which is rough at the microscale, permeable or superhydrophilic, combinations of which can lead to moderate slip lengths [45]. Bailey et al. [3] suggest that the no-slip boundary condition is consistent for liquid fluid motion over a hydrophilic surface. However, when modelling flow over a hydrophobic surface, an apparent slip velocity is observed. The Navier-slip condition on this boundary, as it is commonly known, models a linear relationship between the tangential shear rate and the fluid-plane velocity differences. This yields the fluid velocity at the wall as proportional to its derivative, with the slip length as the proportionality constant. It is also possible to model flow over hydrophilic irregular surfaces by replacing the no-slip condition with an effective slip boundary at an equivalent smooth surface.

Applications of falling films on a porous substrate include rill flows, which are flows in shallow channels in soil created by the erosive action of flowing water, and surface waves over soil systems [44]. The modelling techniques used to study these examples, especially the latter, have much overlap with the surface waves investigated by several of the previously referenced authors, with Samanta et al. [45] developing a depth-averaged Shkadov-type model, whist Sadiq et al. [42] use a long-wave expansion to investigate the stability of the flow. The commonality of many of the various modelling techniques for flow on a porous substrate is the approach to modelling the properties of the fluid-plane boundary. Pascal [37], amongst many others, assume that the porous medium is saturated with fluid and governed by Darcy's law, to describe the slow, viscous flow through a porous medium. Pascal states that the application of Darcy's law is validated by assuming that the intricate geometry of the pore space leads to a low Reynolds number flow. Within this study, Pascal derives a Navier-slip boundary condition of the form

$$\frac{\partial u}{\partial z} = \frac{\alpha}{\sqrt{\kappa}} u \quad \text{on} \quad z = 0, \tag{1.2.4}$$

where u is the componently of fluid velocity parallel to the plane, κ is the permeability of the porous medium and α a dimensionless parameter dependent on the structure of the pore space. The dimensionless slip coefficient (or slip length) is used as a means of accounting for the local geometry of the interface of the porous and liquid layers [54]. The Navier-slip boundary condition is commonly used in adapting thin-film surface wave models to simulate flow over a porous substrate.

Many previous studies [1, 9, 10, 15, 32, 40] on thin-film wave structures investigate falling films, with gravity being the prominent force acting upon it, with a few analysing the stability characteristics e.g. [40]. Numerous other authors [6, 23, 28, 45, 49] investigate thin-film flow subject to surface shear or a surface tension gradient competing against gravity. Kay et al. [23] study two-dimensional thin-film rimming flow within a fixed cylindrical geometry subject to surface shear. Extending previous leading-order thin-film models, inertial effects are included relevant to very high surface shear and correspondingly high-speed film flow applications. Using a hydraulic model approach enabled leading nonlinear inertial effects to be retained. Kay et al. use a local quadratic velocity profile for its consistency with lubrication theory, but also extended to a cubic velocity profile, where the additional profile parameter permits modelling of wall roughness effects. Important to this study, the effects of inertia on some typical rimming-flow solutions provide new and greater insight into existing film solutions.

Samanta [43] investigates the mechanism of instability in shear-imposed flow on an inclined plane. The geometry of the problem studied is very similar to the model proposed in this thesis, with disturbances generated at the inlet which evolve into periodic travelling waves. There are also significant differences in the order of scaling used. Notably the dimensionless governing equations include diffusive terms which, as will later be shown, are disregarded in this formulation due to the nature of the thin-film approximations. Another important comparison is the magnitude of the Reynolds number which differs from what is termed the reduced Reynolds number,

also known as the modified Reynolds number in some literature by $\mathcal{O}(\varepsilon)$. The avenue of exploration in [43] predominantly concerns the linear instability threshold and recovering the critical Reynolds and Froude numbers for the shear-imposed falling film. Although there will not be any formal stability analysis conducted, Chapter 5 contains investigation into the evolution of perturbations in order to compare the stability characteristics of variations of the mathematical model.

A numerical study based on the Stokes equations using a boundary element approach was given by Shuaib et al. [49]. This study determines the different patterns of possible wave structures which can be observed on a thin film flowing on an inclined plane when subject to a constant surface shear, and categorises conditions for different types of film profiles. Studies by Bertozzi et al. [6] proposed that there are several different types of shock waves that connect films of different heights on an inclined plane when the flow is driven by surface shear and gravity. Solutions with more than one type of shock wave were also reported, dependent on the initial configuration of the flow. Bertozzi reports three different types of wave profile, namely compressive shocks, undercompressive shocks and rarefaction waves. In order to obtain the classification of the type of wave, a shock speed S, given by the Rankine-Hugoniot condition

$$S = \frac{Q_- - Q_+}{H_- - H_+}, \tag{1.2.5}$$

is compared with the velocity $F_\pm$ of propagation of small disturbances. In (1.2.5) $H_\pm$ and $Q_\pm$ are the fluid depth and flux respectively, with $+$ and $-$ referring to values on either side of the shock. A compressive shock satisfies the Lax shock inequalities $F_+ \leq S \leq F_-$, assuming travel from left to right; a non-classical shock satisfies the inequalities $S \geq F_-$ and $S \geq F_+$, and is also known as an undercompressive shock. The third type of structure is a rarefaction wave - a smooth, continuous profile gradually joining H_- and H_+.

This thesis investigates the importance of inertia on possible two-dimensional film profiles on an inclined plane under constant surface shear. Validation of the modelling and numerical calculations is evaluated from comparisons with previously published literature, including Shuaib [49] and Bertozzi [6], in the limit of negligible inertial terms. To investigate leading order inertial effects on the film profile, especially in regions where the film profile changes rapidly, modelling will be restricted to at most moderate Reynolds numbers as was achieved by Kay et al. [23]. Kay gives the set of Reynolds numbers characteristic of thin films in bearing chambers as $\mathcal{O}(100)$ [24]. Depth-averaging as used by Benilov, Bertozzi, and Kay [4, 6, 23] and many other authors, is used to obtain governing equations in fewer dependent variables and leads to a Shkadov-type integral boundary layer model following adoption of an assumed velocity profile. Film flow dynamics are given in terms of a pair of coupled partial differential equations for film thickness and local film flux.

Problems and criticisms of the integral boundary layer approach arise when applied to investigating surface waves periodically forced at the inlet e.g. see [10]. Periodic perturbations at the inlet lead to the formation of repeating wave structures known as solitary wave structures. It is noted that solitary waves are distinct from solitons, the former being interactive between waves. Liu and Gollub [29] note that an alternative method to inducing solitary waves is to have natural waves at the inlet, such as due to ambient noise. This is investigated by Chang, Demekhin and Saprikin [10] who utilise white noise at the inlet. Nonlinear instabilities in the small amplitude perturbations then encourage evolution into multi-peak solitary waves. Liu and Gollub [29] provide comprehensive detail on the evolution of solitary waves and the changes in interaction between primary peaks dependent on forcing frequency. Solitary waves are a common nonlinear occurence in falling liquid films down an inclined plane. The inclination angle of the plane varies, with literature existing on near-horizontal flows as well as vertical falling films. Experimental studies of solitary waves provide a ba-

sis against which numerical simulations may be compared. Liu and Gollub [29] study experimentally the flow dynamics of a glycerin-water solution on an almost horizontal plane, inducing solitary waves by periodically forcing the inlet at a given frequency. The flow conditions must exceed a critical Reynolds number in order for the inlet perturbations to grow in amplitude.

A more recent publication by Scheid et al. [47] validates various numerical models against the experimental data provided by Liu and Gollub, before preceding to investigate flow characteristics and associated velocity profiles within the solitary wave structures. The velocity profiles illustrated in [47] are indicative of regions of backflow, and the presence of two or more inflexion points within the profile suggest that a quadratic velocity profile is insufficient to capture the full flow dynamics. However, it is also suggested that this phenomenon is in a very localised region. Scheid et al. [47] come to the conclusion that several of the numerical models evaluated within this study, such as the regularised model and the complete second-order model, predict maximum heights larger than experimental findings, as well as larger amplitudes. Their numerical models do however predict the shape and speed of the solitary waves in the range of parameters explored by Liu and Gollub. The overprediction of the amplitude of capillary waves is also present in several other studies. Tihon et al. [51] observe that the discrepancy becomes worse at higher Reynolds numbers, at which steeper capillary ripples are required in order to stabilize the solitary hump. They hypothesise that the solitary hump will gradually approach a hydraulic jump, with the precursor ripples merging into a shock. A series of profiles for increasing Reynolds number as calculated by Tihon et al. [51] is reproduced in Figure 8. Profiles in Figure 8 can be compared to those obtained by Kay et al. [23] in Figure 3. It is observed that with increasing Reynolds number, there is a distinct increase in the amplitude and decrease in wavelength of the capillary ripples formed at the base of the primary peak of the wave.

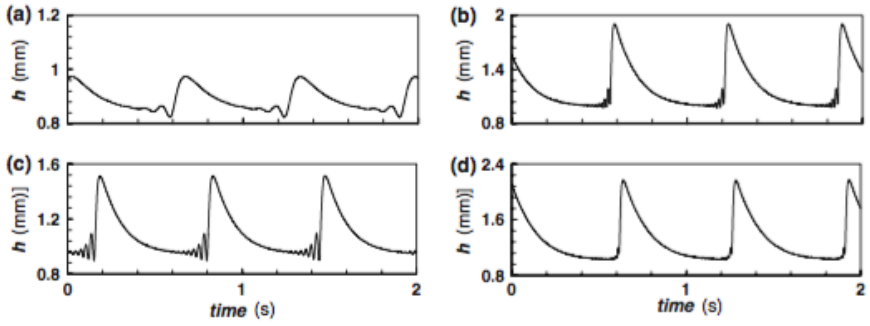


Figure 8.: Profiles calculated for increasing film Reynolds numbers from (a) to (d) [51].

1.3 OVERVIEW OF THE THESIS

A major aim of this thesis is to extend current studies through investigating the impact of inertial terms on the thin-film shock structures formed on an inclined plane. For uniform flow down an inclined plane, a constant-height exact basic flow configuration with quadratic streamwise velocity profile, known as the Nusselt solution, exists from the Navier-Stokes equations. Such solutions are considered far away from any localised shock structures. For a specified steady value of flux, this can provide up to three physically valid conjugate Nusselt heights. Additional solutions with transitions from the conjugate states may be able to coexist to form a piecewise steady film profile.

A key objective is to develop a suitably robust model of the film behaviour of thin films subject to shear at the free surface whilst retaining the physical characteristics of the fluid such as surface tension and, importantly, inertial effects within the film. Besides the practical need for the accurate modelling of surface waves, there is the theoretical challenge of modelling the rich spectrum of wave structures that can form within the flow on an inclined plane.

The literature review in Section 1.2 provides an overview of thin-film flows and their various modelling techniques as well as discussing, in greater

detail, research which has been carried out in this field. The merits of the techniques adopted by the previous authors are highlighted as well as provision of insight into the modelling methods we carry forward into the research presented in this thesis. Existing mathematical models are evaluated and justification is given for the choice of modelling approach in this chapter.

A two-dimensional mathematical model for flow on an inclined plane as derived from the Navier-Stokes equations is introduced in Chapter 2. The model is formulated with the inclusion of a shearing force on the free surface as well as variable slip parameter on the boundary where the fluid is in contact with the plane. Approximations are then taken consistent with an assumption of a moderate Reynolds number. Additionally this is consistent with thin-film flows within the industrial context of a gas-turbine bearing-chamber environment. Formulation is kept general enough such that the model can also serve as a basis for broader variations investigated in subsequent chapters. This chapter also includes a description of the numerical methods used to obtain solutions.

Within an initial study in Chapter 3, film profiles are obtained under shear-imposed conditions and assuming a quadratic form for the velocity of the fluid. Importance is given to the effects of including appropriate inertial terms within the model formulation. Of significance is identification of new wave structures as a result of inertia. Initial profiles are simulated on a plane at moderate angles of inclination, and this is later extended to include solutions at an almost vertical position to explore differences. The formulation of the mathematical model and much of the results assuming a quadratic velocity profile have been included in a recently published study [50]. A cubic profile approach to approximating the flow velocity within the film is then developed in the latter part of the chapter, with the aim of capturing regions of fluid recirculation with greater accuracy. Shear-driven flow on an inclined plane is considered, and resulting profiles are compared against their equivalent analogues when assuming a quadratic representa-

tion. Velocity profile are recreated for quadratic and cubic formulations and compared at both moderate slope inclination angles as well as at a near-vertical angle.

A generalisation of this model is studied in Chapter 4, in which Navier-slip is introduced at the boundary between the fluid and the plane. This enables modelling of the effects of thin-film flow on a porous substrate and also allows investigation into an extended range of solutions and their flow dynamics. The longitudinal velocity of the fluid is taken to be quadratic.

A study into the gravity-driven flow of solitary waves derived from periodic forcing at the inlet is provided. Consideration is given to analysing both quadratic and cubic models. Both physical models are benchmarked against available experimental data and results evaluated for consistency and accuracy. The effects of inertia on these types of wave structures are also investigated, as well as the stability characteristics of the quadratic and cubic models. In a final section within this chapter, the effect of imposing surface shear on solitary wave structures is examined.

Outcomes of this study and results obtained are summarised and an overview of the mathematical model developed within the thesis is given in Chapter 6. Overarching evaluation and concluding remarks are provided.

2

THIN-FILM MODEL FORMULATION INCLUDING INERTIAL EFFECTS

A Cartesian coordinate system is used to describe the flow down a flat, inclined plane with the velocity vector $\bar{\mathbf{u}} = (\bar{u}, \bar{v})$, where $\bar{u}$ is the component of the velocity in the $\bar{x}$-direction and $\bar{v}$ is the component in the $\bar{y}$-direction. The angle of inclination, $\bar{\theta}$, is measured in the anticlockwise direction from the horizontal, and so the angle depicted in Figure 9 would be negative. The flow is subject to a constant surface shear $\bar{\tau}$ opposing gravity and a pressure $\bar{p}_a$ at the free surface with typical wave speed U. For this study, a transformation to a moving coordinate system is chosen, with the plane moving with fixed reference speed U in the negative $\bar{x}$-direction, as shown in Figure 9.

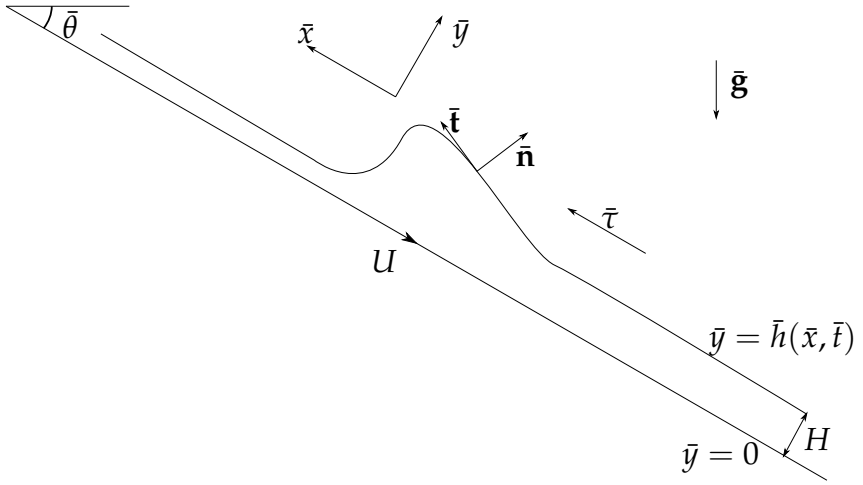


Figure 9.: Plane geometry in dimensional coordinate system

The fluid considered within the numerical experiments is assumed to be incompressible, a reasonable assumption considering that the applications relate to shear-driven oil flow within bearing chambers, as well as the more general experiments carried out predominantly with a water-glycerine mixture. Hence, the film is assumed to be incompressible, with constant density ρ and constant viscosity μ. Gravity is acting with components $\bar{\mathbf{g}} = (g\sin\bar{\theta}, -g\cos\bar{\theta})$. The unit normal vector $\bar{\mathbf{n}}$ and the unit tangential vector $\bar{\mathbf{t}}$ to the free surface are

$$\bar{\mathbf{n}} = \frac{1}{\left(1+\frac{\partial\bar{h}}{\partial\bar{x}}^2\right)^{\frac{1}{2}}}\left(-\frac{\partial\bar{h}}{\partial\bar{x}}, 1\right), \quad \bar{\mathbf{t}} = \frac{1}{\left(1+\frac{\partial\bar{h}}{\partial\bar{x}}\right)^{\frac{1}{2}}}\left(1, \frac{\partial\bar{h}}{\partial\bar{x}}\right). \tag{2.0.1}$$

The incompressible Navier-Stokes equations are taken as the governing equations - conservation of mass is described by

$$\frac{\partial\bar{u}}{\partial\bar{x}} + \frac{\partial\bar{v}}{\partial\bar{y}} = 0 \tag{2.0.2}$$

and the conservation of momentum is given by

$$\rho\left(\frac{\partial\bar{u}}{\partial\bar{t}} + \bar{u}\frac{\partial\bar{u}}{\partial\bar{x}} + \bar{v}\frac{\partial\bar{u}}{\partial\bar{y}}\right) = -\frac{\partial\bar{p}}{\partial\bar{x}} + \mu\left(\frac{\partial^2\bar{u}}{\partial\bar{x}^2} + \frac{\partial^2\bar{u}}{\partial\bar{y}^2}\right) + \rho g\sin\bar{\theta}, \tag{2.0.3}$$

$$\rho\left(\frac{\partial\bar{v}}{\partial\bar{t}} + \bar{u}\frac{\partial\bar{v}}{\partial\bar{x}} + \bar{v}\frac{\partial\bar{v}}{\partial\bar{y}}\right) = -\frac{\partial\bar{p}}{\partial\bar{y}} + \mu\left(\frac{\partial^2\bar{v}}{\partial\bar{x}^2} + \frac{\partial^2\bar{v}}{\partial\bar{y}^2}\right) - \rho g\cos\bar{\theta}. \tag{2.0.4}$$

A slip length of L_s and a no-penetration boundary condition is imposed at the boundary between the fluid and the plane, giving

$$\bar{u} = -U + L_s\frac{\partial\bar{u}}{\partial\bar{y}} \quad \text{and} \quad \bar{v} = 0 \quad \text{on} \quad \bar{y} = 0 \tag{2.0.5}$$

and the kinematic condition on the free surface gives

$$\frac{\partial\bar{h}}{\partial\bar{t}} + \bar{u}\frac{\partial\bar{h}}{\partial\bar{x}} = \bar{v} \quad \text{on} \quad \bar{y} = \bar{h}(\bar{x},\bar{t}). \tag{2.0.6}$$

The boundary condition on $y = 0$ is left general such that the value of the slip length may be specified later. Taking the surface of the film to have surface tension σ, a balance of forces on the interface between liquid

and gas, when written in component form [40], leads to the normal stress boundary condition,

$$\frac{\sigma\frac{\partial^2\bar{h}}{\partial\bar{x}^2}}{\left(1+\frac{\partial\bar{h}}{\partial\bar{x}}^2\right)^{\frac{3}{2}}}+\frac{2\mu}{\left(1+\frac{\partial\bar{h}}{\partial\bar{x}}\right)^2}\left(\frac{\partial\bar{h}}{\partial\bar{x}}\left(\frac{\partial\bar{u}}{\partial\bar{y}}+\frac{\partial\bar{v}}{\partial\bar{x}}\right)-\frac{\partial\bar{h}}{\partial\bar{x}}^2\frac{\partial\bar{u}}{\partial\bar{x}}-\frac{\partial\bar{v}}{\partial\bar{y}}\right)+\bar{p}-\bar{p_a}=0$$

$$\text{on}\quad \bar{y}=\bar{h} \quad (2.0.7)$$

and the tangential stress condition,

$$\bar{\tau}=2\mu\frac{\partial\bar{h}}{\partial\bar{x}}\left(\frac{\partial\bar{v}}{\partial\bar{y}}-\frac{\partial\bar{u}}{\partial\bar{x}}\right)+\mu\left(1-\frac{\partial\bar{h}}{\partial\bar{x}}^2\right)\left(\frac{\partial\bar{u}}{\partial\bar{y}}+\frac{\partial\bar{v}}{\partial\bar{x}}\right)\quad\text{on}\quad\bar{y}=\bar{h}. \quad (2.0.8)$$

The model is non-dimensionalised using the following choice of scalings:

$$\bar{x}=\frac{H}{\varepsilon}x,\quad(\bar{y},\bar{h})=H(y,h),\quad\bar{u}=Uu,\quad\bar{v}=\varepsilon Uv,$$
$$(\bar{p},\bar{p_a})=\frac{\mu U}{\varepsilon H}(p,p_a),\quad\bar{t}=\frac{H}{\varepsilon U}t,\quad\bar{\theta}=\theta\quad\text{and}\quad\bar{\tau}=\frac{\mu U}{H}\tau. \quad (2.0.9)$$

U is the speed of the wall, H is a typical height of the film and $\frac{H}{\varepsilon}$ is an $\bar{x}$-lengthscale, where $\varepsilon \ll 1$ is the ratio of vertical film thickness to the horizontal lengthscales associated with a wave disturbance. This choice of non-dimensionalisation is typical of a thin-film model.

The Navier-Stokes Equations (2.0.2)-(2.0.4) in the dimensionless variables are

$$\frac{\partial u}{\partial x}+\frac{\partial v}{\partial y}=0, \quad (2.0.10)$$

$$\varepsilon\,\mathrm{Re}\left(\frac{\partial u}{\partial t}+u\frac{\partial u}{\partial x}+v\frac{\partial u}{\partial y}\right)=-\frac{\partial p}{\partial x}+\varepsilon^2\frac{\partial^2 u}{\partial x^2}+\frac{\partial^2 u}{\partial y^2}+\lambda\sin\theta, \quad (2.0.11)$$

$$\varepsilon^3\,\mathrm{Re}\left(\frac{\partial v}{\partial t}+u\frac{\partial v}{\partial x}+v\frac{\partial v}{\partial y}\right)=-\frac{\partial p}{\partial y}+\varepsilon^4\frac{\partial^2 v}{\partial x^2}+\varepsilon^2\frac{\partial^2 v}{\partial y^2}-\varepsilon\lambda\cos\theta. \quad (2.0.12)$$

The film Reynolds number $\mathrm{Re}=\frac{\rho UH}{\mu}$ is the dimensionless ratio of inertial to viscous forces and can be used to characterise the nature of the flow, with higher Reynolds number flows exhibiting greater turbulence. Such flow is dominated by inertial forces and tends to produce flow instabilities.

The gravitational parameter is given by $\lambda = \frac{\rho g H^2}{\mu U} = \frac{\mathrm{Re}}{\mathrm{Fr}}$, where the Froude number, $\mathrm{Fr} = \frac{U^2}{gH}$, is the ratio of inertial to gravitational forces. The dimensionless form of the kinematic boundary condition (2.0.6) is

$$\frac{\partial h}{\partial t} + u\frac{\partial h}{\partial x} = v \quad \text{on} \quad y = h \tag{2.0.13}$$

and the slip and no-penetration conditions (2.0.5) become

$$u = -1 + \alpha\frac{\partial u}{\partial y} \quad \text{and} \quad v = 0 \quad \text{on} \quad y = 0, \tag{2.0.14}$$

where $\alpha = \frac{L_s}{H}$ is the dimensionless slip length. The normal stress boundary condition (2.0.7) gives

$$\frac{\varepsilon^3 \frac{\partial^2 h}{\partial x^2}}{\mathrm{Ca}\left(1 + \varepsilon^2 \frac{\partial h}{\partial x}^2\right)^{\frac{3}{2}}} + \frac{2}{(1 + \varepsilon^2 \frac{\partial h}{\partial x})^2}\left(\varepsilon^2 \frac{\partial h}{\partial x}\left(\frac{\partial u}{\partial y} + \varepsilon^2 \frac{\partial v}{\partial x}\right) - \varepsilon^4 \frac{\partial h}{\partial x}^2 \frac{\partial u}{\partial x} - \varepsilon^2 \frac{\partial v}{\partial y}\right)$$
$$+ p - p_a = 0 \quad \text{on} \quad y = h. \tag{2.0.15}$$

The capillary number, $\mathrm{Ca} = \frac{\mu U_0}{\sigma}$, relates the effects of viscosity to surface tension across the interface between a liquid and a gas, although in various other formulations [34, 46], the Weber and Kapitza numbers have been included as a similar comparison between surface tension and other fluid forces. Gjevik [19] takes the Weber number to be of $\mathcal{O}(\varepsilon^{-2})$, corresponding to a choice of Capillary number in the current formulation of $\mathcal{O}(\varepsilon^{-2})$. This results in an overall surface tension term of $\mathcal{O}(\varepsilon)$. The tangential stress condition (2.0.8) is non-dimensionalised as

$$\tau = 2\varepsilon^2 \frac{\partial h}{\partial x}\left(\frac{\partial v}{\partial y} - \frac{\partial u}{\partial x}\right) + \left(1 - \varepsilon^2 \frac{\partial h}{\partial x}^2\right)\left(\frac{\partial u}{\partial y} + \varepsilon^2 \frac{\partial v}{\partial x}\right) \quad \text{on} \quad y = h. \tag{2.0.16}$$

2.1 NUSSELT SOLUTIONS FOR UNIFORM FLOW ON AN INCLINED PLANE

In the context of Stokes flow, the limit $\mathrm{Re} \to 0$ is taken and the governing equations become

$$\frac{\partial u}{\partial x} + \frac{\partial v}{\partial y} = 0, \tag{2.1.1}$$

$$-\frac{\partial p}{\partial x} + \varepsilon^2 \frac{\partial^2 u}{\partial x^2} + \frac{\partial^2 u}{\partial y^2} + \lambda \sin\theta = 0, \tag{2.1.2}$$

$$-\frac{\partial p}{\partial y} + \varepsilon^4 \frac{\partial^2 v}{\partial x^2} + \varepsilon^2 \frac{\partial^2 v}{\partial y^2} - \varepsilon\lambda \cos\theta = 0. \tag{2.1.3}$$

Thin-film flow studies evaluate Equations (2.1.1)-(2.1.3) in the context of lubrication theory, with $\varepsilon \ll 1$. Unidirectional uniform flow is considered by taking the component of the velocity perpendicular to the plane $v = 0$ at leading order. Thus, assuming no variation in the x-coordinate direction, (2.1.2) is reduced to

$$\frac{\partial^2 u}{\partial y^2} + \lambda \sin\theta = 0. \tag{2.1.4}$$

Together with the slip boundary condition (2.0.14) on the lower wall and the surface shear condition (2.0.16) on the free surface, which becomes

$$u_y = \tau \quad \text{on} \quad y = h \tag{2.1.5}$$

when $\varepsilon \ll 1$, this yields a quadratic form for the component of film velocity parallel to the inclined plane

$$u = -\frac{\lambda}{2} y^2 \sin\theta + (\lambda h \sin\theta + \tau)\, y + \alpha(\lambda h \sin\theta + \tau) - 1, \tag{2.1.6}$$

also termed as the streamwise or longitudinal velocity. The film flux is calculated by integrating the streamwise velocity profile, $q = \int_0^h u \, \mathrm{d}y$, giving

$$q = \frac{\lambda h^3}{3} \sin\theta + \left(\frac{\tau}{2} + \alpha\lambda \sin\theta\right) h^2 + (\alpha\tau - 1)h. \tag{2.1.7}$$

For a fixed flux and for specified values of α, λ, θ and τ, the cubic polynomial (2.1.7) yields up to three possible conjugate heights for a uniform profile, commonly known as the Nusselt solutions. In order for three distinct values of h satisfying the same q, the range of values which surface

shear τ may take is limited, as can be seen in Figure 10. Assuming no slip on the fluid-plane boundary, the curves for $\tau = 1.8320$ and $\tau = 2.6171$ (to 4 d.p.) represent limiting case scenarios which result in two distinct heights for a given flux, beyond which there is only a single Nusselt solution possible.

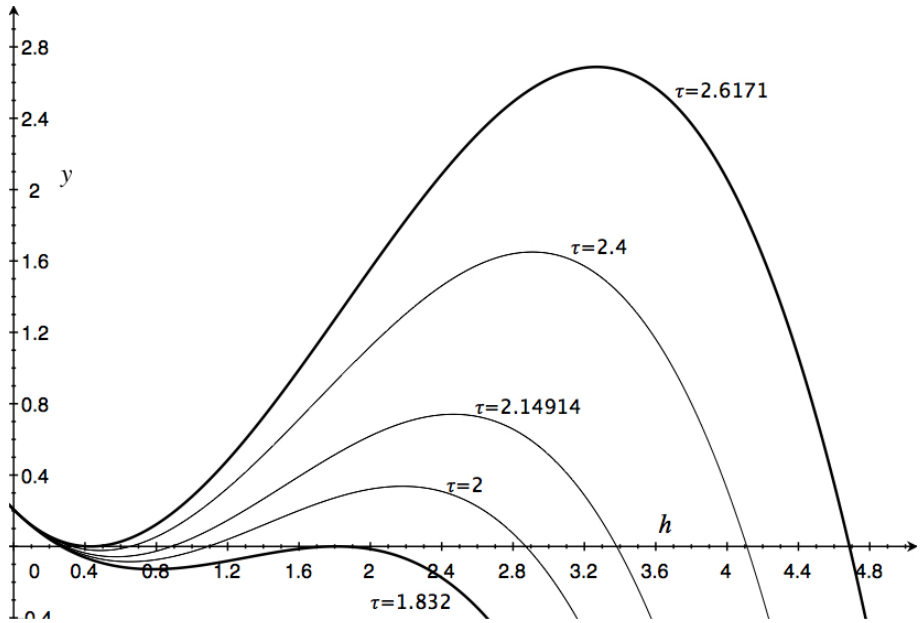


Figure 10.: Cubic polynomial $y = \frac{\lambda \sin\theta}{3}h^3 + \frac{\tau}{2}h^2 - h - q$ plotted for increasing values of τ. $\alpha = 0$, $\lambda = 1$, $\theta = -45$, $q = -0.2068$.

2.2 THIN-FILM FLOW AT MODERATE REYNOLDS NUMBERS

Thin films subject to strong surface shear may experience moderate inertial effects at leading order on taking the following formal approximations:

$$\varepsilon \ll 1, \quad \mathrm{Re} \sim \mathcal{O}\left(\frac{1}{\varepsilon}\right) \quad \text{and} \quad \lambda \sim \mathcal{O}(1). \tag{2.2.1}$$

These lead to moderate values of Reynolds number that can be compared to classical lubrication theory studies [49], where $\varepsilon \ll 1$ and $\mathrm{Re} \to 0$. The Navier-Stokes Equations (2.0.10)-(2.0.12), to $\mathcal{O}(\varepsilon)$, are

$$\frac{\partial u}{\partial x} + \frac{\partial v}{\partial y} = 0, \tag{2.2.2}$$

$$\mathrm{Re}^* \left(\frac{\partial u}{\partial t} + u\frac{\partial u}{\partial x} + v\frac{\partial u}{\partial y} \right) = -\frac{\partial p}{\partial x} + \frac{\partial^2 u}{\partial y^2} + \lambda \sin\theta, \tag{2.2.3}$$

$$\frac{\partial p}{\partial y} + \varepsilon\lambda \cos\theta = 0, \tag{2.2.4}$$

where $\mathrm{Re}^* = \varepsilon\,\mathrm{Re}$ is the reduced Reynolds number. The fluid-plane boundary conditions remain exact.

In considering the normal stress boundary condition (2.0.15), the surface tension term involving $\frac{\partial^2 h}{\partial x^2}$ is retained. Although negligible in the majority of the flow, it can become comparable to the other terms in regions of any shock transitions between conjugate height solutions and therefore may have a dominant local effect on the flow. This approach is consistent also with other thin-film studies [19, 23, 34] and the normal stress condition (2.0.15) is approximated as

$$\frac{\varepsilon^3}{\mathrm{Ca}}\frac{\partial^2 h}{\partial x^2} + p - p_a = 0 \quad \text{on} \quad y = h. \tag{2.2.5}$$

The tangential stress boundary condition (2.0.16) under the above approximation is

$$\tau = \frac{\partial u}{\partial y} \quad \text{on} \quad y = h. \tag{2.2.6}$$

2.3 AN INTEGRAL BOUNDARY LAYER MODEL

The Kármán-Polhausen depth-averaging technique is used to reduce the system of equations by integrating (2.2.2)-(2.2.4) from the wall at $y = 0$ through to the surface of the film at $y = h$. Kay [23] uses a similar technique to remove radial dependence in a film flow within a polar coordinate system.

Leibniz' integral rule is used to express differentiation under the integral sign in an equivalent form. A general form of Leibniz' rule is

$$\int_{a(t)}^{b(t)} \frac{\partial f}{\partial t}\,\mathrm{d}x = \frac{\mathrm{d}}{\mathrm{d}t}\left(\int_{a(t)}^{b(t)} f(x,t)\,\mathrm{d}x\right) - f(b(t),t)\frac{\mathrm{d}b}{\mathrm{d}t} + f(a(t),t)\frac{\mathrm{d}a}{\mathrm{d}t}. \quad (2.3.1)$$

Depth-averaging the continuity equation (2.2.2) yields

$$\frac{1}{h}\int_0^h \frac{\partial u}{\partial x}\,\mathrm{d}y + \frac{1}{h}\int_0^h \frac{\partial v}{\partial y}\,\mathrm{d}y = 0, \quad (2.3.2)$$

which, using Leibniz' rule, can be written as

$$\frac{\mathrm{d}}{\mathrm{d}x}\int_0^h u\,\mathrm{d}y - u\Big|_h \frac{\partial h}{\partial x} + \left[v\right]_0^h = 0. \quad (2.3.3)$$

The no-penetration condition $v = 0$ on $y = 0$ and kinematic boundary condition $\frac{\partial h}{\partial t} + u\frac{\partial h}{\partial x} = v$ on $y = h(x,t)$ are incorporated into (2.3.3), giving

$$\frac{\partial h}{\partial t} + \frac{\partial q}{\partial x} = 0, \quad (2.3.4)$$

where q is the dimensionless volume flux. Integrating Equation (2.2.4) and applying the normal stress boundary condition (2.2.5) gives the pressure within the film as

$$p = p_a + \varepsilon\lambda(h-y)\cos\theta - \frac{\varepsilon^3}{\mathrm{Ca}}h_{xx}. \quad (2.3.5)$$

Depth-averaging of Equation (2.2.3) again involves integrating across the thickness of the film to give

$$\mathrm{Re}^*\,\frac{1}{h}\left(\int_0^h \frac{\partial u}{\partial t} + u\frac{\partial u}{\partial x} + v\frac{\partial u}{\partial y}\,\mathrm{d}y\right) = \frac{1}{h}\left(\int_0^h -\frac{\partial p}{\partial x} + \frac{\partial^2 u}{\partial y^2} + \lambda\sin\theta\,\mathrm{d}y\right). \quad (2.3.6)$$

The terms within the integral on the left hand side of (2.3.6) are algebraically manipulated using a combination of the chain rule, the product rule and the continuity equation (2.2.2) to give the revised form:

$$\begin{aligned}\frac{\partial u}{\partial t} + u\frac{\partial u}{\partial x} + v\frac{\partial u}{\partial y} &= \frac{\partial u}{\partial t} + \frac{\partial}{\partial x}\left(u^2\right) - u\frac{\partial u}{\partial x} + \frac{\partial}{\partial y}(uv) - u\frac{\partial v}{\partial y}\\ &= \frac{\partial u}{\partial t} + \frac{\partial}{\partial x}\left(u^2\right) + \frac{\partial}{\partial y}(uv) - u\left(\frac{\partial u}{\partial x} + \frac{\partial v}{\partial y}\right)\\ &= \frac{\partial u}{\partial t} + \frac{\partial}{\partial x}\left(u^2\right) + \frac{\partial}{\partial y}(uv). \end{aligned} \quad (2.3.7)$$

Using Leibniz' rule gives

$$\begin{aligned}
&\int_0^h \frac{\partial u}{\partial t} + u\frac{\partial u}{\partial x} + v\frac{\partial u}{\partial y}\,\mathrm{d}y \\
&= \int_0^h \frac{\partial u}{\partial t} + \frac{\partial}{\partial x}\left(u^2\right) + \frac{\partial}{\partial y}(uv)\,\mathrm{d}y \\
&= \frac{\partial}{\partial t}\int_0^h u\,\mathrm{d}y - u\Big|_h \frac{\partial h}{\partial t} + \frac{\partial}{\partial x}\int_0^h u^2\,\mathrm{d}y - u^2\Big|_h \frac{\partial h}{\partial x} + \Big[uv\Big]_0^h \\
&= \frac{\partial}{\partial t}\int_0^h u\,\mathrm{d}y + \frac{\partial}{\partial x}\int_0^h u^2\,\mathrm{d}y + \Big[uv\Big]_0^h - u\Big|_h \left(\frac{\partial h}{\partial t} - u\Big|_h \frac{\partial h}{\partial x}\right). \qquad (2.3.8)
\end{aligned}$$

Using the kinematic boundary condition (2.0.13) and the no-penetration condition (2.0.14) provides the identity

$$\int_0^h \frac{\partial u}{\partial t} + u\frac{\partial u}{\partial x} + v\frac{\partial u}{\partial y}\,\mathrm{d}y \equiv \frac{\partial}{\partial t}\int_0^h u\,\mathrm{d}y + \frac{\partial}{\partial x}\int_0^h u^2\,\mathrm{d}y. \qquad (2.3.9)$$

Use of tangential stress boundary condition $\frac{\partial u}{\partial y} = \tau$ on $y = h$ and the expression for pressure within the film (2.2.2), the depth-averaged momentum equation (2.3.6) is written as

$$\mathrm{Re}^*\left(\frac{\partial q}{\partial t} + \frac{\partial}{\partial x}\int_0^h u^2\,\mathrm{d}y\right) = \lambda h\sin\theta + \tau - \frac{\partial u}{\partial y}\Big|_{y=0} - \varepsilon\lambda h\frac{\partial h}{\partial x}\cos\theta + \frac{\varepsilon^3}{\mathrm{Ca}}h\frac{\partial^3 h}{\partial x^3}. \qquad (2.3.10)$$

It is convenient to introduce nonlinear coefficients I_h and I_q that can be used to simplify the integral term on application of the chain rule:

$$\begin{aligned}
\frac{\partial}{\partial x}\left(\int_0^h u^2\,\mathrm{d}y\right) &= \frac{\partial}{\partial h}\left(\int_0^h u^2\,\mathrm{d}y\right)\frac{\partial h}{\partial x} + \frac{\partial}{\partial q}\left(\int_0^h u^2\,\mathrm{d}y\right)\frac{\partial q}{\partial x} \\
&= I_h\frac{\partial h}{\partial x} + I_q\frac{\partial q}{\partial x} \qquad (2.3.11)
\end{aligned}$$

where

$$I_h = \frac{\partial}{\partial h}\int_0^h u^2\,\mathrm{d}y \quad \text{and} \quad I_q = \frac{\partial}{\partial q}\int_0^h u^2\,\mathrm{d}y. \qquad (2.3.12)$$

The third order partial differential momentum equation in $h(x,t)$ and $q(x,t)$ becomes

$$\mathrm{Re}^*\left(\frac{\partial q}{\partial t} + I_h\frac{\partial h}{\partial x} + I_q\frac{\partial q}{\partial x}\right) = \lambda h\sin\theta + \tau - \frac{\partial u}{\partial y}\Big|_{y=0} - \varepsilon\lambda h\frac{\partial h}{\partial x}\cos\theta + \frac{\varepsilon^3}{\mathrm{Ca}}h\frac{\partial^3 h}{\partial x^3}, \qquad (2.3.13)$$

to be solved together with the continuity equation

$$\frac{\partial h}{\partial t} + \frac{\partial q}{\partial x} = 0. \qquad (2.3.14)$$

Exact expressions for I_h and I_q are derived once an approximation for the streamwise velocity profile u is assumed; this is detailed in the following chapters. Physical interpretation of the various terms in the momentum equation (2.3.11) are summarised in Table 1 to clarify the mathematical terminology.

Mathematical term	**Physical interpretation**
$\mathrm{Re}^* \left(\frac{\partial q}{\partial t} + I_h \frac{\partial h}{\partial x} + I_q \frac{\partial q}{\partial x} \right)$	Inertia
$\lambda h \sin\theta$	Gravity
τ	Surface shear
$\left. \frac{\partial u}{\partial y} \right\vert_{y=0}$	Assumed velocity profile
ε	Depth aspect ratio
$\varepsilon \lambda h \frac{\partial h}{\partial x} \cos\theta$	Hydrostatic pressure
$\frac{\varepsilon^3}{\mathrm{Ca}} h \frac{\partial^3 h}{\partial x^3}$	Surface tension

Table 1.: Physical interpretation of terms in the momentum equation (2.3.11).

2.4 NUMERICAL METHODS

The governing continuity and momentum equations, and associated boundary conditions are solved numerically on a computational domain $0 < x < L$. The domain is discretised by $n-1$ uniformly spaced interior nodes x_i, for $i = 1 \ldots n-1$; local film profiles at x_0 and x_n are assumed to be of uniform film depth and flow is assumed to be entirely parallel to the plane at these points.

2.4.1 *Initial and boundary conditions*

Values of h are known as boundary conditions at x_0 and x_n, but are applied selectively at only one of the boundaries to avoid overspecification which would cause the PDE problem to be ill-posed. These uniformity conditions remain in every case considered within this thesis; additionally Dirichlet boundary values are assigned to be the Nusselt heights for the constant boundary studies, dependent on the parameters within the system, and are discussed in later chapters. The Dirichlet boundary for the oscillating boundary problems that are used to study solitary wave structures in Chapter 5 are taken to be time-dependent.

Boundary conditions are enforced at every iteration in obtaining a solution for governing equations. It is noted the problem will be dependent on the initial conditions prescribed in seeking transient profiles. Typically Nusselt heights are taken as the basis of the initial profiles, with a smooth curve based on a hyperbolic tangent joining two different heights. The exact form of the analytical expression for the smoothing function between two Nusselt heights is given later in Equation (3.3.1). A schematic of the smoothing, as well as a summary of the boundary conditions, is given in Figure 11 where a smoothed profile joins different Nusselt depths h_l and h_r. The left hand boundary conditions are enforced as

$$\left.\begin{aligned} h &= h_l, \\ \frac{\partial h}{\partial x} &= 0, \\ \frac{\partial q}{\partial x} &= 0, \end{aligned}\right\} \quad \text{at} \quad x = x_0 \tag{2.4.1}$$

and the right hand boundary as

$$\frac{\partial h}{\partial x} = 0 \quad \text{at} \quad x = x_n. \tag{2.4.2}$$

The boundary conditions given in (2.4.1) and (2.4.2) are imposed in each of the various cases studied in Chapters 3-3.4 with the film height of the left

hand boundary h_l assumed to be a constant. Within Chapter 5, in which solitary waves are investigated, the value of h_l is a function of time.

At each time iteration step the right hand boundary film height $h(x_n)$ (equivalent to h_n) is calculated as a function of $h(x_{n-1})$ and $h(x_{n-2})$ given later in (2.4.8). Through application of the uniformity boundary condition $\frac{\partial h}{\partial x}(x_n, t) = 0$, this ultimately remains at the Nusselt height h_r. This is a consequence of calculations being restricted to ensure that the wave structures within the interior of the domain do not reach the boundary and disturb the uniformity conditions. The value of flux q_n on the right hand boundary is calculated through the cubic definition given in (2.1.7) as

$$q_n = \frac{\lambda h_n^3}{3} \sin\theta + \left(\frac{\tau}{2} + \alpha\lambda \sin\theta\right) h_n^2 + (\alpha\tau - 1)h_n. \tag{2.4.3}$$

A backward finite difference formulation provides the basis of the calculation of h_n and more detail is described in Subsection 2.4.2. The right hand boundary is termed the hydraulic control section, from which the fluid flux influences flow dynamics throughout the domain. The initial flux within the interior of the domain, $q(x_i, 0)$, is calculated using (2.1.7) substituting values of the initial profile heights $h(x_i, 0)$, for $i = 1 \ldots n - 1$.

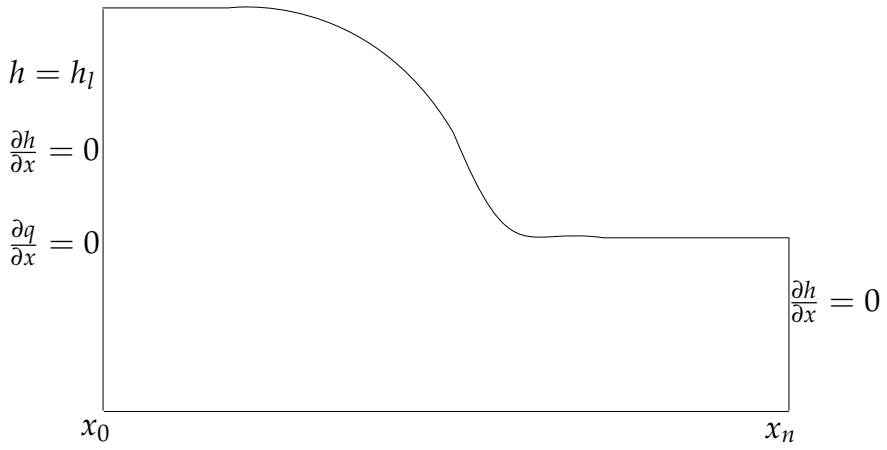


Figure 11.: Schematic of numerical domain and boundary conditions

2.4.2 *Finite difference method*

A finite difference approach is used to calculate the approximate values of the spatial derivatives at each of the interior points. This method is chosen due to its relative simplicity given the complexity and highly nonlinear nature of the governing equations to be solved. However, one should be aware of the need for uniform grid spacing leading to a large number of nodes, even if a high density of nodes is required to resolve a feature within only a small section of the domain. Regions which require greater detail and consequently a greater number of spatial nodes dictate the mesh density of the entirety of the domain when using a uniformly spaced mesh.

A linear upwind differencing scheme (LUDS) provides a second-order approximation of the first derivative of film height, $\frac{\partial h}{\partial x}$. An upwind finite difference stencil is used to give a direction-sensitive numerical approximation to simulate the direction of convection. The LUDS is a generalisation of the first order upwind differencing scheme (UDS) [36]. A first order scheme approximates the value of the convected variable at a location by its value at the first upstream node. Within a second order scheme, linear extrapolation, based on the values of the variable at the two upstream nodes, is used to calculate the convected variable value. In general, the second order LUDS reduces the numerical diffusion compared to a first-order UDS. An alternative scheme considered that gives third-order accuracy through two upstream nodes and one downstream node is the QUICK scheme. This however, may give rise to oscillations in the solution in regions where the gradient of the variable being solved is large [2], such as in the vicinity of wave fronts within the context of this thesis. The QUICK scheme was avoided as it may exaggerate the amplitude of the capillary ripples known to form at the base of a shock, or even cause the numerical instabilities. For

an interior stencil point i, the second order LUDS approximations are given by

$$V\frac{\partial h}{\partial x}(x_i) = V\left(\frac{3h_i - 4h_{i-1} + h_{i-2}}{2\Delta x} + \mathcal{O}(\Delta x^2)\right) \quad \text{if} \quad V > 0,$$
$$V\frac{\partial h}{\partial x}(x_i) = V\left(\frac{-h_{i+2} + 4h_{i+1} - 3h_i}{2\Delta x} + \mathcal{O}(\Delta x^2)\right) \quad \text{if} \quad V < 0, \tag{2.4.4}$$

where the subscripts are dictated by the direction of convection. Where the convective term V is negative, the first of the two approximations in (2.4.4) is used and, if positive, the second. To reduce the complexity of the numerical system the continuity equation (2.3.14) is manipulated as

$$\frac{\partial q}{\partial x} = -\frac{\partial h}{\partial t} \tag{2.4.5}$$

and together with the momentum equation (2.3.13) gives

$$\mathrm{Re}^*\left(\frac{\partial q}{\partial t} + I_h\frac{\partial h}{\partial x} - I_q\frac{\partial h}{\partial t}\right) - \lambda h\sin\theta - \tau + \frac{\partial u}{\partial y}\Big|_{y=0} + \varepsilon\lambda h\cos\theta\frac{\partial h}{\partial x} - \frac{\varepsilon^3}{\mathrm{Ca}}h\frac{\partial^3 h}{\partial x^3} = 0. \tag{2.4.6}$$

This averts the need for upwinding on $\frac{\partial q}{\partial x}$. The terms which require upwind discretisation in the momentum equation are $I_h\frac{\partial h}{\partial x}$, dependent on whether I_h is positive or negative, and $\varepsilon\lambda h\cos\theta\frac{\partial h}{\partial x}$, where $\varepsilon\lambda h\cos\theta > 0$ for all cases considered.

The first derivative of film flux, $\frac{\partial q}{\partial x}$ and the third derivative $\frac{\partial^3 h}{\partial x^3}$ are given by second order central difference formulae as

$$\frac{\partial q}{\partial x}(x_i) = \frac{-q_{i-1} + q_{i+1}}{2\Delta x},$$
$$\frac{\partial^3 h}{\partial x^3}(x_i) = \frac{h_{i-2} + 2h_{i-1} - 2h_{i+1} + h_{i+2}}{2\Delta x^3} \tag{2.4.7}$$

respectively [17]. It is assumed that the film profile is sufficiently constant at the boundaries of the computation domain that all derivatives are zero at $i = 0$ and $i = n$.

A standard finite difference discretisation for nodes towards the extremities of the computational domain is used and so the technique of using

"ghost nodes" is employed [12]. The ghost nodes are used in the discretisation of the third derivative $\frac{\partial^3 h}{\partial x^3}(x_1)$. Additionally, the relevant forward and backward formulations are also used to express boundary nodes in terms of interior variables. A similar technique is used by Chen [12] to remove dependence on the boundary variables. The height of the right hand side boundary, h_n, is assumed unknown but does not feature as a variable to be solved for within the numerical solver. Utilising the boundary condition of a uniform profile, backward differences are used at $i = n$ to express h_n as

$$h_n = -\frac{1}{3}h_{n-2} + \frac{4}{3}h_{n-1}. \tag{2.4.8}$$

Similarly, forward differences are used to express q_0 as

$$q_0 = \frac{4}{3}q_1 - \frac{1}{3}q_2. \tag{2.4.9}$$

These values are used within the discretisations of the spatial derivatives at nodes $i = 1$ and $i = n - 1$, giving

$$V\frac{\partial h}{\partial x}(x_1) = \frac{V}{\Delta x}\left(-2h_0 + 2h_1\right) \quad \text{if} \quad V > 0, \tag{2.4.10}$$

and

$$\begin{aligned} V\frac{\partial h}{\partial x}(x_{n-2}) &= \frac{V}{\Delta x}\left(-\frac{4}{3}h_{n-2} + \frac{4}{3}h_{n-1}\right), \\ V\frac{\partial h}{\partial x}(x_{n-1}) &= \frac{V}{\Delta x}\left(-\frac{1}{2}h_{n-2} + \frac{1}{2}h_{n-1}\right) \quad \text{if} \quad V < 0. \end{aligned} \tag{2.4.11}$$

Application of the ghost node technique is also used to give

$$\begin{aligned} \frac{\partial^3 h}{\partial x^3}(x_1) &= \frac{1}{\Delta x^3}\left(h_0 - \frac{1}{2}h_1 - h_2 + \frac{1}{2}h_3\right), \\ \frac{\partial^3 h}{\partial x^3}(x_{n-2}) &= \frac{1}{\Delta x^3}\left(-\frac{1}{2}h_{n-4} + h_{n-3} - \frac{1}{6}h_{n-2} - \frac{1}{3}h_{n-1}\right), \\ \frac{\partial^3 h}{\partial x^3}(x_{n-1}) &= \frac{1}{\Delta x^3}\left(-\frac{1}{2}h_{n-3} + \frac{7}{6}h_{n-2} - \frac{2}{3}h_{n-1}\right). \end{aligned} \tag{2.4.12}$$

The first spatial derivative of q at node $i = 1$ uses (2.4.9) may be simplified to

$$\frac{\partial q}{\partial x}(x_1) = \frac{1}{\Delta x}\left(-\frac{2}{3}q_1 + \frac{2}{3}q_2\right), \tag{2.4.13}$$

but this is overwritten by $\frac{\partial q}{\partial x}(x_1) = 0$ being enforced on the boundary. Thus, the spatial derivatives of both h and q are discretised in terms of the interior variables h_i and q_i, for $i = 1, \ldots, n-1$.

2.4.3 *Transient solver*

An implicit (backward) first-order Euler method [27] is used to approximate time variation in both the momentum and continuity equations. An implicit scheme is chosen, as opposed to the simpler explicit forward Euler method, for its comparative stability - see Kondic [27]. The backward Euler method computes a first-order time derivative approximations at $t = k + 1$ using

$$\frac{y_{k+1} - y_k}{\Delta t} = f(t_{k+1}, y_{k+1}), \tag{2.4.14}$$

given the form $\frac{\partial y}{\partial t} = f(t, y)$, where Δt is the time-step. For the equations required to be solved in this thesis, f is a nonlinear function.

The finite difference approximations together with the implicit Euler scheme yield a general system of $2(n-1)$ nonlinear equations for values of grid variables $h_1, \ldots, h_{n-1}$ and $q_1, \ldots, q_{n-1}$. Unknowns h_n and q_n are calculated post-solution using the equations given in (2.4.8) and (2.4.3); correspondingly these do not feature as independent variables within the algebraic system of equations to be solved. Kondic [27] gives a variation of the Newton method for solving equations of the form in (2.4.14), used here to find a solution at each time-step. For a $(2n-2)$-dimensional system, the equations to be solved may be expressed concisely as a nonlinear vector equation

$$\mathbf{F}(\mathbf{X}) = \mathbf{0}, \tag{2.4.15}$$

where $\mathbf{X} = [h_1, \ldots, h_{n-1}, q_1, \ldots, q_{n-1}]$ is the concatenated column vector of the independent variables, and $\mathbf{F} : \mathbb{R}^{2n-2} \to \mathbb{R}^{2n-2}$ is the concatenated column vector of the functions $\mathcal{C}_i$ and $\mathcal{M}_i$ for $i = 1, \ldots, n-1$. $\mathcal{C}_i$ and $\mathcal{M}_i$ refer to the discretised continuity and momentum equations respectively at the i^{th} node. If $\mathbf{X}^k$ is the k^{th} approximation to the solution of (2.4.15), an iterative solution based on Newton's method is defined by Broyden [7] as

$$\mathbf{X}^{k+1} = \mathbf{X}^k - \mathbf{J}^{-1}\mathbf{F}(\mathbf{X}^k). \tag{2.4.16}$$

For computational ease this can be rearranged to give

$$\mathbf{J}(\mathbf{X}^k)(\mathbf{X}^{k+1} - \mathbf{X}^k) = -\mathbf{F}(\mathbf{X}^k) \tag{2.4.17}$$

where $\mathbf{J}$ is the Jacobian matrix of F given by

$$\mathbf{J} = \begin{pmatrix} \frac{\partial \mathcal{C}_1}{\partial h_1} & \cdots & \frac{\partial \mathcal{C}_1}{\partial h_{n-1}} & \frac{\partial \mathcal{C}_1}{\partial q_1} & \cdots & \frac{\partial \mathcal{C}_1}{\partial q_{n-1}} \\ \vdots & \ddots & \vdots & \vdots & \ddots & \vdots \\ \frac{\partial \mathcal{C}_{n-1}}{\partial h_1} & \cdots & \frac{\partial \mathcal{C}_{n-1}}{\partial h_{n-1}} & \frac{\partial \mathcal{C}_{n-1}}{\partial q_1} & \cdots & \frac{\partial \mathcal{C}_{n-1}}{\partial q_{n-1}} \\ \frac{\partial \mathcal{M}_1}{\partial h_1} & \cdots & \frac{\partial \mathcal{M}_1}{\partial h_{n-1}} & \frac{\partial \mathcal{M}_1}{\partial q_1} & \cdots & \frac{\partial \mathcal{M}_1}{\partial q_{n-1}} \\ \vdots & \ddots & \vdots & \vdots & \ddots & \vdots \\ \frac{\partial \mathcal{M}_{n-1}}{\partial h_1} & \cdots & \frac{\partial \mathcal{M}_{n-1}}{\partial h_{n-1}} & \frac{\partial \mathcal{M}_{n-1}}{\partial q_1} & \cdots & \frac{\partial \mathcal{M}_{n-1}}{\partial q_{n-1}} \end{pmatrix}. \tag{2.4.18}$$

Algebraic rearrangement of (2.4.16) into the form given in (2.4.17) has the advantage that the inverse of the Jacobian matrix need not be explicitly calculated. This approach however requires calculating the entries within the matrix $\mathbf{J}$. Further detail on the analytically calculated Jacobian matrix is given in Appendix A. This matrix system, of the form $\mathbf{AX} = \mathbf{B}$, is solved using the Matlab function *mldivide*, which uses an inbuilt algorithm to decide on the best method of solution. *mldivide* is able to minimise computation time through its ability to consider the sparsity and symmetry in the problem before dispatching to the appropriate solver. The Matlab solver returns the value of $(\mathbf{X}^{k+1} - \mathbf{X}^k)$, from which the updated solution vector $\mathbf{X}^{k+1}$ may be recovered. As with other Newton-method-based iterative procedures, quadratic convergence is anticipated given a suitable initial guess.

The initial profile for the first time-step is chosen as a smoothed function dependent on Nusselt values of h and the corresponding values of q as calculated by Equation (2.1.7). Starting profiles for the iterative Newton's method at subsequent time-steps are taken as the converged solution from the previous time iteration. Δx is chosen such that the mesh is dense enough to resolve the short-wavelength capillary region smoothly, whilst Δt is chosen to ensure robust and progressive evolution of the film profile. In general, a fixed relationship was not observed between Δx and Δt, although a formal investigation was not conducted into this. Initial evaluation of the numerical scheme was undertaken and showed that the steepest sections of a film profile are generally observed developing rapidly from the smooth initial profiles in comparison to the development and evolution of the re-

mainder of the film. The capillary region at the base of the primary peak of a wave structure is also generally the point within the entire domain with the steepest spatial gradient. If values of either Δx or Δt are chosen to be too large, the solution displays a negative value of h within the capillary region, representative of film rupture, soon after initiation. This results in numerical singularities and a blow-up of the simulation, and so is used as a guide for choosing the correct values of these numerical parameters. Thus, for an accurate numerical solution, this requires choosing sufficient nodal density to resolve the predicted capillary region. If a breakdown of the solution is observed, the simulation is rerun with a shorter time step and a higher mesh density. A drawback of increasing the mesh density is that not only is there a larger system of equations to be solved, but the memory requirements also increase proportionally. The issue of computational memory was minimised to a large extent by utilising the sparse nature of the diagonally structured Jacobian matrix, illustrated in Figure 12. Nevertheless, the computational time required to solve the system was still considerable.

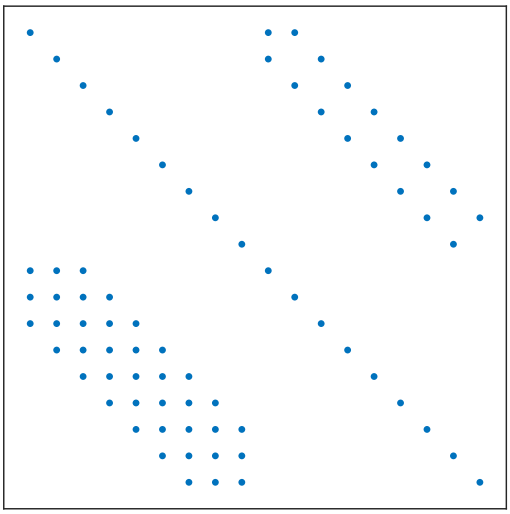


Figure 12.: Illustration of the sparse structure of the Jacobian matrix

3

INERTIAL EFFECTS ON SHEAR-DRIVEN FILM FLOW

In this chapter thin-film flow is considered subject to a constant shear on the free surface with a no-slip condition imposed on the boundary between the fluid and the plane. Profiles of this nature may be compared to those obtained by Bertozzi et al. [6], Levy et al. [28] and Shuaib et al. [49], all of whom investigated similar geometric models in the absence of inertial terms within their formulation.

3.1 FILM EVOLUTION EQUATIONS USING A QUADRATIC VELOCITY PROFILE

The fluid-plane boundary condition (2.0.14) becomes

$$u = -1 \quad \text{on} \quad y = 0 \tag{3.1.1}$$

when the dimensionless slip length $\alpha = 0$. This reflects the fact that the system is viewed within a travelling frame of reference, and so the plane appears to move in the negative x-direction.

A film velocity profile in the form of a polynomial is a common assumption and so is incorporated into the governing equations. The number of degrees of freedom of this polynomial is considered in evaluating the accuracy of the numerical solutions. The expression (2.1.6) for the streamwise velocity $u(y)$ in uniform flow on the plane shows the quadratic nature of the film profile, and so a quadratic profile is anticipated to be an accurate

approximation in regions of near-uniform flow. In regions with larger amplitude disturbances and steeper wave features there have been numerous previous studies both experimental and theoretical. These studies suggest there exist areas of backflow and fluid recirculation, and that a polynomial of cubic or even higher order may be more accurate. Figure 6 shows the streamwise velocity profile as computed by Malamataris et al. [32] for successive locations within the primary of a wave structure and the capillary region. It is noted that some profiles show several points of inflexion, indicative of fluid velocity profiles more complex than quadratic. However, most profiles show good agreement with a quadratic flow in the majority of the domain.

We assume a quadratic general velocity profile at $\mathcal{O}(1)$ of the form

$$u = a_0 + a_1 y + a_2 y^2, \tag{3.1.2}$$

where the coefficients a_0, a_1 and a_2 are to be determined. The coefficients are calculated using a specified surface shear τ on $y = h$, the no-slip condition on $y = 0$, and specified volume flux q. Application of these conditions result in a set of simultaneous algebraic equations

$$\begin{aligned} &a_1 + 2a_2 h = \tau, \\ &a_0 = -1, \\ &a_0 h + a_1 \frac{h^2}{2} + a_2 \frac{h^3}{3} = q. \end{aligned} \tag{3.1.3}$$

Solution of the equations in (3.1.3) gives expressions involving h and q for the profile coefficients as

$$\begin{aligned} a_0 &= -1, \\ a_1 &= \frac{3}{h} - \frac{\tau}{2} + \frac{3q}{h^2}, \\ a_2 &= -\frac{3}{2h^2} + \frac{3\tau}{4h} - \frac{3q}{2h^3}. \end{aligned} \tag{3.1.4}$$

The expression for the velocity profile of fluid within the film is now given as

$$u = \frac{3(h^2\tau - 2h - 2q)}{4h^3} y^2 - \frac{h^2\tau - 6h - 6q}{2h^2} y - 1. \tag{3.1.5}$$

This is consistent with Nguyen and Balakotaiah [34], who use a stream function of the form $\psi(x,y,t) = A(x,t)y^2 + B(x,t)y^3$, corresponding to a quadratic velocity profile through the relationship $u = \frac{\partial \psi}{\partial y}$. Differences in the constant term a_0 arise through the choice of either a stationary or a travelling frame of reference.

The profile (3.1.2) is used to evaluate the integral term $\frac{\partial}{\partial x}\int_0^h u^2 \, \mathrm{d}y$ in Equation (3.1.6), the depth-averaged momentum equation,

$$\mathrm{Re}^* \left(\frac{\partial q}{\partial t} + \frac{\partial}{\partial x} \int_0^h u^2 \, \mathrm{d}y \right) = \lambda h \sin\theta + \tau - \frac{\partial u}{\partial y}\Big|_{y=0} - \varepsilon \lambda h \frac{\partial h}{\partial x} \cos\theta + \frac{\varepsilon^3}{\mathrm{Ca}} h \frac{\partial^3 h}{\partial x^3}, \tag{3.1.6}$$

as derived in Chapter 2. By substitution and simplification of the associated algebra, (3.1.6) can be written as

$$\mathrm{Re}^* \left(\frac{\partial q}{\partial t} + I_h \frac{\partial h}{\partial x} + I_q \frac{\partial q}{\partial x} \right) = \lambda h \sin\theta - \frac{3}{h} + \frac{3\tau}{2} - \frac{3q}{h^2} - \varepsilon \lambda h \cos\theta \frac{\partial h}{\partial x} + \frac{\varepsilon^3}{\mathrm{Ca}} h \frac{\partial^3 h}{\partial x^3}, \tag{3.1.7}$$

where I_h and I_q, calculated through integration of the square of the velocity profile as in (2.3.11), are functions of h, q and τ. Values are highly nonlinear expressions given by

$$I_h = \frac{4h^3\tau + h^4\tau^2 - 48q^2 + 2qh^2\tau + 8h^2}{40h^2} \quad \text{and} \quad I_q = \frac{8h + h^2\tau + 48q}{20h}. \tag{3.1.8}$$

The depth-averaged continuity equation (2.3.4) and the depth-averaged momentum equation (3.1.7) compare with the coupled partial differential equations of the Shkadov model [48]. The system of equations (2.3.4) and (3.1.7) is used for the numerical simulation of moving shock structures on thin films that are subject to imposed exterior surface shear. Differences between the present formulation and the Shkadov model are slight, however their implications on the numerical simulations that follow are significant. A key difference is that the Shkadov model does not incorporate surface shear ($\tau = 0$). The inclusion of surface shear, as shown later in Section 3.3.1, leads to stabilisation of the capillary ripples and allows numerical simulations to be attained at higher Reynolds numbers. This is possible as

a consequence of the smaller amplitude, larger wavelength capillary ripples requiring few mesh nodes to resolve numerically.

Film height and film flux for shear-driven flow are given from solving

$$\mathrm{Re}^* \left(\frac{\partial q}{\partial t} + I_h \frac{\partial h}{\partial x} - I_q \frac{\partial h}{\partial t} \right) - \lambda h \sin\theta + \frac{3}{h} - \frac{3\tau}{2} + \frac{3q}{h^2} + \varepsilon\lambda h \cos\theta \frac{\partial h}{\partial x} - \frac{\varepsilon^3}{\mathrm{Ca}} h \frac{\partial^3 h}{\partial x^3} = 0 \tag{3.1.9}$$

and

$$\frac{\partial h}{\partial t} + \frac{\partial q}{\partial x} = 0. \tag{3.1.10}$$

The governing equations are mathematically subject to general constant far-field boundary conditions

$$h = h_l,\, q = q_l \quad \text{as} \quad x \to -\infty \tag{3.1.11}$$

and

$$h = h_r,\, q = q_r \quad \text{as} \quad x \to \infty. \tag{3.1.12}$$

Solutions obtained from the inertial model developed in this study are compared against the non-inertial limiting case film profiles obtained in previous literature. Shuaib [49] has investigated a similar problem in the context of Stokes flow. Taking $\mathrm{Re} = 0$ gives an expression for flux,

$$q = \frac{h^2}{3} \left(\lambda h \sin\theta - \frac{3}{h} + \frac{3\tau}{2} - \varepsilon\lambda h \cos\theta \frac{\partial h}{\partial x} + \frac{\varepsilon^3}{\mathrm{Ca}} h \frac{\partial^3 h}{\partial x^3} \right), \tag{3.1.13}$$

and insertion of (3.1.13) into (3.1.10) yields, in dimensionless form,

$$\frac{\partial h}{\partial t} + \frac{\partial}{\partial x} \left(\frac{1}{2}\tau h^2 + \frac{1}{3}\lambda h^3 \sin\theta \right) = \frac{\varepsilon^3}{3\,\mathrm{Ca}} \frac{\partial}{\partial x} \left(h^3 \frac{\partial^3 h}{\partial x^3} \right) + \frac{\partial}{\partial x} \left(\frac{1}{3}\varepsilon\lambda h^3 \cos\theta \frac{\partial h}{\partial x} \right) + \frac{\partial h}{\partial x}. \tag{3.1.14}$$

Equation (3.1.14) is comparable to the evolution equation for the film thickness h in [49]

$$\frac{\partial h}{\partial t} + \frac{\partial}{\partial x} \left(\frac{\gamma h^2}{2} + \frac{\sin\theta}{3} h \right) = -\frac{1}{\mathrm{Ca}} \frac{\partial}{\partial x} \left(\frac{h^3}{3} \frac{\partial^3 h}{\partial x^3} \right) + \frac{\partial}{\partial x} \left(\frac{\cos\theta}{3} h^3 \frac{\partial h}{\partial x} \right), \tag{3.1.15}$$

given appropriate choice of parameter values. Shuaib uses γ to signify dimensionless shear stress. Hence, solutions obtained by Shuaib correspond

Parameter	Value
λ	1
Ca	1×10^{-4}
τ	2.14914
q	-0.2068
ε	1×10^{-2}
α	1

Table 2.: Dimensionless parameter values corresponding to those used by Shuaib et al. [49].

to setting the reduced Reynolds number to be zero (Stokes flow) and choosing parameters within the current model as in Table 2.

For a given slope inclination, conjugate values of the Nusselt heights are calculated by specifying flux q, surface shear, τ, and gravity parameter, λ. The cubic equation in h for constant flux q (2.1.7), with $\alpha = 0$, is

$$q = \frac{\lambda h^3}{3} \sin\theta + \frac{\tau}{2} h^2 - h. \tag{3.1.16}$$

Solving Equation (3.1.16) yields h_1, h_2 and h_3 (see Table 3) and may theoretically coexist for appropriate values of τ.

τ	θ	h_1	h_2	h_3
2	-45	0.2801	1.0910	2.8716
2.14914	-45	0.2933	0.8848	3.3809
2.2	-45	0.2986	0.8305	3.5378
2.3	-45	0.3108	0.7367	3.8315
2.4	-45	0.3266	0.6535	4.1111
2.14914	-80	0.2822	1.2878	1.6975

Table 3.: Nusselt heights (to 4 decimal places). $q = -0.2068$ and $\lambda = 1$.

3.2 CLASSIFICATION OF FILM PROFILES

A reference velocity U corresponding to the dimensional velocity of the wall is calculated by inserting the dimensional equivalent of the cubic expression (3.1.16) into the Rankine-Hugoniot condition $S = \frac{Q_- - Q_+}{H_- - H_+}$. The flux in (1.2.5) corresponds to a stationary reference system, and so the substitution $\hat{q} = q + h$ is made, where $\hat{q}$ and q are in the fluxes in the stationary and moving reference frames respectively. With the appropriate algebraic manipulation,

$$U = \left(\frac{\rho g \sin\theta H^2}{3}\right)\left(\frac{1-b^3}{1-b}\right) + \left(\frac{\tau H}{2\mu}\right)\left(\frac{1-b^2}{1-b}\right) \tag{3.2.1}$$

is obtained, where b is the ratio of the film heights at the upper and lower ends of the plane respectively. The dimensional reference velocity U may be used to obtain more information about speed and direction of propagation of fronts to aid with classification of the different types of wave features. Within a moving frame of reference, the motion of perturbations relative to the front is considered. Classical shock waves, also termed Lax shocks, satisfy the Lax condition

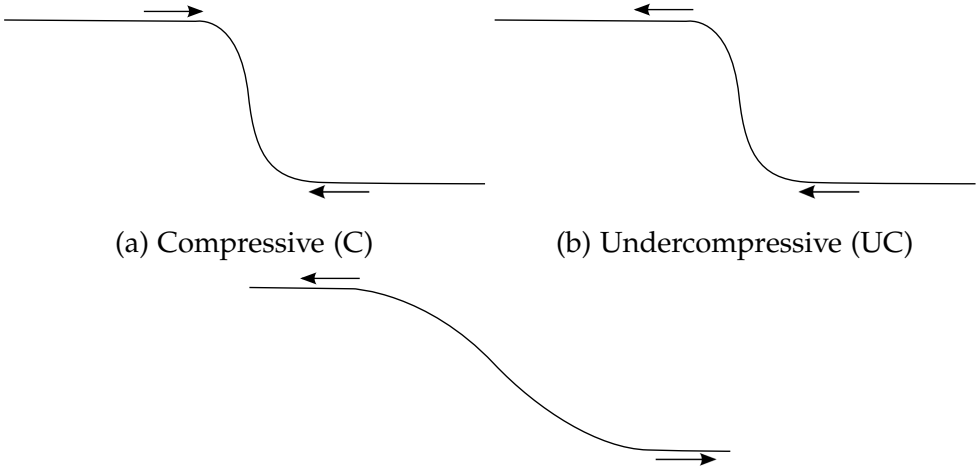
$$F_+ \leq S \leq F_-. \tag{3.2.2}$$

S is the shock velocity, F_- is the velocity at which perturbations travel within a film depth of H_-, and F_+ the velocity within a film depth of H_+. Perturbations on either side of a Lax shock travel towards the compressive front and impinge upon it (Figure 13a). A non-classical shock wave on the other hand satisfies the inequalities

$$S \geq F_- \quad \text{and} \quad S \geq F_+, \tag{3.2.3}$$

with perturbations on either side of an non-classical shock appearing to move through the undercompressive front, both disturbances propagating in the same direction (Figure 13b). Rarefaction waves are continuous surface profiles appearing to get smoother with time. Perturbations on either side moving away from the wave feature (Figure 13c). Figure 13 depicts

upstream facing structures with flow from right to left in a moving frame of reference. Downstream facing structures, with the higher film depth on the upstream (right hand) side, are classified as reverse compressive or reverse undercompressive.



(a) Compressive (C) (b) Undercompressive (UC)

(c) Rarefaction wave (Rw)

Figure 13.: Direction of propagation of perturbations as viewed in a moving frame of reference.

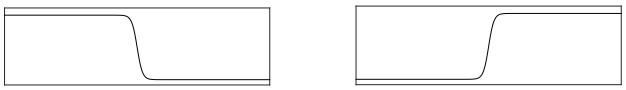
3.3 SHEAR-DRIVEN FILM PROFILES USING A QUADRATIC VELOCITY PROFILE

Wave structures are instigated from defining an initial film profile and the evolution of standing waves and transient film profiles is investigated. Two-tier initial profiles are illustrated in figures 14a and 14b that involve a choice of two of the conjugate heights $h_1 < h_2 < h_3$ for given values of θ and τ. Figures 15a to 15f illustrate three-tier initial profiles involving all three Nusselt heights. For ease of notation, we label the height of the initial film profile on the left hand side of the domain is labelled h_l, height on the right hand side h_r and, if applicable, the height of the middle tier h_m. The heights of boundary and initial tiers are denoted with h_1, h_2 or h_3, corresponding to the Nusselt values in Table 3. A simple translation of a hyperbolic tangent

function is used to create a smooth two-tier initial profile between h_l and h_r using

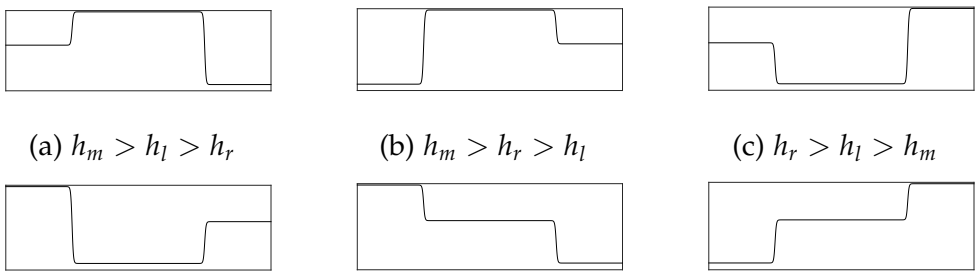
$$h = -\frac{h_l - h_r}{2} \tanh\left(kx - \frac{L}{2}\right) + \frac{h_l + h_r}{2} \tag{3.3.1}$$

and a three-tier initial profile is formed through merging multiple two-tier profiles.



(a) $h_l > h_r$ (b) $h_l < h_r$

Figure 14.: Two-tier initial profiles



(a) $h_m > h_l > h_r$ (b) $h_m > h_r > h_l$ (c) $h_r > h_l > h_m$

(d) $h_l > h_r > h_m$ (e) $h_l > h_m > h_r$ (f) $h_l < h_m < h_r$

Figure 15.: Three-tier initial profiles

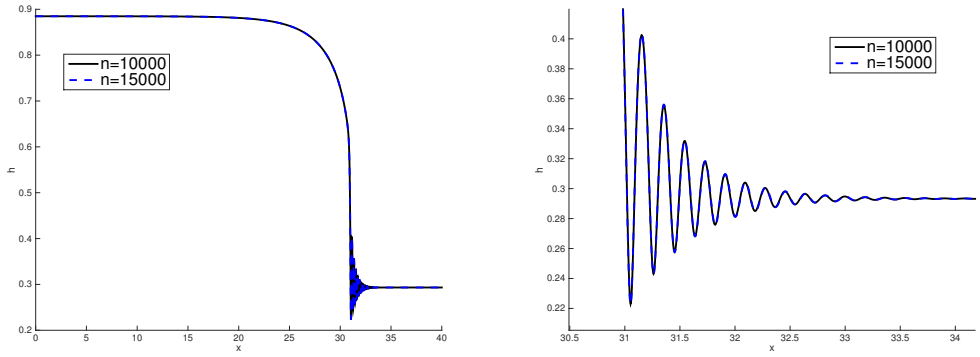
Results included within this chapter are for a moderate angle of inclination $\theta = -45$ and a steeper angle $\theta = -80$. Wave features within profiles are classified as: compressive (C), reverse compressive (RC), undercompressive (UC), reverse undercompressive (RUC) or a rarefaction wave (Rw).

Solutions reported in Chapters 3-3.4 that appear as stationary are standing shocks moving up the plane with the reference velocity (3.2.1) in the corresponding fixed physical coordinate system, while those that appear as travelling fronts are moving faster or slower than the reference velocity U. In all the cases reported within this chapter, the imposed surface shear overcomes the gravitational force and the resulting fronts always move upwardly in the plane, in the positive x-direction.

3.3.1 *Smoothing effects of inertia*

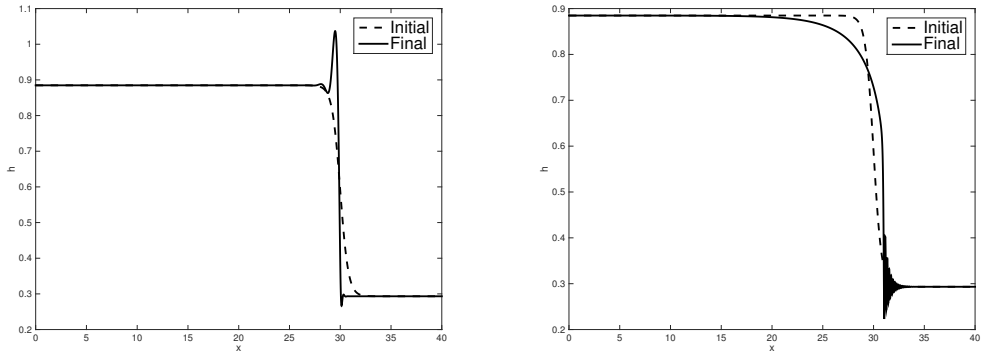
An initial film profile of the form in Figure 14a develops into a compressive wave-front under initial conditions where $h_l = h_2$ and $h_r = h_1$, as shown in Figure 17. Results are comparable to the non-inertial profiles reported by Levy and Shearer [28], and Shuaib [49]. Increasing the Reynolds number results in a smoothing of the film profile at the top of the shock. This is an expected consequence of increasing inertial effects since the internal flow will tend towards moving with smoothed streamlines in this region (see Figure 21) rather than in a similar fashion to those seen in Figure 20. In addition, the formation of very short wavelength capillary ripples at its base is found, as shown in Figure 17b. The capillary waves are also present in profiles obtained in other numerical studies which include the effects of inertia [43], as well as observed in experimental work by Kofman et al. [26]. These capillary ripples are mesh-independent, indicating this is a model feature. This is shown in Figure 16, where both the overall profile structure and a close up of the capillary region for both $n = 10000$ and $n = 15000$ are provided, n being the number of grid points within the domain shown. Increasing the mesh density beyond a certain threshold does not change the shape of the profile any further, with both profiles overlapping exactly.

Further investigations were carried out by varying the surface shear. As previously noted for Figure 10, there is a limitation to the range of values of τ in order to support three conjugate film depths. Expanded plots of the capillary ripples for three different values of τ are given in Figure 18. It can be seen in both this figure and in Figure 19 that with increasing surface shear, the wavelength of the capillary ripples also increases, while the amplitude decreases. The wavelength of the first capillary ripple increases from 0.09 for $\tau = 2$, to 0.13 for $\tau = 2.4$, whilst the amplitude decreases from 0.1993 to 0.1262. This aids with numerical stability of the solution and hence, solutions for the full range of values for which our approximation $\mathrm{Re} \sim \mathcal{O}\left(\frac{1}{\varepsilon}\right)$ is valid were achievable without any finite-time singularities.



(a) Overall profile structure (b) Expanded view of capillary region

Figure 16.: Wave structure for two different mesh densities, highlighting mesh-independence.

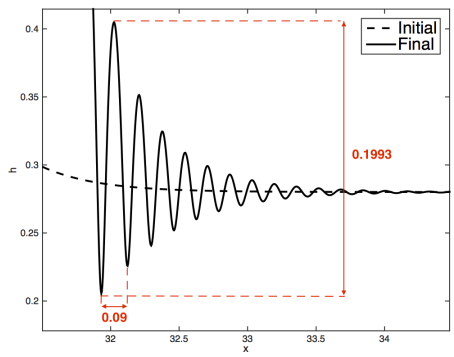


(a) $\mathrm{Re}^* = 0$ (b) $\mathrm{Re}^* = 10$

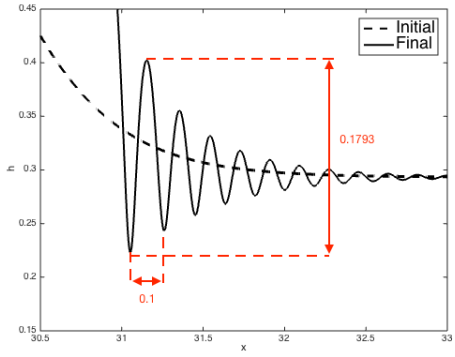
Figure 17.: Compressive. $\theta = -45$, $h_l = h_2$, $h_r = h_1$.

Fluid flow may be characterised by the velocity vector field within the film. A velocity field, within a moving frame of reference in this instance, gives a clear indication of the direction of travel of fluid particles and provides a more detailed picture of any regions within which fluid is recirculating. Additionally a plot of streamlines as a family of curves which are tangential to the velocity vector of the flow and indicate the direction in which a fluid element will travel at any point in time is informative.

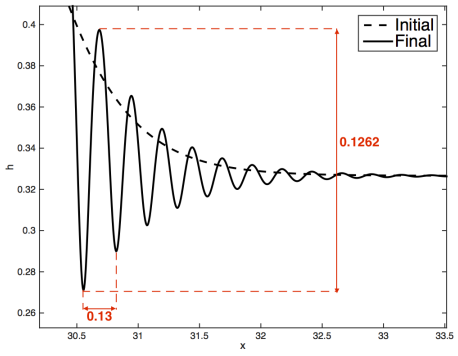
The full evolved wave structure in Figure 17b, with $h_l = h_2$, $h_r = h_1$ and $\mathrm{Re}^* = 10$ is now considered as an example case. The assumed quadratic



(a) $\tau = 2$



(b) $\tau = 2.14914$ (Figure 17b)



(c) $\tau = 2.4$

Figure 18.: Capillary waves for increasing values of τ. $\theta = -45$, $\mathrm{Re}^* = 10$.

velocity profile $u = a_0 + a_1 y + a_2 y^2$ can be reconstructed to give information about the velocity of the fluid parallel to the plane. However, by the nature of a depth-averaged formulation, information about fluid velocities perpendicular to the plane is not initially known. An expression for $v(x)$ must be found through manipulation of the continuity equation and subsequent integration, with application of the no-penetration boundary condition between the fluid and the plane. Integrating

$$\begin{aligned} \frac{\partial v}{\partial y} &= -\frac{\partial u}{\partial x} \\ &= -\left(\frac{\partial a_0}{\partial x} + \frac{\partial a_1}{\partial x} y + \frac{\partial a_2}{\partial x} y^2\right) \end{aligned} \tag{3.3.2}$$

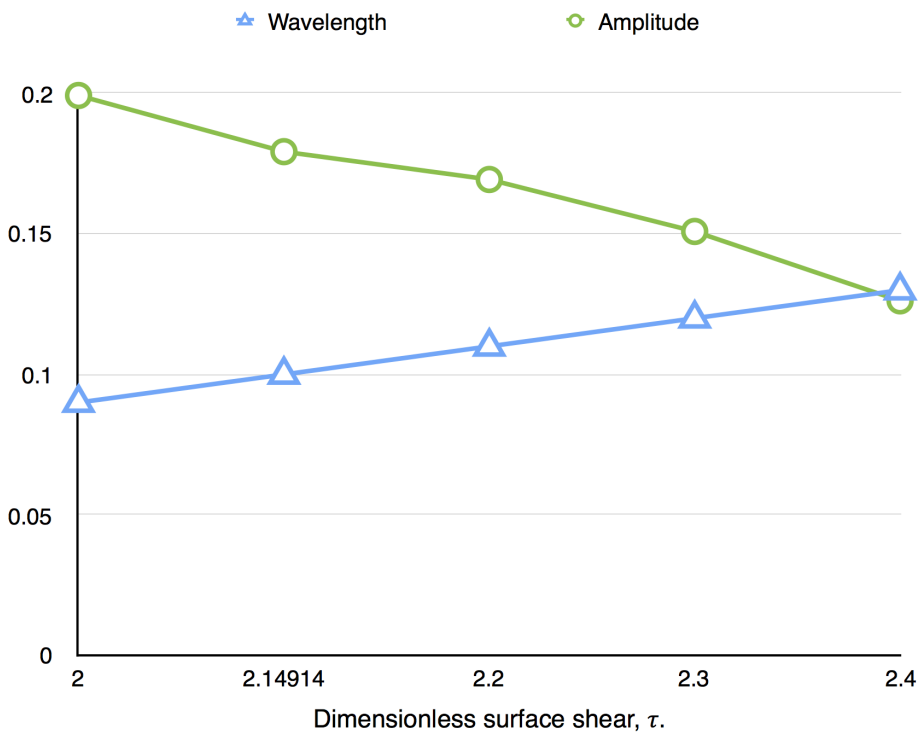


Figure 19.: Capillary wavelength increases and amplitude decreases with increasing surface shear. $\theta = -45$, $\mathrm{Re}^* = 10$.

gives

$$\begin{aligned} v &= \int -\left(\frac{\partial a_0}{\partial x} + \frac{\partial a_1}{\partial x} y + \frac{\partial a_2}{\partial x} y^2\right) \mathrm{d}y \\ &= -\left(\frac{\partial a_0}{\partial x} y + \frac{\partial a_1}{\partial x} \frac{y^2}{2} + \frac{\partial a_2}{\partial x} \frac{y^3}{3}\right) + c, \end{aligned} \tag{3.3.3}$$

where c is a constant to be determined. Using the no-penetration condition $v = 0$ on $y = 0$, an expression for the velocity perpendicular to the plane is obtained as

$$v = -\left(\frac{\partial a_0}{\partial x} y + \frac{\partial a_1}{\partial x} \frac{y^2}{2} + \frac{\partial a_2}{\partial x} \frac{y^3}{3}\right). \tag{3.3.4}$$

The partial derivatives of the profile coefficients are discretised within the domain using grid-based spacing and calculated using central difference formulation (3.3.5). For convenience, a common spacing Δx is used as in the original data for Figure 17, with an arbitrary choice of Δy, dependent

on the level of detail we require for the velocity vector map. Coefficients $\frac{\partial a_{i,j}}{\partial x}$ for $i = 0, 1, 2$ and $j = 1, \ldots, N-1$ are given by

$$\frac{\partial a_{i,j}}{\partial x} = \frac{-a_{i,j-1} + a_{i,j+1}}{2\Delta x}. \tag{3.3.5}$$

The discrete values of a_0, a_1 and a_2 are calculated at each grid point using definitions of the profile coefficients given in (3.1.4) and the discrete values of y. Once values for u and v at each grid point have been obtained, a velocity vector map is created, which can then be used to construct a streamline map using the Matlab function *streamline*.

Figure 20 using the technique described above to visualise the streamlines within the wave structure in 17a. The lack of inertia is evident at the top of the wave structure, with the streamlines significantly from a smooth line of motion. Figure 21 shows streamlines as seen within a moving frame of

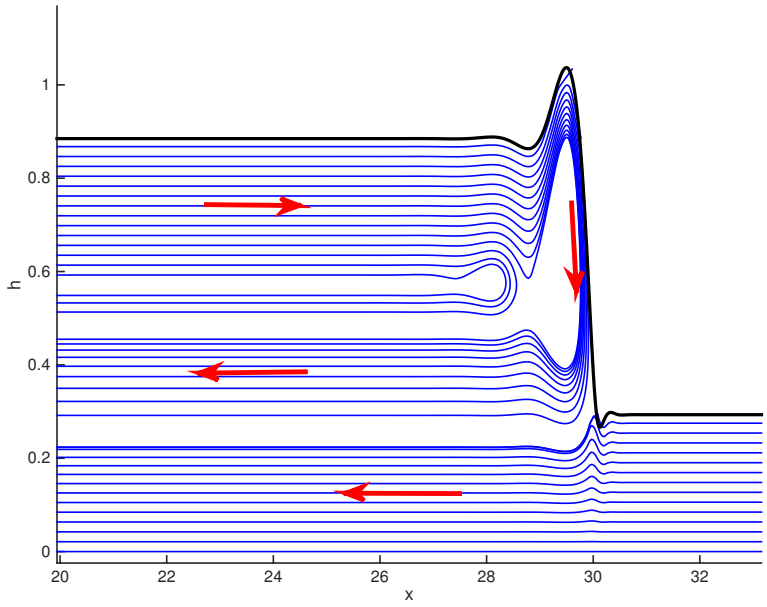


Figure 20.: Streamlines for wave structure in Figure 17a as viewed in a moving frame of reference. $\theta = -45$, $\mathrm{Re}^* = 0$.

reference for the wave structure in Figure 17b. We note that any particles which enter the domain from point A recirculate within the bore and exit back out of the wave front at B. The entire bore is seated on top of a base

flow with particle movement in the negative x-direction. Fluid enters at C and travelling straight across, disregarding the slight disturbances within the capillary region which eventually settle into steady parallel flow.

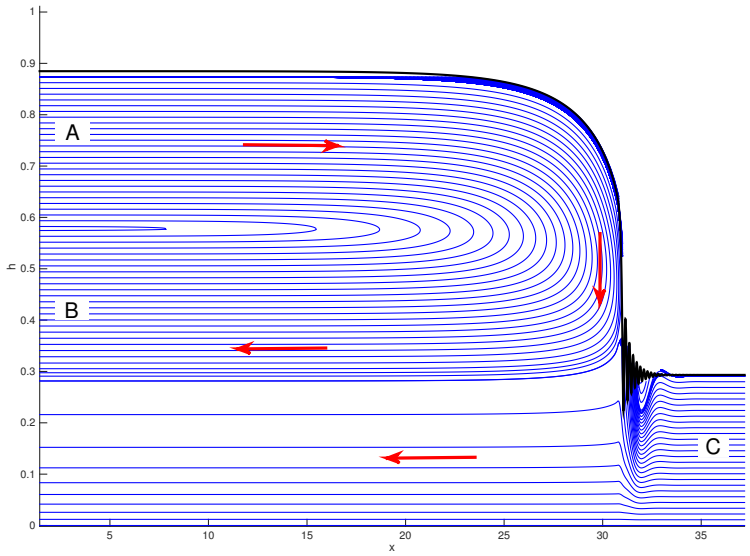
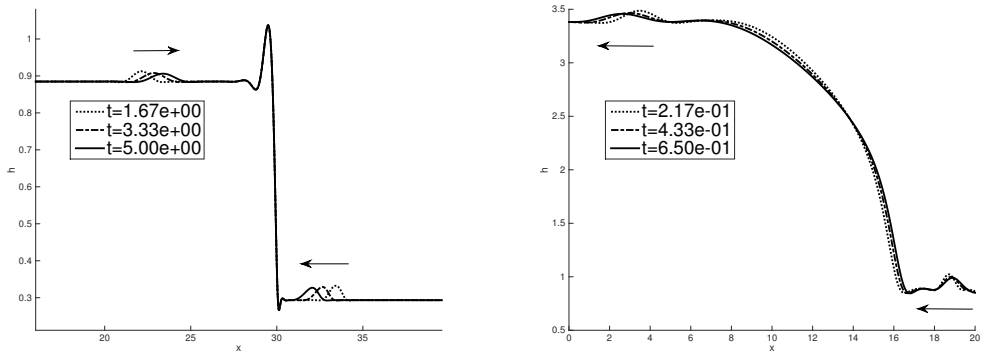


Figure 21.: Streamlines for wave structure in Figure 17b as viewed in a moving frame of reference. $\theta = -45$, $\mathrm{Re}^* = 10$.

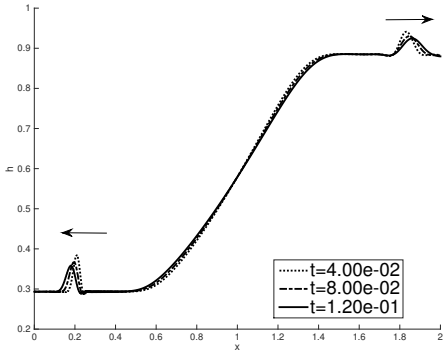
Wave structures are classified as compressive, undercompressive or a rarefaction wave using the direction of travel of perturbations. An example is given in Figure 22, corresponding to examples of film profile together with finite-amplitude perturbations on either side of the shock front. It can be seen that the perturbations on either side of the front are travelling towards the front in the moving frame of reference, and therefore this is classified as a compressive shock in Figure 22a; classified as an undercompressive front with perturbations travelling through the shock (noting motion relative to the front) in Figure 22b; and perturbations travelling away from the front in the rarefaction wave in Figure 22c.

Another point to note from Figure 22 is that the perturbations decay in amplitude as they travel towards the shock front without any numerical instability. This was found in all other cases investigated and reported



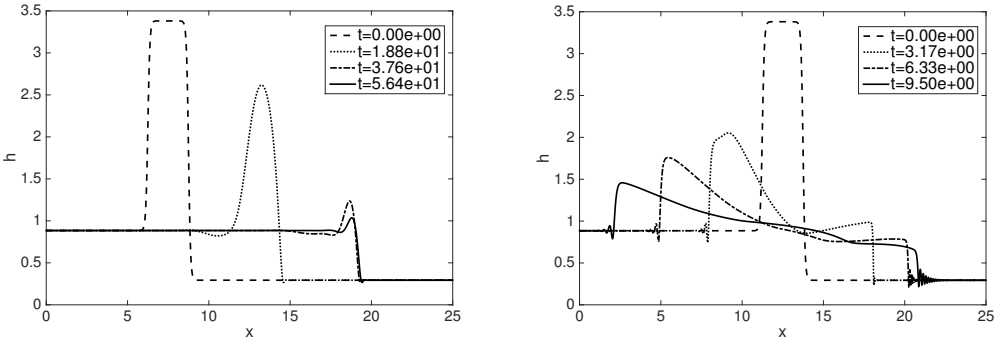
(a) Compressive

(b) Undercompressive



(c) Rarefactive

Figure 22.: Evolution of perturbations for different wave structures.



(a) $\mathrm{Re}^* = 0$

(b) $\mathrm{Re}^* = 10$

Figure 23.: (a) Compressive. (b) Reverse undercompressive - compressive. $\theta = -45$, $h_l = h_2$, $h_m = h_3$, $h_r = h_1$.

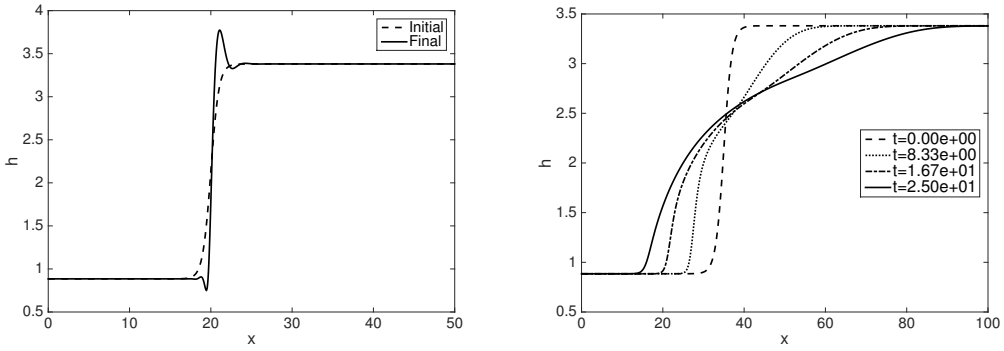
here, suggesting that film profiles are stable to finite-amplitude perturbations (nonlinear stability) and that imposing surface shear on the integral

boundary layer model makes it less susceptible to singularities and numerical instabilities than reported by the Shkadov model in previous literature.

Figure 23, with boundary conditions as in Figure 17, but an intermediate tier in the initial profile at $h_m = h_3$, shows the time development of a compressive wave front at $\mathrm{Re}^* = 0$. The initial peak in Figure 23a decreases in height steadily and tends towards the intermediate film conjugate height $h_2 = 0.8848$, eventually reaching a steady solution in a moving frame of reference, correlating to a travelling wave in a stationary frame of reference. Shuaib [49] also reports this type of wave profile with $\mathrm{Re}^* = 0$. When inertial effects are considered (Figure 23b); two wave fronts develop - a leading and a trailing front, giving a reverse undercompressive-compressive combination. The trailing (left hand) front, although appearing to propagate in the negative direction, in the corresponding fixed reference (stationary frame) system, is moving upwards with a velocity slower than the reference one while the right hand side corresponds to an under-compressive front moving faster than the reference velocity. Both the leading and the trailing fronts are travelling up the plane in a stationary frame of reference. The height of the trailing front in Figure 23b is decreasing with time, and it is anticipated that this will ultimately tend towards the height of the left hand boundary. The height of the front on the right hand side has also decreased with time and is tending towards a compressive shock front, noting also the capillary ripples at its base. The results in Figure 23 confirm uniqueness of solution with respect to Figure 17. As time progresses the film profiles in figures 23a and 23b tend to those in figures 17a and 17b respectively, corresponding to differences in the Reynolds numbers.

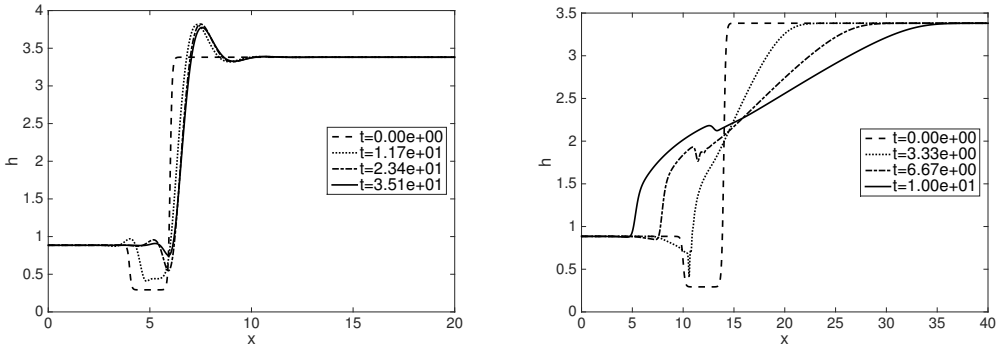
Figure 24, with boundary conditions $h_l = h_2$, $h_r = h_3$, illustrates the smoothing effect of inertia from an initial steep reverse compressive front for $\mathrm{Re}^* = 0$ with a profile that develops into a steady solution in a moving frame of reference, physically representing a standing wave travelling up the plane. With the inclusion of inertia the profile evolves with time, becoming smoother and in Figure 24b can be seen moving in the negative x direc-

tion at a dimensionless speed of 0.61. This is slower than the dimensionless reference velocity of -1, at which the entire system is moving, and so the net movement of this wave structure is up the plane, in the direction of the applied surface shear. Similar profiles are observed in Figure 25, where the boundary conditions match but the initial profile contains an additional tier $h_m = h_1$ in the interior of the domain. Once again, the $\mathrm{Re}^* = 0$ profile represents a travelling wave solution comparable to Figure 24a. When increasing the Reynolds number (Figure 25b), we obtain a smoothed reverse compressive profile that is evolving with time as in Figure 24b.



(a) $\mathrm{Re}^* = 0$ (b) $\mathrm{Re}^* = 10$

Figure 24.: Reverse compressive. $\theta = -45$, $h_l = h_2$, $h_r = h_3$.

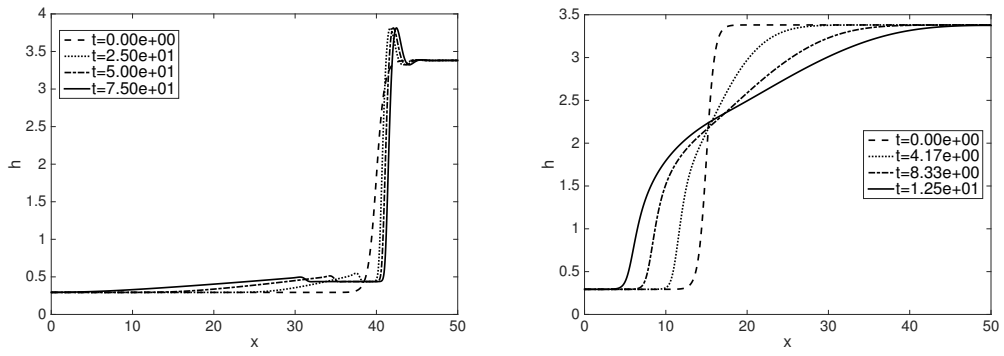


(a) $\mathrm{Re}^* = 0$ (b) $\mathrm{Re}^* = 10$

Figure 25.: Reverse compressive. $\theta = -45$, $h_l = h_2$, $h_m = h_1$, $h_r = h_3$.

Figure 26 illustrates the development of two-tier initial profiles with $h_l = h_1$ and $h_r = h_3$, while Figure 27 contains three-tier initial profiles with the

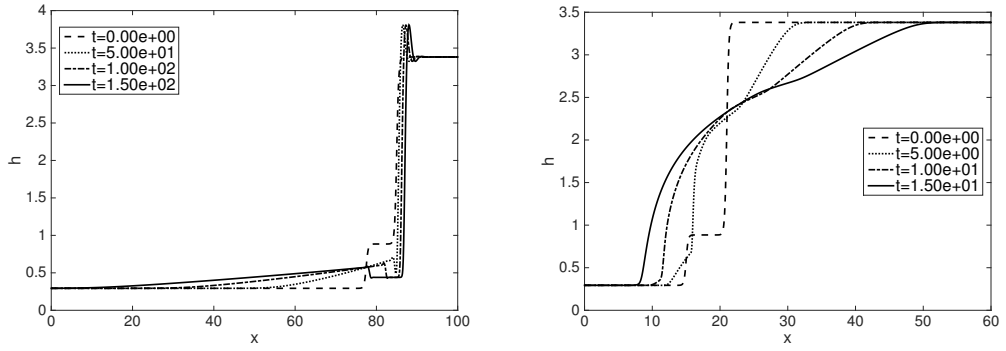
same boundary conditions and an interior tier at $h_m = h_2$. Again, similarity is observed between different profiles provided the boundary conditions are consistent, as illustrated with Figure 26 and 27, highlighting uniqueness of the solutions obtained. At $\mathrm{Re}^* = 0$, a central tier is observed developing at $h = 0.4374$, to the left of the main standing wave. This is not a solution of the cubic equation (2.1.7) which would be consistent with the flux at the inlet and outlet. The profiles in figures 26a and 27a are similar to a solution obtained by Levy and Shearer [28], who reported a large downward facing travelling wave followed by a smaller upward facing travelling wave. Although both waves are moving upwards, the speed of the larger wave is greater than that of the smaller one and the distance between them increases, leaving the interior film depth at $h = 0.4374$. Increasing the Reynolds number, in both the two-tier and three-tier initial profile cases, has the effect of eliminating this feature, as well as smoothing the solution. Both inertial profiles 26b and 27b are of the same structure and the presence of the tier at $h_m = h_2$ in the interior of the three-tier initial profile does not affect the structure formed as time increases, once again indicating uniqueness of the solutions.



(a) $\mathrm{Re}^* = 0$ (b) $\mathrm{Re}^* = 10$

Figure 26.: Undercompressive - reverse undercompressive. $\theta = -45$, $h_l = h_1$, $h_r = h_3$.

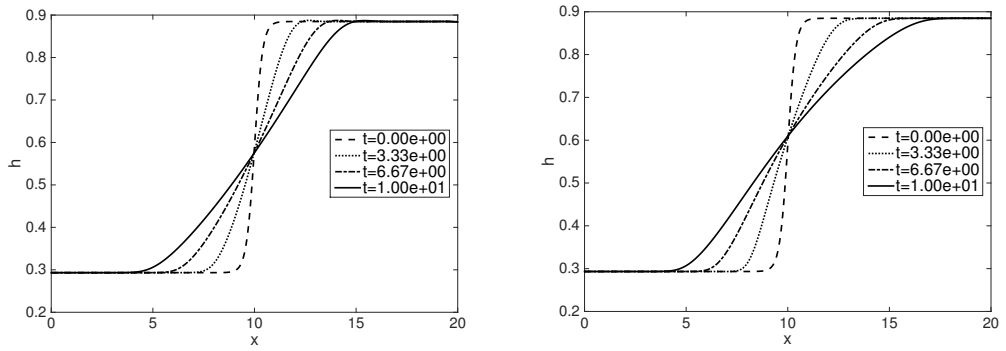
A typical rarefaction wave structure (Figure 28) was also observed, such as in figure 5b of [49], with boundary conditions $h_l = h_1$, $h_r = h_2$. In-



(a) $\mathrm{Re}^* = 0$ (b) $\mathrm{Re}^* = 10$

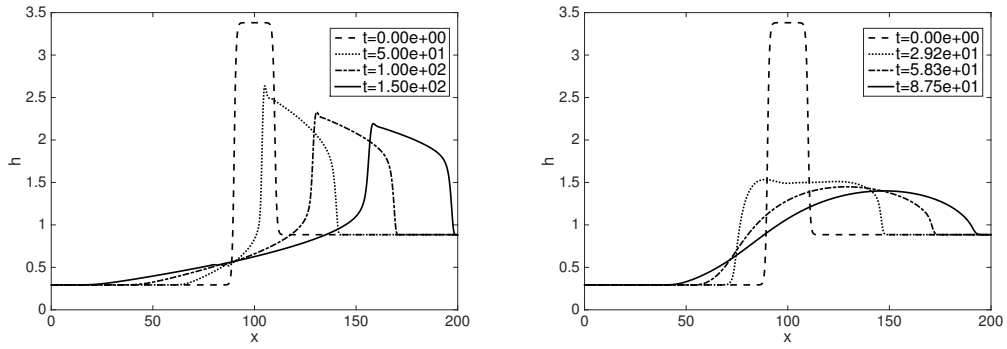
Figure 27.: Undercompressive - reverse undercompressive. $\theta = -45$, $h_l = h_1$, $h_m = h_2$, $h_r = h_3$.

creasing the Reynolds number had a minimal effect in this type of film profile, varying the speed of evolution, but with little change to the overall structure of the profile. When investigating the three-tier profile with boundary conditions equivalent to the rarefaction wave profile, a decaying undercompressive-rarefaction wave film profile is seen as in Figure 29. It is anticipated that this is a transient process tending towards the rarefaction wave over an extended period of time. The most significant difference between the non-inertial and inertial profiles in figures 29a and 29b is the smoothing of the wave structure, as is expected with increasing Reynolds number.



(a) $\mathrm{Re}^* = 0$ (b) $\mathrm{Re}^* = 10$

Figure 28.: Rarefaction wave. $\theta = -45$, $h_l = h_1$, $h_r = h_2$.



(a) $\mathrm{Re}^* = 0$ (b) $\mathrm{Re}^* = 10$

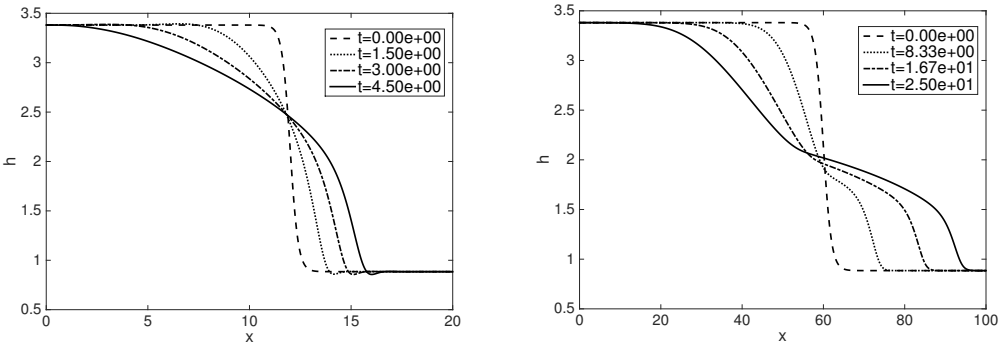
Figure 29.: Undercompressive - rarefaction wave. $\theta = -45$, $h_l = h_1$, $h_m = h_3$, $h_r = h_2$.

3.3.2 *Formation of new fronts*

A new feature observed with the inclusion of inertia is the formation of an evolving region that is not a conjugate height in Table 3. The heights of the fronts depend on the boundary conditions of the initial profiles. In order to verify that the effects observed are a physical feature, the initial conditions are modified to maintain the same boundary conditions, but with modified conditions in the interior of the domain.

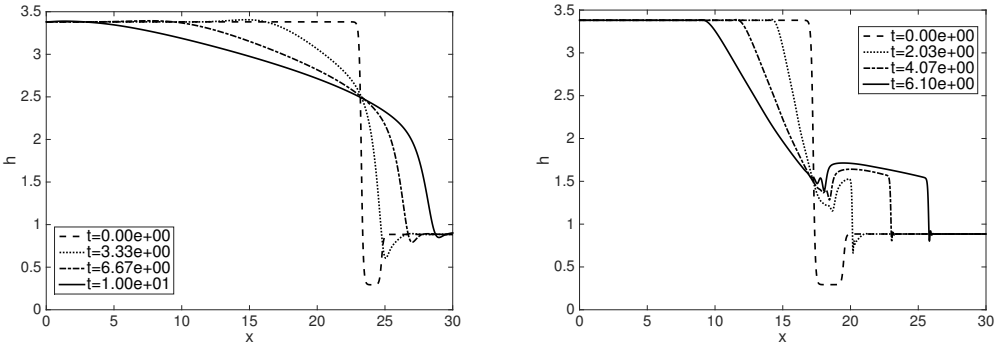
A profile initiated by $h_l = h_3$ (figures 30-33) produces an undercompressive front at $\mathrm{Re}^* = 0$, also reported by Levy and Shearer [28]. Commonality of solution is observed, exhibited by changes in initial profile with equivalent boundary conditions developing into identically shaped wave structures. This is evident in figures 30a and the equivalent three-tier initial profile solution 31a, where $h_m = h_1$, $h_r = h_2$, as well as with figures 32a and 33a, where $h_m = h_2$, $h_r = h_1$. When increasing the Reynolds number, the formation of a secondary undercompressive front is seen - this is a new feature not reported in any Stokes flow study. The height of the intermediate state depends on the boundary conditions, so different initial profiles with identical boundary conditions form intermediate fronts of the same height. In Figure 30b, the secondary front has an approximate film height of 1.5 -

higher than the intermediate film height $h_2 = 0.8848$ associated with a slope inclination of $\theta = -45$. As in the previous section, the features produced from two-tier initial profiles are able to be replicated by allowing three-tier initial profiles with the respective boundary conditions to develop, suggesting that these are unique solutions given the boundary conditions in figures 30 and 31. The film profiles in Figure 32a and 33a with boundary conditions $h_l = h_3$, $h_r = h_1$, both develop into identically structured undercompressive waves with both the two-tier and the three-tier initial profile configurations. With the inclusion of inertia, as can be seen in figures 32b and 33b, there is development of a secondary undercompressive front with an approximate film height of 1, marginally lower than the intermediate film height.



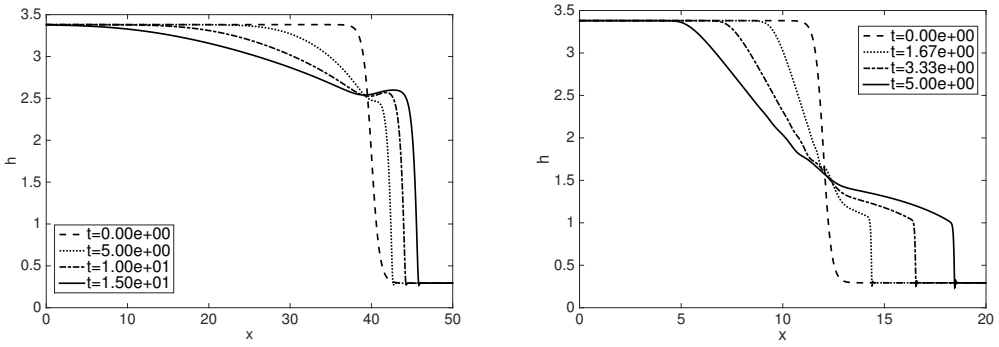
(a) $\mathrm{Re}^* = 0$ (b) $\mathrm{Re}^* = 10$

Figure 30.: (a) Undercompressive. (b) Undercompressive - undercompressive. $\theta = -45$, $h_l = h_3$, $h_r = h_2$.



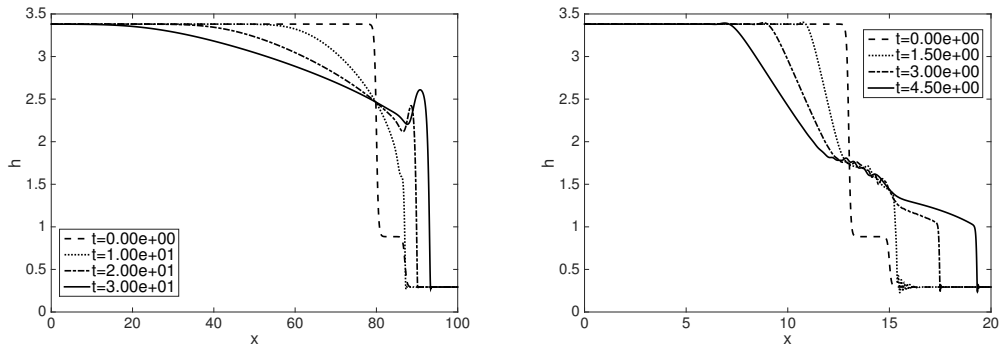
(a) $\mathrm{Re}^* = 0$ (b) $\mathrm{Re}^* = 10$

Figure 31.: (a) Undercompressive. (b) Undercompressive - undercompressive. $\theta = -45$, $h_l = h_3$, $h_m = h_1$, $h_r = h_2$.



(a) $\mathrm{Re}^* = 0$ (b) $\mathrm{Re}^* = 10$

Figure 32.: (a) Undercompressive. (b) Undercompressive - undercompressive. $\theta = -45$, $h_l = h_3$, $h_r = h_1$.



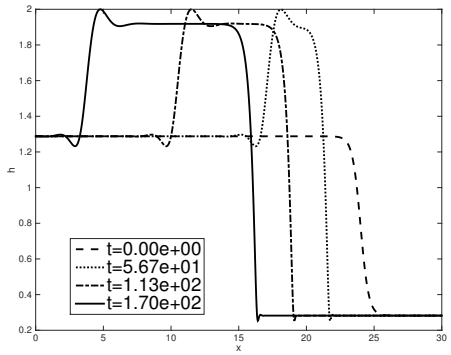
(a) $\mathrm{Re}^* = 0$ (b) $\mathrm{Re}^* = 10$

Figure 33.: (a) Undercompressive. (b) Undercompressive - undercompressive. $\theta = -45$, $h_l = h_3$, $h_m = h_2$, $h_r = h_1$.

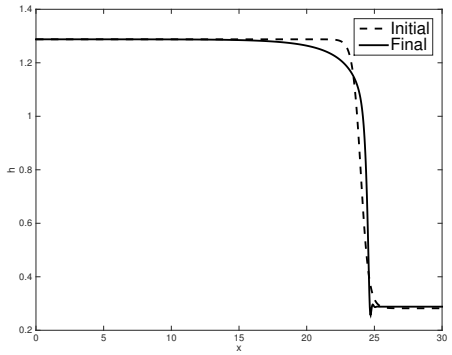
3.3.3 *Near-vertical film profiles*

The cases exhibited in figures 17 to 29 are representative of the types of film profile obtained at moderate angles of inclination. However, on increasing the slope inclination to $\theta = -80$, the evolution of some film profiles at $\mathrm{Re}^* = 0$ reveals a wave feature not evident at $\theta = -45$. At $0 \leq \mathrm{Re}^* \ll 1$, the formation of an interior tier at a height of 1.9 is observed as in several profiles, indicating uniqueness of the solution. When increasing the film Reynolds number, the profiles become identical in structure to cases at $\theta = -45$ with equivalent boundary conditions. This feature is observed in cases where $h_r = h_1$ irrespective of whether the initial profile is of a two-tier or three-tier configuration and is classified as a compressive-undercompressive structure. The compressive wave is moving, within the frame of reference shown, at a slower speed than the reference velocity and therefore physically represents a wave structure moving in the positive x-direction, up the plane i.e. to the left in the figure. The undercompressive wave is also moving up the plane, but at a faster rate, and so the tier at $h = 1.9$ will become increasingly dominant throughout the domain. The inclusion of a small film Reynolds number is enough to eliminate this feature, as in Figure 34b, and increasing the Reynolds number further (Figure 34c) illustrates the uniqueness of the solution in comparison to Figure 17b. The development of the three-tier initial profile in Figure 35a with equivalent boundary conditions to Figure 34 also produces the tier at $h = 1.9$ when $\mathrm{Re}^* = 0$. Figure 35b with $\mathrm{Re}^* = 10$ exhibits similarity to the $\theta = -45$ profile in Figure 23b.

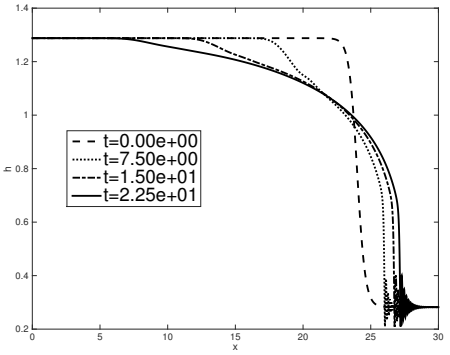
The development of the new feature is again observed with an initial profile configuration consisting of boundary conditions $h_l = h_3$ and $h_r = h_1$, as in figures 36 and 37. Figure 36 illustrates the time development of a two-tier initial profile into a three-tier profile at $\mathrm{Re}^* = 0$, which is then no longer present when the Reynolds number is increased to $\mathrm{Re}^* = 10$. The height of the newly-developed tier is $h = 1.9$, providing confirmation of the



(a) $\mathrm{Re}^* = 0$

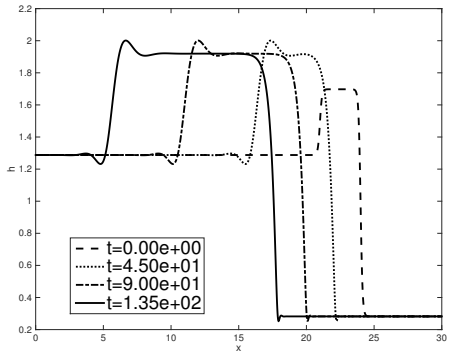


(b) $\mathrm{Re}^* = 1$

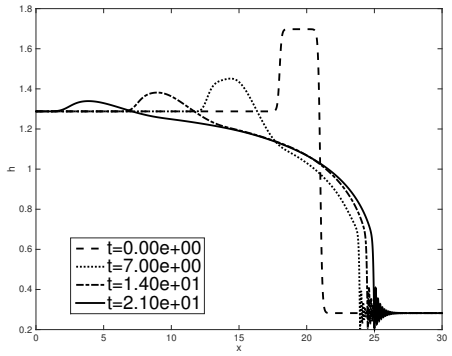


(c) $\mathrm{Re}^* = 10$

Figure 34.: $\theta = -80$, $h_l = h_2$, $h_r = h_1$.



(a) $\mathrm{Re}^* = 0$

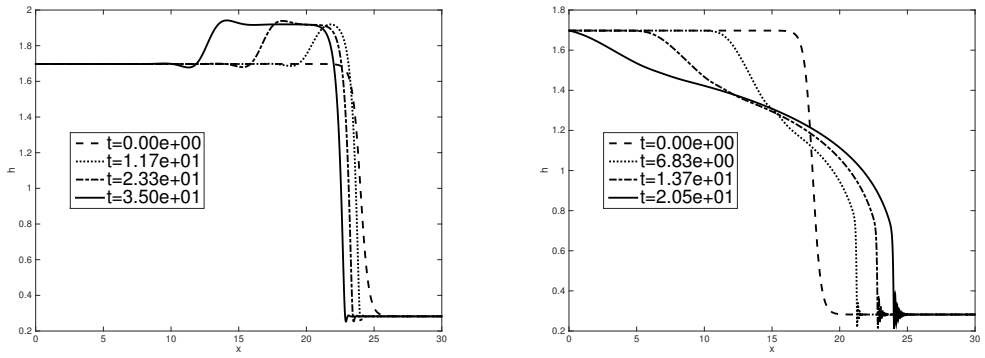


(b) $\mathrm{Re}^* = 10$

Figure 35.: $\theta = -80$, $h_l = h_2$, $h_m = h_3$, $h_r = h_1$

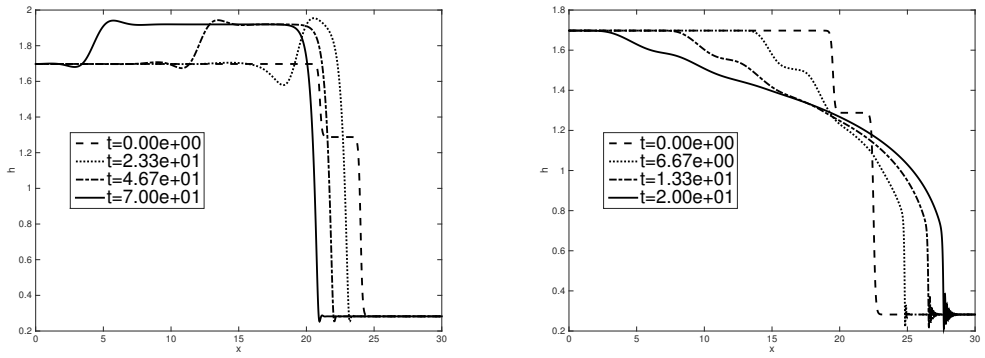
new tier observed in figures 34a and 35a. The tier at $h = 1.9$ is also seen in the development of a three-tier initial profile with boundary and initial

conditions $h_l = h_3$, $h_m = h_2$ and $h_r = h_1$, as in Figure 37a. The commonality with the profiles depicted in figures 34-37 is the height of the right hand side boundary, which is always the lowest of the three conjugate heights.



(a) $\mathrm{Re}^* = 0$ (b) $\mathrm{Re}^* = 10$

Figure 36.: $\theta = -80$, $h_l = h_3$, $h_r = h_1$.

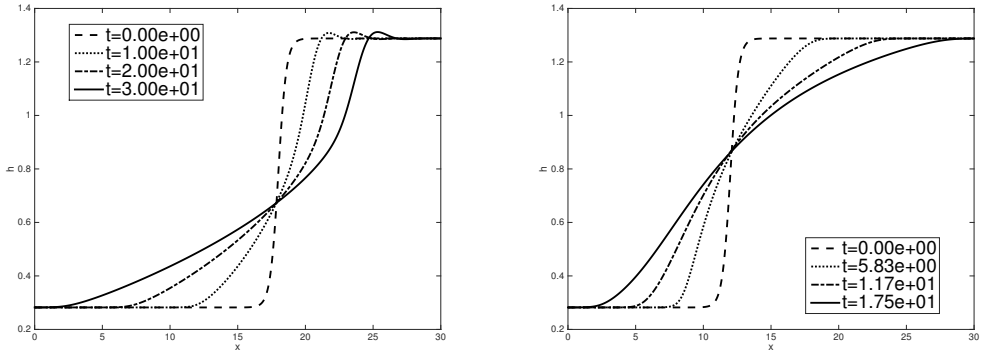


(a) $\mathrm{Re}^* = 0$ (b) $\mathrm{Re}^* = 10$

Figure 37.: $\theta = -80$, $h_l = h_3$, $h_m = h_2$, $h_r = h_1$.

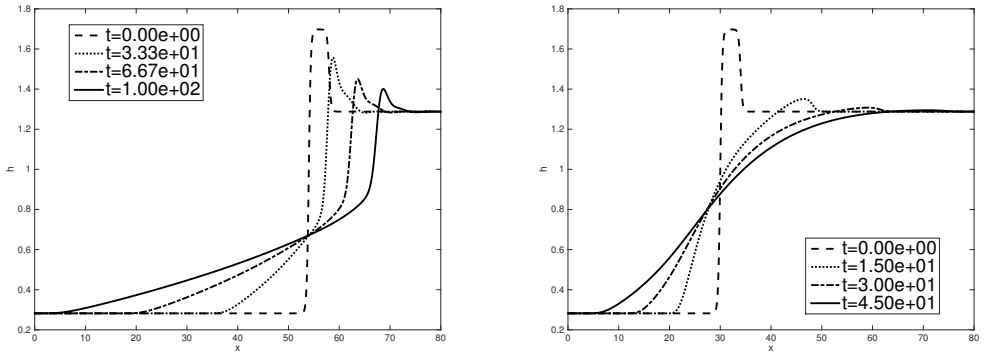
With an initial profile as in figures 38 and 39, with the lowest conjugate height on the left and the intermediate height on the right hand side boundary, profile development is observed very similar to that in figures 28 and29. Again, the general trend of the transient profile is determined by the boundary conditions as opposed to the initial conditions. A smoother profile is seen at $\theta = -45$ compared to $\theta = -80$, with sharper changes in film gradi-

ent, potentially due to the increased effect of gravity at steeper inclination angles.



(a) $\mathrm{Re}^* = 0$ (b) $\mathrm{Re}^* = 10$

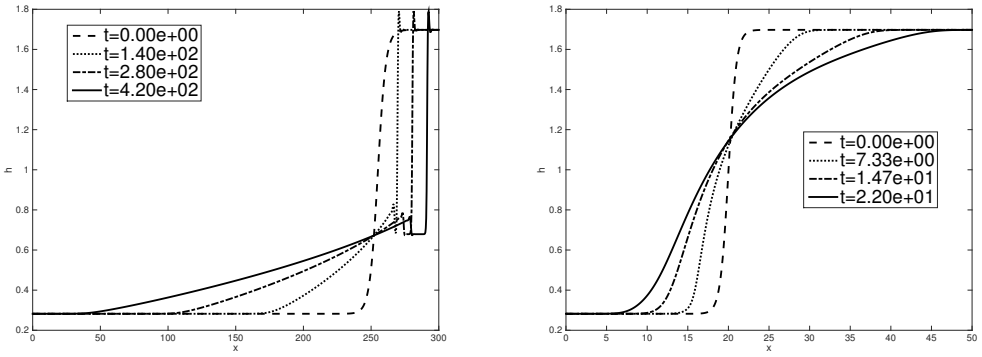
Figure 38.: $\theta = -80$, $h_l = h_1$, $h_r = h_2$.



(a) $\mathrm{Re}^* = 0$ (b) $\mathrm{Re}^* = 10$

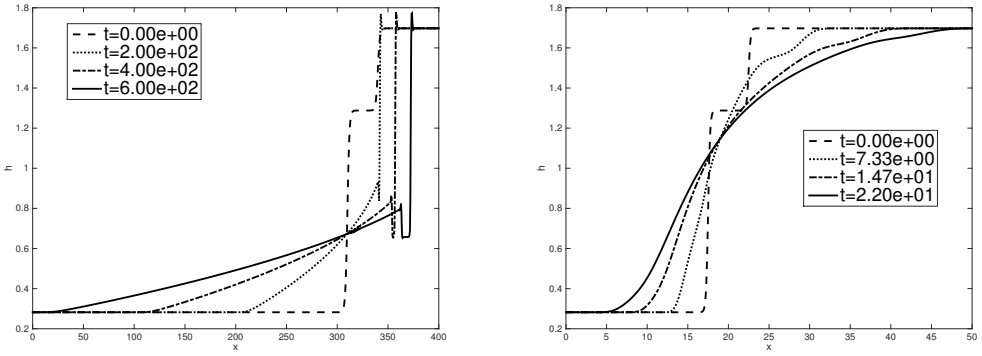
Figure 39.: $\theta = -80$, $h_l = h_1$, $h_m = h_3$, $h_r = h_2$.

Figures 40 and 41 compare with 26 and 27, with almost identical profile structures evolving at $\theta = -80$ as with the respective $\theta = -45$ cases. The formation of a tier at the base of the negative-facing front is observed, at a height of approximately $h = 0.7$. This value appears as the height of the tier formed with a three-tier initial profile, where the initial intermediate tier is eliminated with the evolution of the profile. Profiles for both the two-tier and three-tier initial cases develop into identical structures, as was seen in figures 26 and 27.



(a) $\mathrm{Re}^* = 0$ (b) $\mathrm{Re}^* = 10$

Figure 40.: $\theta = -80$, $h_l = h_1$, $h_r = h_3$.

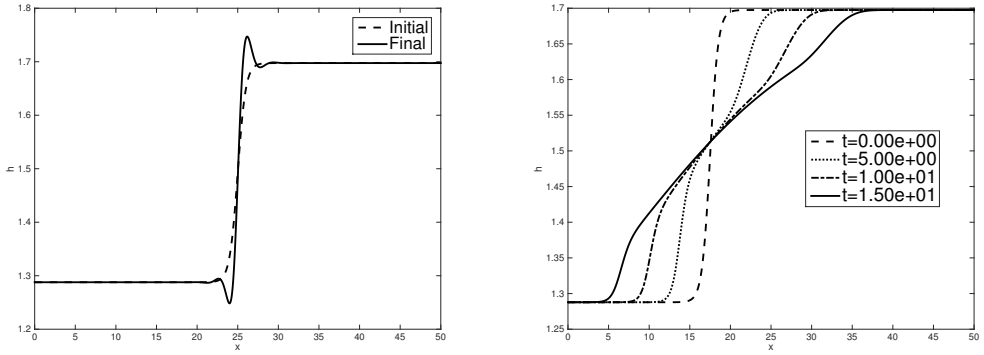


(a) $\mathrm{Re}^* = 0$ (b) $\mathrm{Re}^* = 10$

Figure 41.: $\theta = -80$, $h_l = h_1$, $h_m = h_2$, $h_r = h_3$.

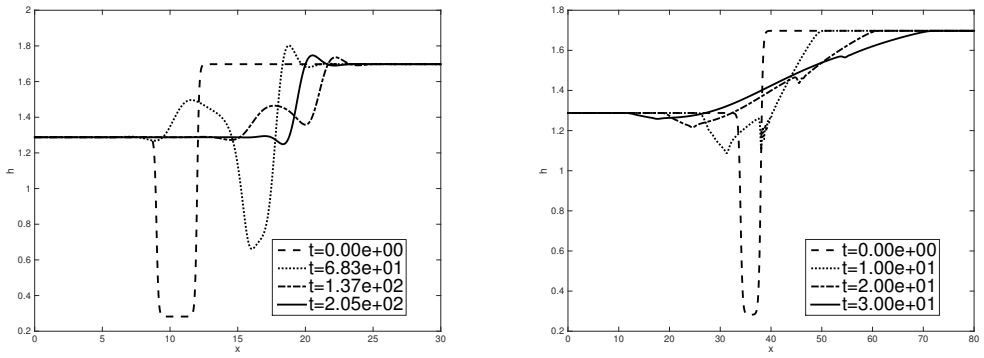
Initial profiles with boundary conditions $h_l = h_2$, $h_r = h_3$ are now considered, as in figures 42 and 43. Figure 42 compares with Figure 24, with the profiles at $\mathrm{Re}^* = 0$ obtaining a steady state solution in a moving frame of reference. Within a fixed frame of reference, this corresponds to an upward-facing travelling wave. The inclusion of inertia transforms both the two-tier and three-tier initial profiles into transient solutions comparable to those at $\theta = -45$. When comparing figures 24a and 42a, a point to note is the shift in the positive x-direction in the $\theta = -80$ case, where the steady profile is achieved further towards the right hand side of the domain. This is presumed to be an effect of the larger gravitational force acting at the steeper

angle of inclination. Wave development in Figure 43, from a three-tier initial profile, is in a similar manner as from the two-tier equivalent seen in Figure 42.



(a) $\mathrm{Re}^* = 0$ (b) $\mathrm{Re}^* = 10$

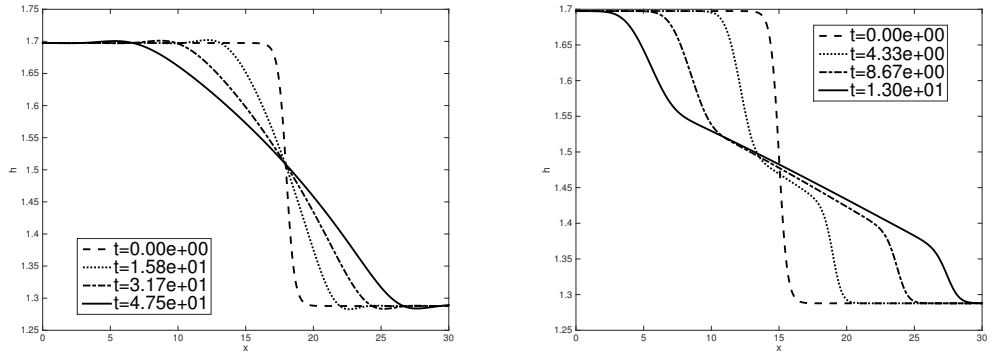
Figure 42.: $\theta = -80$, $h_l = h_2$, $h_r = h_3$.



(a) $\mathrm{Re}^* = 0$ (b) $\mathrm{Re}^* = 10$

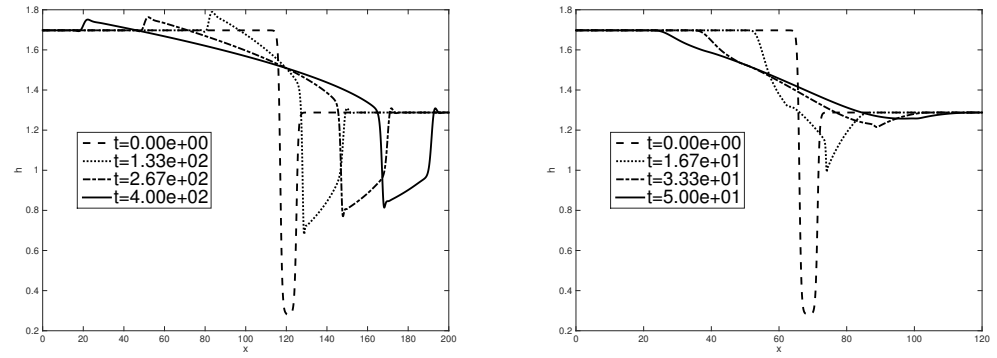
Figure 43.: $\theta = -80$, $h_l = h_2$, $h_m = h_1$, $h_r = h_3$.

Initial profiles with boundary conditions set at the conjugate heights of $h_l = h_3$ and $h_r = h_2$, as in figures 44 and 45 produce smoother fronts which evolve at a much slower rate than their $\theta = -45$ counterparts in figures 32 and 33.



(a) $\mathrm{Re}^* = 0$ (b) $\mathrm{Re}^* = 10$

Figure 44.: $\theta = -80$, $h_l = h_3$, $h_r = h_2$.



(a) $\mathrm{Re}^* = 0$ (b) $\mathrm{Re}^* = 10$

Figure 45.: $\theta = -80$, $h_l = h_3$, $h_m = h_1$, $h_r = h_2$.

3.4 FILM EVOLUTION EQUATIONS USING A CUBIC VELOCITY PROFILE

Recirculation regions within both shear-driven flow and gravity-driven flow are intrinsic in capturing the profile of surface waves. Recirculation may be captured by a quadratic velocity profile such as assumed in Chapters 3 and 4, but for greater detail and insight into how the fluid behaves within the thin film, an additional order of accuracy may be required. In this section, the governing equations for the flow are revised assuming a cubic velocity profile for the flow. The velocity profile is taken to assume the cubic form

$$u = a_0 + a_1 y + a_2 y^2 + a_3 y^3. \tag{3.4.1}$$

As previously the no-slip and no-penetration boundary conditions

$$u = -1 \quad \text{and} \quad v = 0 \tag{3.4.2}$$

are applied on the fluid-plane boundary at $y = 0$. The film flux is defined as

$$q = \int_0^h u \, \mathrm{d}y. \tag{3.4.3}$$

Taking the x and y momentum equations from (2.0.11)-(2.0.12) at leading order gives the coupled partial differential equations

$$\begin{aligned} \mathrm{Re}^* \left(\frac{\partial u}{\partial t} + u\frac{\partial u}{\partial x} + v\frac{\partial u}{\partial y} \right) &= -\frac{\partial p}{\partial x} + \frac{\partial^2 u}{\partial y^2} + \lambda \sin\theta, \\ \frac{\partial p}{\partial y} &= 0. \end{aligned} \tag{3.4.4}$$

Integrating the second equation in (3.4.4) gives

$$p = p_a, \tag{3.4.5}$$

by enforcing the pressure $p = p_a$ on $y = h$ at leading order. Enforcing the no-slip and no penetration conditions (3.4.2), then

$$0 = \frac{\partial^2 u}{\partial y^2} + \lambda \sin\theta. \tag{3.4.6}$$

Additional constraints required to define a_0, a_1, a_2 and a_3 are

$$\begin{aligned} &a_1 + 2a_2 h = \tau, \\ &a_0 = -1, \\ &a_0 h + a_1 \frac{h^2}{2} + a_2 \frac{h^3}{3} + a_3 \frac{h^4}{4} = q, \end{aligned} \tag{3.4.7}$$

similar to Section 3.1. Solving (3.4.6)-(3.4.7) yields cubic film profile coefficients

$$\begin{aligned} a_0 &= -1, \\ a_1 &= \frac{\lambda h^3 \sin\theta - h^2\tau + 12h + 12q}{5h^2}, \\ a_2 &= -\frac{1}{2}\lambda \sin\theta, \\ a_3 &= \frac{4\lambda h^3 \sin\theta + 6h^2\tau - 12h - 12q}{15h^4}. \end{aligned} \tag{3.4.8}$$

As previously, the chain rule is applied to express the integral velocity terms I_h and I_q as in (2.3.11). This yields the nonlinear integral coefficients

$$I_h = \frac{1}{2625h^2}\Big(5\lambda^2 h^6 \sin\theta^2 - 23h^5\lambda\tau\sin\theta - 123h^4\lambda\sin\theta \\ -82h^3\lambda q\sin\theta + 33h^4\tau^2 + 192h^3\tau + 96h^2 q\tau + 639h^2 - 3264q^2\Big) \quad (3.4.9)$$

and

$$I_q = -\frac{1}{2625h}\Big(41\lambda h^3\sin\theta - 96h^2\tau - 1278h - 6528q\Big). \quad (3.4.10)$$

The revised momentum equation is

$$\mathrm{Re}^*\left(\frac{\partial q}{\partial t} + I_h\frac{\partial h}{\partial x} + I_q\frac{\partial q}{\partial x}\right) = \lambda h\sin\theta + \tau \\ - \frac{\lambda h^3\sin\theta - h^2\tau + 12h + 12q}{5h^2} - \varepsilon\lambda h\frac{\partial h}{\partial x}\cos\theta + \frac{\varepsilon^3}{\mathrm{Ca}}h\frac{\partial^3 h}{\partial x^3}. \quad (3.4.11)$$

As previously, the same continuity equation as

$$\frac{\partial h}{\partial t} + \frac{\partial q}{\partial x} = 0. \quad (3.4.12)$$

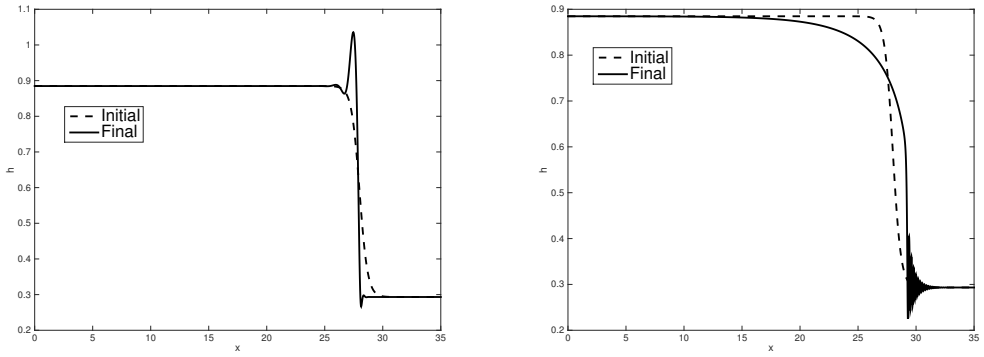
3.4.1 *Shear-driven film profiles using a cubic velocity profile*

Following the approach of Section 3.3, thin-film flow on an inclined plane subject to surface shear opposing gravity is again considered. Parameter values have been chosen to be identical to earlier in the chapter to enable direct comparison of profiles.

Particular importance is given to the capillary region so that an assessment of the recirculation properties within the fluid layer may be made. Initial profiles are again chosen such that they reflect the Nusselt solutions of the cubic equation arising from steady, uniform flow

$$q = \frac{\lambda h^3}{3}\sin\theta + \frac{\tau}{2}h^2 - h, \quad (3.4.13)$$

with solution values of h given in Table 3. As earlier, h_1, h_2 and h_3 correspond to the low, intermediate and highest conjugate states, whilst h_l, h_m

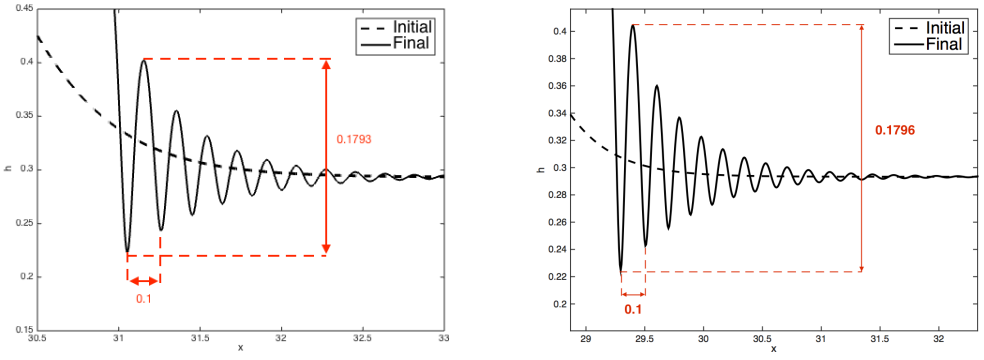


(a) $\mathrm{Re}^* = 0$ (b) $\mathrm{Re}^* = 10$

Figure 46.: Wave profiles. $\theta = -45$, $h_l = h_2$, $h_r = h_1$.

and h_r refer to the height of the tier on the left, in the middle, and on the right of the initial profile respectively.

Figure 46 shows wave profiles with boundary conditions $h_l = h_2$, $h_r = h_1$ that may be compared to those in Figure 17 obtained with a quadratic velocity profile. Structures of the standing wave are comparable, and so an expanded view of capillary region is analysed in order to gain more insight. Figure 47 shows the wavelength of the capillary ripples and these are not affected by choice of quadratic and cubic; amplitude is increased minimally with the cubic assumption.



(a) Quadratic (Figure 17b) (b) Cubic (Figure 46b)

Figure 47.: Expanded views of the capillary region obtained with quadratic and cubic velocity profiles at $\mathrm{Re}^* = 10$.

An analysis of velocity field and streamlines are calculated in a similar manner to Section 3.3, Equations (3.3.2)-(3.3.5). The fluid velocity parallel to the plane is given by

$$u = a_0 + a_1 y + a_2 y^2 + a_3 y^3, \tag{3.4.14}$$

whilst the velocity vector perpendicular to the plane is calculated by

$$v = \int - \left(\frac{\partial a_0}{\partial x} + \frac{\partial a_1}{\partial x} y + \frac{\partial a_2}{\partial x} y^2 + \frac{\partial a_3}{\partial x} y^3 \right) \mathrm{d}y \tag{3.4.15}$$

and a no-penetration boundary condition $v = 0$ at $y = 0$ used to give

$$v = - \left(\frac{\partial a_0}{\partial x} y + \frac{\partial a_1}{\partial x} \frac{y^2}{2} + \frac{\partial a_2}{\partial x} \frac{y^3}{3} + \frac{\partial a_3}{\partial x} \frac{y^4}{4} \right). \tag{3.4.16}$$

The flow velocity vectors can also be used directly to map the velocity profile at various points within the flow using the cubic profile (3.4.14) and the definitions of the coefficients in (3.4.8). Figures 48 and 49 depict the reconstructed cubic velocity profiles at various cross-sections on the main structure within the wave front as well as within the first capillary wave. It is noted that in both sets of velocity profiles, the majority of the velocity profiles are almost linear, with velocity profiles corresponding to the points marked indicating the more extreme examples shown.

The asterisks marked (i), in figures 48 and 49 respectively, show a much more nonlinear profile, although recirculation is not evident in either figure - for recirculation to be present, regions of the velocity profile more negative than $u = -1$ would be required; and showing velocities $u > -1$ at other heights.

Streamlines are calculated to give further insight. Figure 50 is compared to Figure 21 and it is observed that the cubic profile also reproduces flow dynamics as a moving bore on top of a base parallel flow, with disturbances to the parallel flow again observed within the capillary region.

For further investigation into the potential recirculation of fluid within the capillary region, the reduced Reynolds number is increased to $\mathrm{Re}^* = 20$ and the velocity profiles constructed at various points between the leading

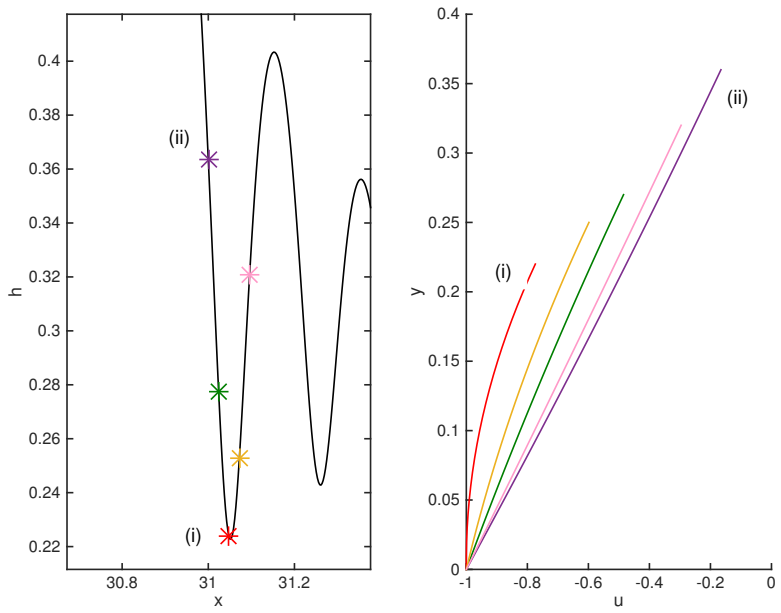


Figure 48.: Quadratic velocity profile at several cross-sections in Figure 46b. $\theta = -45$, $\mathrm{Re}^* = 10$.

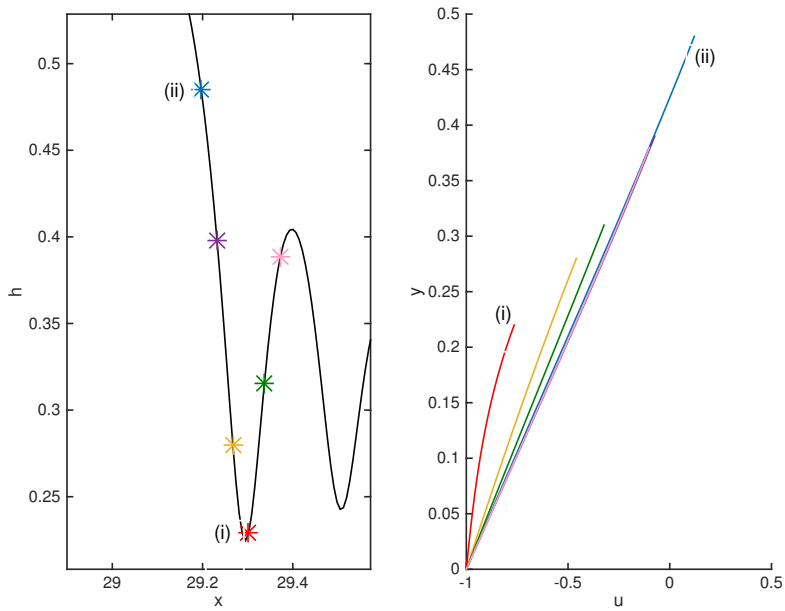


Figure 49.: Cubic velocity profile for indicated points reproduced from Figure 17b.

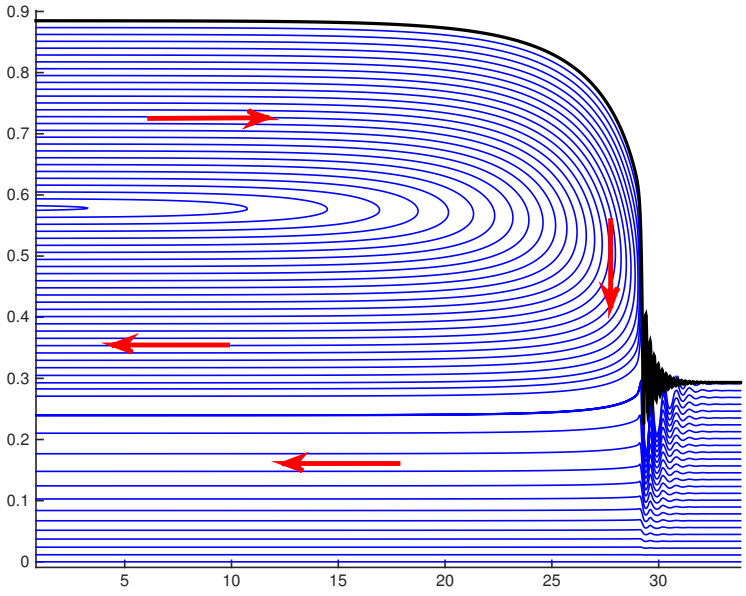


Figure 50.: Streamlines using cubic velocity profile in moving frame of reference. $\theta = -45$, $\mathrm{Re}^* = 10$, $h_l = 0.8848$, $h_r = 0.2933$.

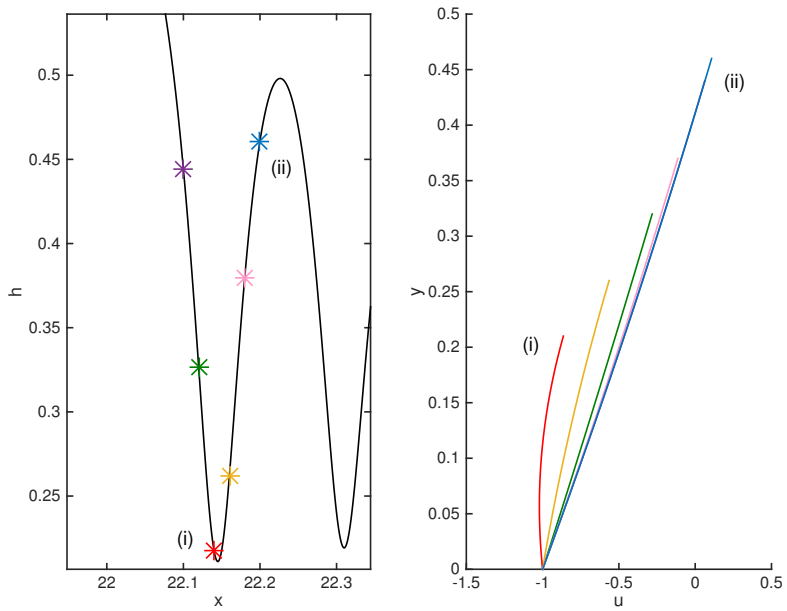


Figure 51.: Quadratic velocity profile at several cross-sections. $\theta = -45$, $\mathrm{Re}^* = 20$.

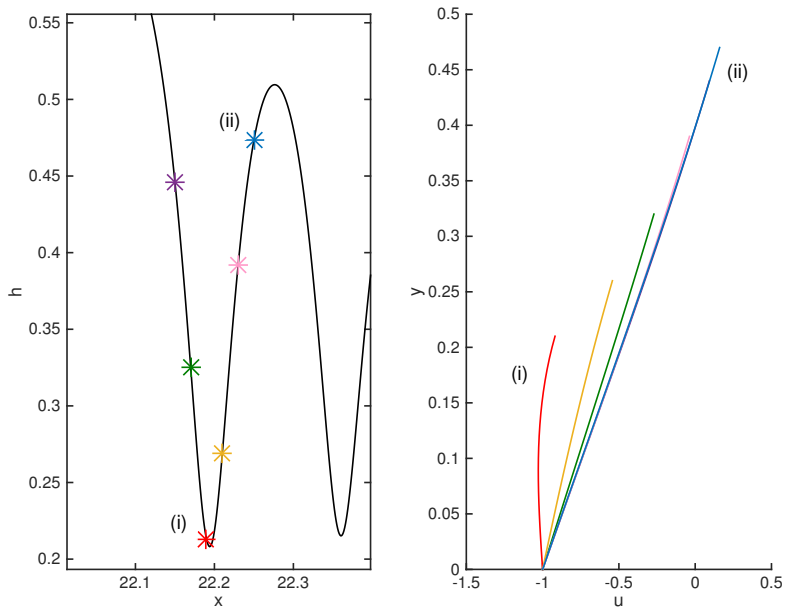


Figure 52.: Cubic velocity profile at several cross-sections. $\theta = -45$, $\mathrm{Re}^* = 20$.

wave and the first capillary wave. In Figure 52 it is seen that at the asterisk marked (i), which corresponds to the base of the first capillary ripple and the shallowest point in the wave profile, recirculation starts to become evident, with the velocity curve showing values more negative than the wall velocity. Within the moving frame of reference, this corresponds to fluid moving in the negative direction relative to the wall, and within a fixed frame of reference, this implies recirculation. Velocity profiles at the other points sampled tend to be closer to linear in structure. The quadratic profiles depicted in Figure 51 show no significant differences to the cubic profiles in Figure 52, with recirculation at the shallowest point in the film profile observed.

Reverting back to a Reynolds number of $\mathrm{Re}^* = 10$, the angle of inclination is increased to $\theta = -80$ to observe the recirculation properties within a near-vertical film. Figures 53 and 54 show quadratic and cubic velocity profiles respectively at various points within the main wave structure and capillary region. Both figures exhibit similar profile shapes, with a velocity

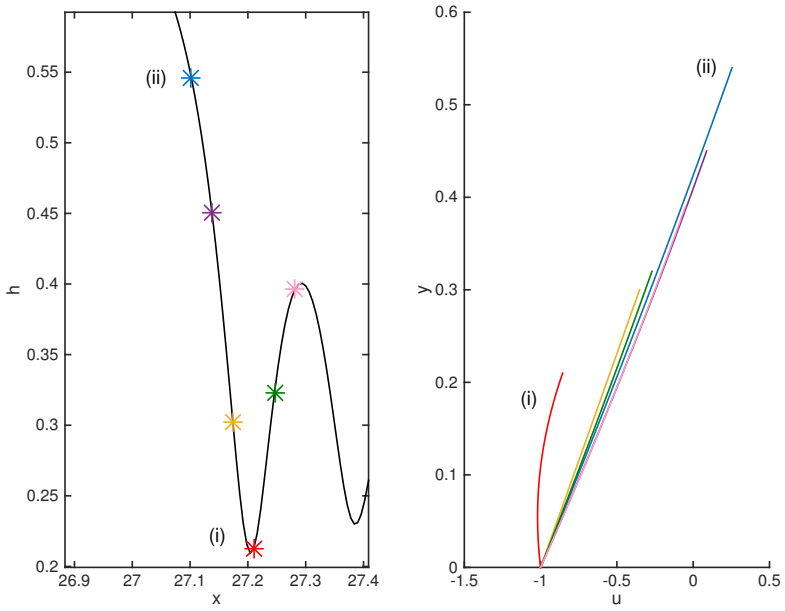


Figure 53.: Quadratic velocity profile at several cross-sections. $\theta = -80$, $\mathrm{Re}^* = 10$.

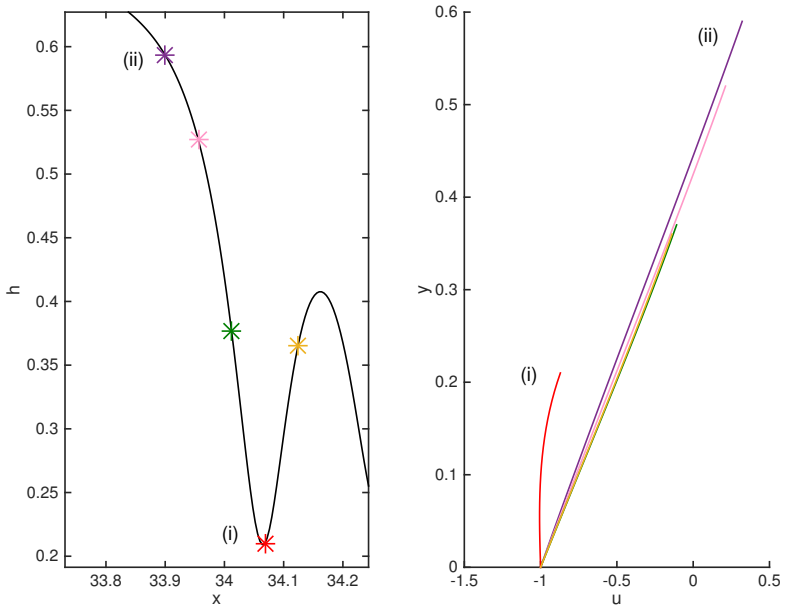
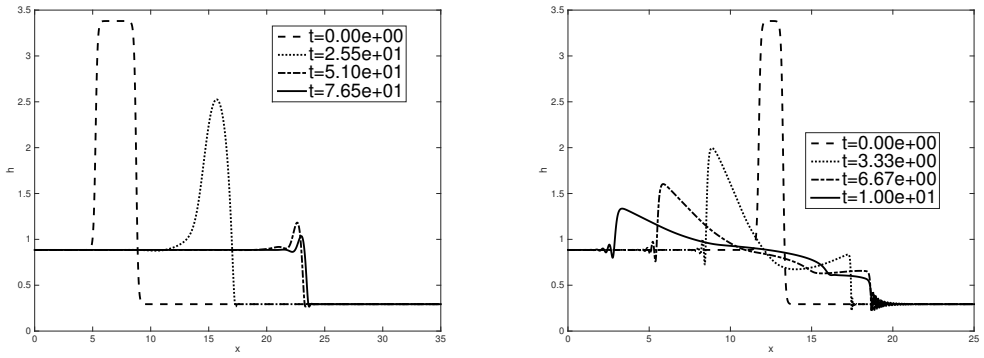


Figure 54.: Cubic velocity profile at several cross-sections. $\theta = -80$, $\mathrm{Re}^* = 10$.

marginally more negative than $u = -1$ observed at a cross section taken in line with the shallowest point on the film profile, reflecting a very slight recirculation region. This corresponds to the profiles marked (i) in figures 53 and 54. From comparisons between figures 52-54, it is observed that there is very strong similarity in assuming quadratic and cubic velocity profiles within the flow.

The other profiles obtained using an assumed cubic velocity profile are now compared, both between $\mathrm{Re}^* = 0$ and $\mathrm{Re}^* = 10$ cases, as well as to the profiles within Section 3.3 with equivalent boundary and initial conditions but obtained using a quadratic velocity profile.

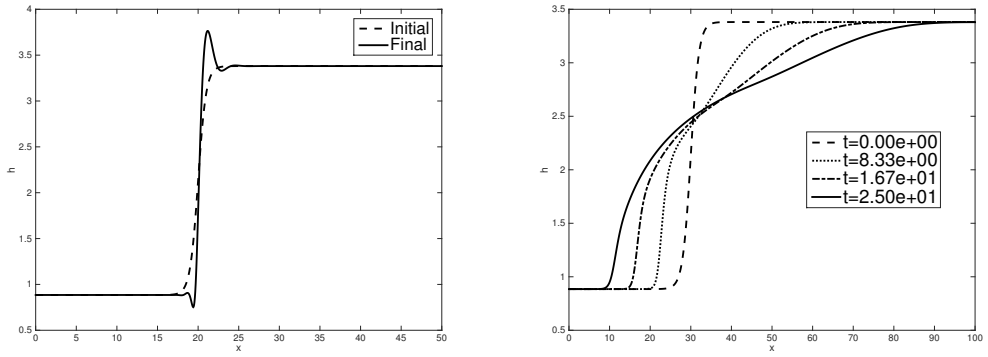
As when comparing the profiles obtained in this section, when assuming a cubic velocity profile, to those obtained in Section 3.3 through the assumption of a quadratic velocity profile, several of the profiles exhibited strong similarities and identical structures with subtle differences. The boundary conditions of the three-tier initial profiles in Figure 55 correspond to those of the two-tier initial profiles in Figure 46, as well as those from 23. It is shown that the initial profiles in Figure 55 are tending towards the same structures which evolved in the two-tier initial profile equivalent.



(a) $\mathrm{Re}^* = 0$ (b) $\mathrm{Re}^* = 10$

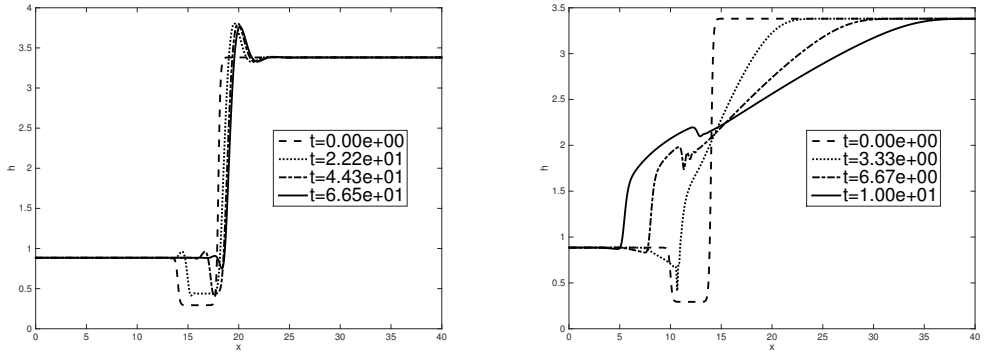
Figure 55.: Wave profiles. $\theta = -45$, $h_l = h_2$, $h_m = h_3$, $h_r = h_1$.

Figures 56 and 57 are the respective two and three-tier initial profiles with boundary conditions $h_l = h_2$ and $h_r = h_3$. Identical profile development is



(a) $\mathrm{Re}^* = 0$ (b) $\mathrm{Re}^* = 10$

Figure 56.: Wave profiles. $\theta = -45$, $h_l = h_2$, $h_r = h_3$.

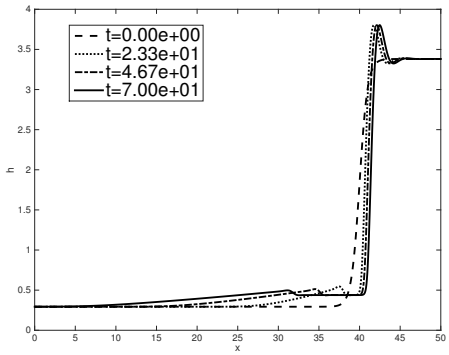


(a) $\mathrm{Re}^* = 0$ (b) $\mathrm{Re}^* = 10$

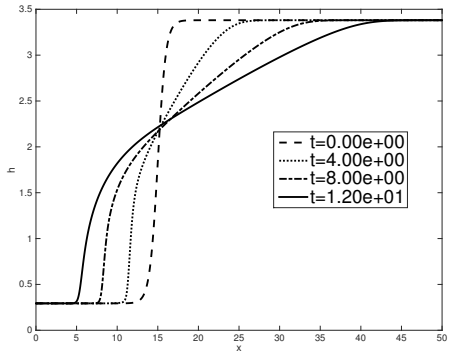
Figure 57.: Wave profiles. $\theta = -45$, $h_l = h_2$, $h_m = h_1$, $h_r = h_3$.

seen again when compared to figures 24 and 25. At $\mathrm{Re}^* = 0$, the formation of a standing wave is observed, travelling up the plane in a fixed coordinate system. With the reduced film Reynolds number increased to $\mathrm{Re}^* = 10$, smoothed transient profiles are observed.

Profiles with $h_l = h_1$ and $h_r = h_3$ are interesting in that the formation of a tier of height $h = 0.4$ is observed when $\mathrm{Re}^* = 0$. Seen in both figures 58a and 59a, this is consistent with tier development when adopting a quadratic velocity profile as in figures 26a and 27a, highlighting this as a model feature. The inclusion of inertia damps this tier and the smoothed profile observed in figures 58b and 59b is seen again.

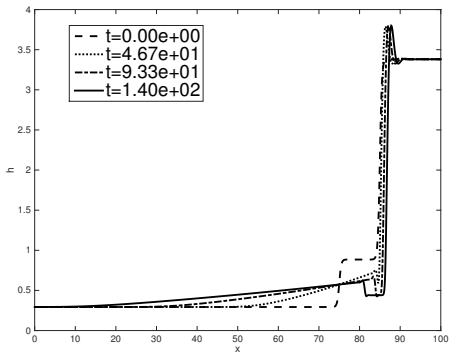


(a) $\mathrm{Re}^* = 0$

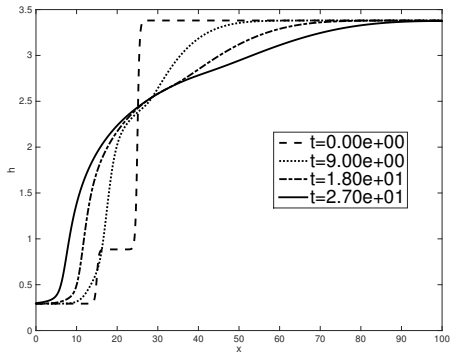


(b) $\mathrm{Re}^* = 10$

Figure 58.: Wave profiles. $\theta = -45$, $h_l = h_1$, $h_r = h_3$.

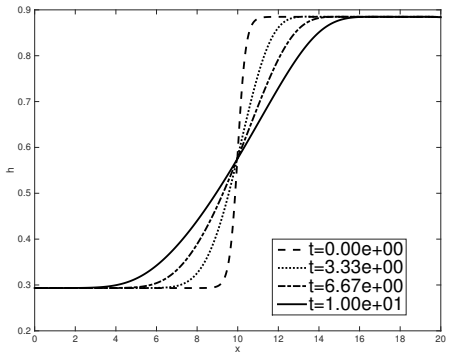


(a) $\mathrm{Re}^* = 0$

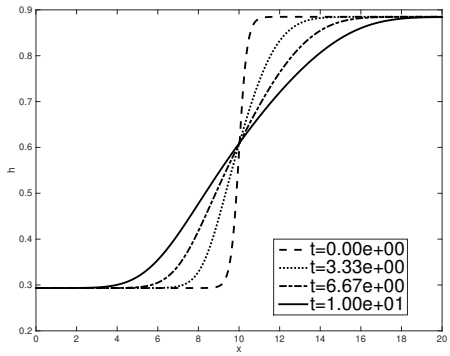


(b) $\mathrm{Re}^* = 10$

Figure 59.: Wave profiles. $\theta = -45$, $h_l = h_1$, $h_m = h_2$, $h_r = h_3$.

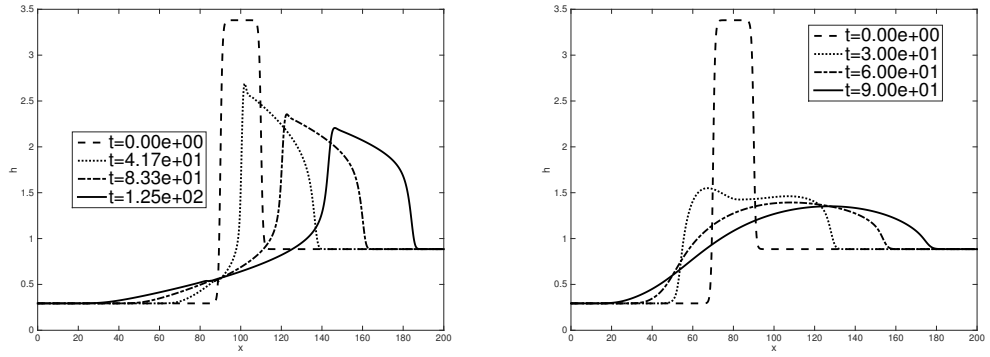


(a) $\mathrm{Re}^* = 0$



(b) $\mathrm{Re}^* = 10$

Figure 60.: Wave profiles. $\theta = -45$, $h_l = h_1$, $h_r = h_2$.

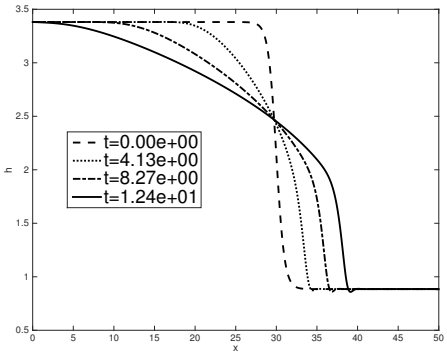


(a) $\mathrm{Re}^* = 0$ (b) $\mathrm{Re}^* = 10$

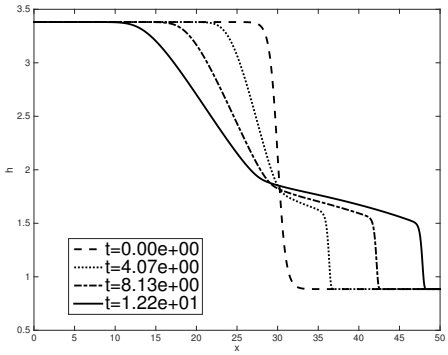
Figure 61.: Wave profiles. $\theta = -45$, $h_l = h_1$, $h_m = h_3$, $h_r = h_2$.

Boundary conditions of $h_l = h_1$, $h_r = h_2$ in figures 60 and 61 produce rarefaction wave type profiles as seen with a quadratic velocity profile previously. With a two-tier initial profile, increasing the film Reynolds number has minimal effect, whereas a three-tier initial profile, also observed in Figure 29b with a quadratic velocity profile, exhibits significant smoothing at $\mathrm{Re}^* = 0$.

The formation of fronts at heights which are not solutions of the cubic equation for constant flux is again observed using a cubic velocity profile in figures 62-65 as was with the quadratic velocity profile in figures 30-33. The profile development looks identical to those seen in Section 3.3, again dependent on boundary conditions. The boundary condition $h_l = h_3$ is common across all the profiles, and the height of the new front is dependent on the height of the right hand boundary. With the right hand boundary fixed at the intermediate conjugate height h_2, a new front at an approximate height of 1 is observed and when $h_r = h_1$, a similarly shaped profile is seen, but with the new front now taking a height $h \approx 1.5$. These values correspond to those observed previously, and are irrespective of whether the initial profile is of a two-tier or three-tier configuration.

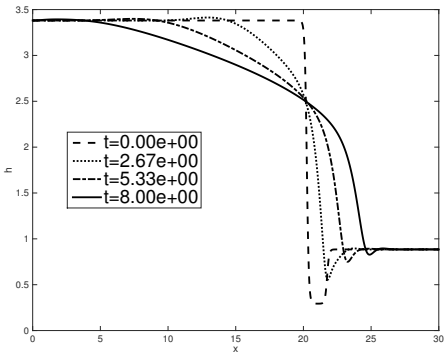


(a) $\mathrm{Re}^* = 0$

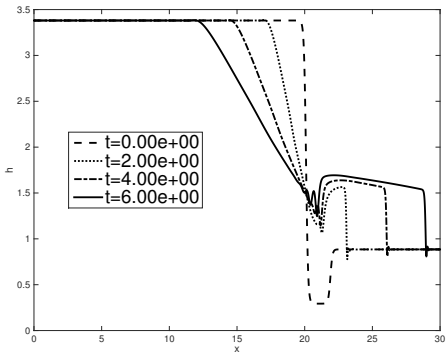


(b) $\mathrm{Re}^* = 10$

Figure 62.: Wave profiles. $\theta = -45$, $h_l = h_3$, $h_r = h_2$.

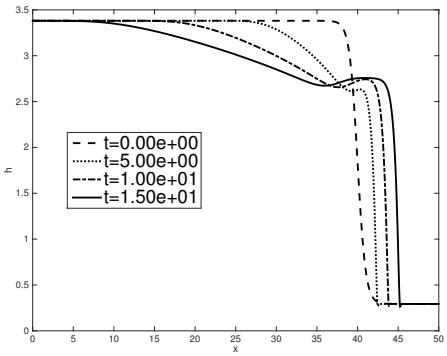


(a) $\mathrm{Re}^* = 0$

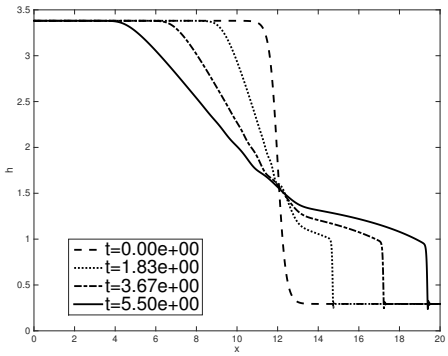


(b) $\mathrm{Re}^* = 10$

Figure 63.: Wave profiles. $\theta = -45$, $h_l = h_3$, $h_m = h_1$, $h_r = h_2$.

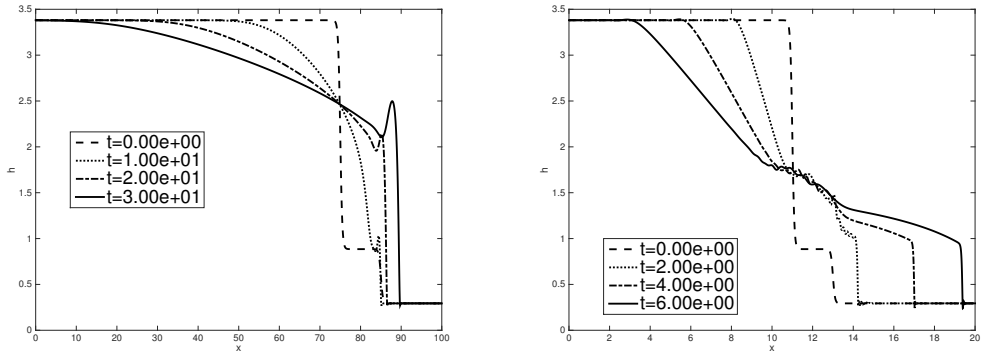


(a) $\mathrm{Re}^* = 0$



(b) $\mathrm{Re}^* = 10$

Figure 64.: Wave profiles. $\theta = -45$, $h_l = h_3$, $h_r = h_1$.



(a) $\mathrm{Re}^* = 0$ (b) $\mathrm{Re}^* = 10$

Figure 65.: Wave profiles. $\theta = -45$, $h_l = h_3$, $h_m = h_2$, $h_r = h_1$.

3.5 OVERVIEW OF THE CHAPTER

For modelling shear-driven Stokes flow, profiles obtained in previous literature were reproduced. The Reynolds number was then increased to allow the initial profiles such as those illustrated in figures 14 and 15 to develop under the influence of inertia. For some initial profiles the inclusion of inertia had a marginal impact on the film profile. Smoothing at the top of wave structures was observed due to the internal flow exhibiting a smoother pattern when $\mathrm{Re}^* > 0$. In other cases however, a significant change developed from the non-inertial profile. When comparing figures 31a and 31b, for example, both evolved from the same conjugate states selected from Table 3. Developed profiles involved either modification and smoothing as the Reynolds number was increased, or the formation of fronts at intermediate (non-conjugate) heights, indicating that these were solutions of the full model equations which include inertial effects, rather than Stokes flow solutions. These heights were consistent throughout, with three-tier initial profiles producing similar wave structures to their two-tier counterparts when equivalent boundary conditions were applied.

Additionally, wave profiles present only at steeper angles of slope inclination were produced and it was demonstrated that changing the Reynolds

number has a significant effect. Figures 34-37 illustrate, for an inclination angle of $\theta = -80$, the formation of a tier that is damped and then eliminated with the inclusion of a small film Reynolds number to the point where it is identical in structure to profiles obtained at $\theta = -45$. Formation of this tier is at a consistent height of approximately $h = 1.9$, irrespective of initial profile structure, the only commonality being that the height of the right hand boundary is the lowest of the three conjugate states possible at $\theta = -80$. This highlights that this is a Stokes flow model feature, which is then eliminated upon including inertial terms within the governing equations.

Within the latter part of this chapter, the mathematical formulation of the thin-film depth-averaged model has been revised to adopt a more general cubic velocity profile. With the extended model, the fluid dynamics within the capillary region of a wave structure were captured. Although the overall amplitude, wavelength and general structure of the capillary ripples remained similar to those observed previously, it was shown by reconstructing the profiles themselves that fluid deviates from a characteristic shear linear profile at the base of the main wave structure, the shallowest point within the flow profile. Increasing the film Reynolds number increases the curvature of the velocity profile at this point and recirculation of the fluid was observed, as seen in figures 51 and 52. Recirculation regions, where the fluid velocity, at points, is more negative than the wall velocity, are also observed at the near vertical angle of $\theta = -80$. Once again, both reconstructed quadratic and cubic velocity profiles show great similarity.

The remainder of the film profiles obtained when assuming a cubic velocity profile, in figures 55-65 were analysed for their overall structure, with all exhibiting the same features as their quadratic velocity profile counterparts from Section 3.3. Both two-tier and three-tier configurations were used, as previously, to initialise wave disturbances and the evolution of the structure was examined. A combination of compressive, undercompressive and rarefaction wave structures, as well as their downstream-facing equivalents were observed.

Thus, adoption of a cubic velocity profile was shown not to modify the wave structure as a whole, but instead potentially provide greater detail of flow dynamics within the capillary region. Further comparison of quadratic and cubic assumptions for the velocity profile is given in Chapter 5.

4

SHEAR-DRIVEN FLOW WITH A NAVIER SLIP BOUNDARY CONDITION

In this chapter the effects of setting a boundary condition which allows slip between the fluid and the wall at $y = 0$ are investigated, corresponding to a dimensionless slip length $\alpha > 0$. Mathematically this is reflected in the values of the coefficients on assuming a quadratic form $u = a_0 + a_1 y + a_2 y^2$ for the streamwise velocity profile. A Navier-slip boundary is physically interpreted by Samanta et al. [44] as a means of modelling flow over a porous medium, although their investigation is in the context of falling films and the formation of solitary waves. Pascal [37] shows that the Navier-slip boundary condition is a consistent means of modelling flow over a porous medium. An assumption is that flow within the porous medium has a much lower velocity than that within the main fluid layer itself; the effective slip length α is considered as related to the permeability of the substrate. Some studies [22, 30] choose to incorporate the Darcy number, a measure of the relative permeability of the medium versus its cross-sectional area, into their mathematical model, as a measure of the plane properties, as opposed to the slip length as is done here. Both these studies are restricted to focus on a linear stability analysis of the system rather than detail about the wave structures formed on the inclined plane. Bailey et al. [3] also incorporate a slip boundary condition on the boundary between the fluid and the plane, although used to model a slippery substrate rather than a porous medium.

Within this chapter the slip condition is enforced with an aim of informing future design of aeroengine bearing chamber walls.

Additional boundary conditions enforced are the tangential shear condition on the free surface and value of film flux. The boundary conditions and flux constraint

$$\begin{aligned} u &= -1 + \alpha \frac{\partial u}{\partial y} \quad \text{on} \quad y = 0, \\ \frac{\partial u}{\partial y} &= \tau \quad \text{on} \quad y = h, \\ q &= \int_0^h u \, \mathrm{d}y, \end{aligned} \tag{4.0.1}$$

lead to the set of simultaneous equations in the variables a_0, a_1 and a_2:

$$\begin{aligned} a_0 &= -1 + \alpha a_1, \\ a_1 &+ 2a_2 h = \tau, \\ a_0 h &+ a_1 \frac{h^2}{2} + a_2 \frac{h^3}{3} = q. \end{aligned} \tag{4.0.2}$$

Upon solution of the equations in (4.0.2), the velocity profile coefficients are given by

$$\begin{aligned} a_0 &= \frac{6\alpha q - 2h^2 - \alpha h^2 \tau}{2h(3\alpha + h)}, \\ a_1 &= \frac{6h + 6q - h^2 \tau}{2h(3\alpha + h)}, \\ a_2 &= \frac{3(2\alpha h \tau + h^2 \tau - 2h - 2q)}{4h^2(3\alpha + h)}. \end{aligned} \tag{4.0.3}$$

Following the formulation in Chapter 2, the integral term $\int_0^h u^2 \, \mathrm{d}y$ in Equation (2.3.10) is once again written as $I_h \frac{\partial h}{\partial x} + I_q \frac{\partial q}{\partial x}$, where the nonlinear coefficients I_h and I_q are now given by

$$\begin{aligned} I_h = \frac{1}{40h^2(3\alpha + h)^3} \Big(& 72\alpha^3 h^4 \tau^2 + 44\alpha^2 h^5 \tau^2 + 11\alpha h^6 \tau^2 + h^7 \tau^2 \\ & + 126\alpha^2 h^4 \tau + 84\alpha^2 h^3 q \tau + 38\alpha h^5 \tau + 18\alpha h^4 q \tau + 4h^6 \tau + 2h^5 q \tau \\ & - 1080\alpha^3 q^2 - 1080\alpha^2 h q^2 + 72\alpha h^4 + 96\alpha h^3 q \\ & - 336\alpha h^2 q^2 + 8h^5 - 48h^3 q^2 \Big), \\ I_q = \frac{7\alpha h^3 \tau + h^4 \tau + 360\alpha^2 q + 240\alpha h q + 8h^3 + 48h^2 q}{20h(3\alpha + h)^2}. \end{aligned} \tag{4.0.4}$$

Inserting the above coefficients into the general form of the depth-averaged thin-film approximation of the momentum equation (2.3.13) leads to

$$\mathrm{Re}^* \left(\frac{\partial q}{\partial t} + I_h \frac{\partial h}{\partial x} + I_q \frac{\partial q}{\partial x} \right) = \lambda h \sin\theta + \tau - \frac{6h + 6q - h^2\tau}{2h(3\alpha + h)} - \varepsilon\lambda h \cos\theta \frac{\partial h}{\partial x} + \frac{\varepsilon^3}{\mathrm{Ca}} h \frac{\partial^3 h}{\partial x^3}. \quad (4.0.5)$$

and the continuity equation (2.3.14) remains as

$$\frac{\partial h}{\partial t} + \frac{\partial q}{\partial x} = 0, \quad (4.0.6)$$

as in (3.1.10).

As noted within Chapter 2, a cubic expression in film height h for flux

$$q = \frac{\lambda h^3}{3} \sin\theta + \left(\frac{\tau}{2} + \alpha\lambda \sin\theta \right) h^2 + (\alpha\tau - 1)h \quad (4.0.7)$$

was derived, with parameters λ, θ, τ, and, importantly for this chapter, includes a slip length α. Figure 66 shows a plot of this cubic for varying α, with the dashed line for $\alpha = 0$ being comparable to Figure 10. The solid line

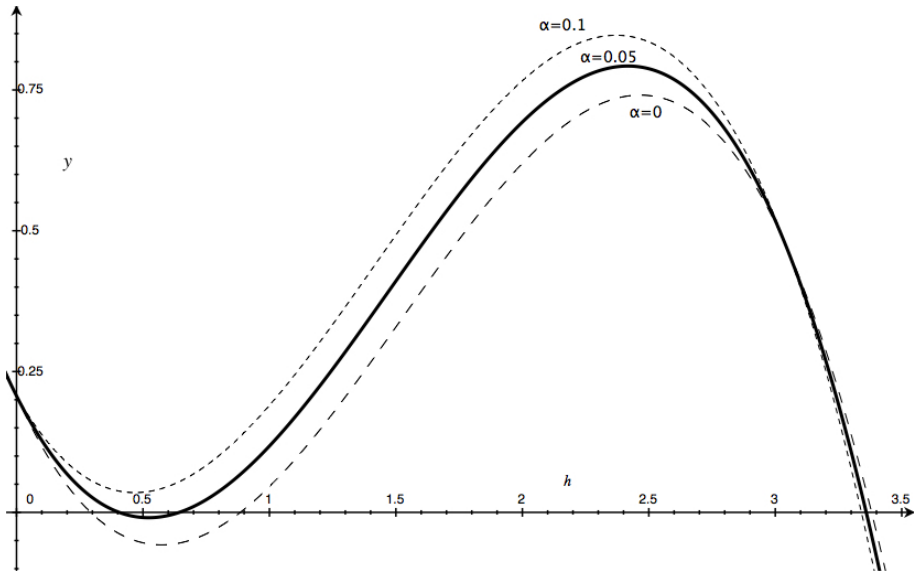


Figure 66.: $y = \frac{\lambda h^3}{3} \sin\theta + \left(\frac{\tau}{2} + \alpha\lambda \sin\theta \right) h^2 + (\alpha\tau - 1)h - q$ for different values of α. $\lambda = 1$, $\theta = -45$, $q = -0.2068$, $\tau = 2.14914$.

for $\alpha = 0.05$ is closer to a limiting case scenario that still allows for three distinct solutions when the horizontal axis approaches becoming tangential

to the turning point of the cubic graph. The limiting value of slip length is $\alpha = 0.0603$ and increasing the slip length further translates the minimum point in the positive y-direction until only a single Nusselt solution to the cubic equation is possible.

For the purposes of detailed numerical investigation within this chapter, the value of slip length is fixed at $\alpha = 0.05$ and compared to film profiles from Chapter 3, both with the non-inertial ($\mathrm{Re}^* = 0$) profiles and those obtained at $\mathrm{Re}^* = 10$. This allows a clear indication of the effects of increasing the slip length, or in a more physical sense, the material properties of the plane on which the wave profiles evolve. The solutions of cubic equation (4.0.7) are conjugate heights used as boundary and initial conditions for initial of wave disturbances; these are referred to as the low, intermediate and higher Nusselt film depths respectively.

4.1 MODELLING SLIP FLOW

For direct comparisons the film profiles within this section take the same values of parameters used in Chapter 3 i.e.

$$\lambda = 1,\ \mathrm{Ca} = 1 \times 10^{-4},\ \tau = 2.14914,\ q = -0.2068 \quad \text{and} \quad \varepsilon = 1 \times 10^{-2}. \tag{4.1.1}$$

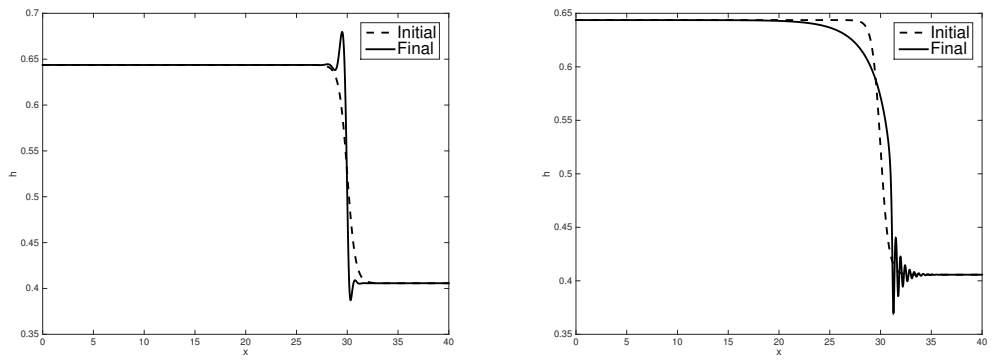
The angle of inclination is fixed as $\theta = -45$ in order to enable direct comparison to some of the profiles obtained in Chapter 3; the value of the dimensionless slip length is initially taken as $\alpha = 0.05$. This gives three corresponding values of the Nusselt heights as listed in Table 4. In a subsequent study α is increased to 0.1 to investigate the effects of only a single Nusselt height. These values of α are consistent a physical model for flow on a hydrophobic, or even super-hydrophobic surface. In a study by Bailey et al. [3], the slip length is given of the order of 50μm on such surfaces. Combined with the a film thickness of approximately 1mm, as is typical of thin-film

flows in a bearing chamber environment, these values yield a dimensionless slip length of $\alpha = \frac{L_s}{H} = 0.05$.

α	h_1	h_2	h_3
0	0.2933	0.8848	3.3809
0.01	0.3075	0.8451	3.3764
0.02	0.3241	0.8028	3.3721
0.03	0.3441	0.7571	3.3678
0.04	0.3696	0.7057	3.3637
0.05	0.4057	0.6437	3.3579

Table 4.: Nusselt heights. $q = -0.2068$ and $\lambda = 1$.

4.1.1 *Film profiles from multiple Nusselt solutions*

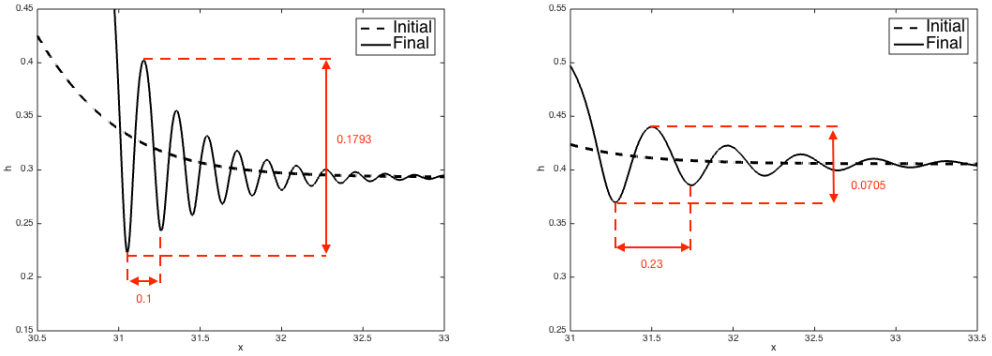


(a) $\mathrm{Re}^* = 0$ (b) $\mathrm{Re}^* = 10$

Figure 67.: Wave profiles. $\alpha = 0.05$, $h_l = h_2$, $h_r = h_1$.

Figure 67 shows profiles including slip at the fluid-plane boundary, which has the effect of reducing the severity of capillary ripples with the inclusion of inertia. At $\mathrm{Re}^* = 0$, very similar profiles are observed in comparison to Figure 17. Increasing film Reynolds number retains the overall structure of the standing wave formed, but there is a significant difference to be ob-

served in the formation of waves in the capillary region, as can be seen in Figure 68. Comparing figures 68a and 68b, it is noted that increasing the di-



(a) $\alpha = 0$ (Figure 17b) (b) $\alpha = 0.05$ (Figure 67b)

Figure 68.: Capillary waves for two values of α at $\mathrm{Re}^* = 10$.

mensionless slip length from $\alpha = 0$ to $\alpha = 0.05$ has the effect of reducing the amplitude and increasing the wavelength of the capillary ripples. With increasing slip length, the difference between h_1 and h_2 decreases, and the decreased severity of the capillary region is deduced to be a result of a smaller hydraulic jump, which in turn implies a smaller difference in the fluid velocities either side of the wave front. For further investigation, changes in values of slip length which still yield three unique Nusselt heights as a solution of Equation (4.0.7) are chosen and the capillary region examined. The Nusselt heights for the increasing values of α are summarised in Table 4.

Profiles are obtained for two different values of α, shown in Figure 68, with boundary $h_l = h_2$ and $h_r = h_1$ and the capillary regions examined for wavelength and amplitude. A distinct trend to be observed in Figure 69 is capillary wavelength increasing with slip length, whilst the amplitude of the capillary ripple closest to the main wave decreases. Increase in slip length at the fluid-plane boundary is seen to reduce the overall severity of the capillary region.

Figure 70 shows a three-tier initial profile gradually transitioning towards a two-tier solution and comparison with Figure 23 shows very similar de-

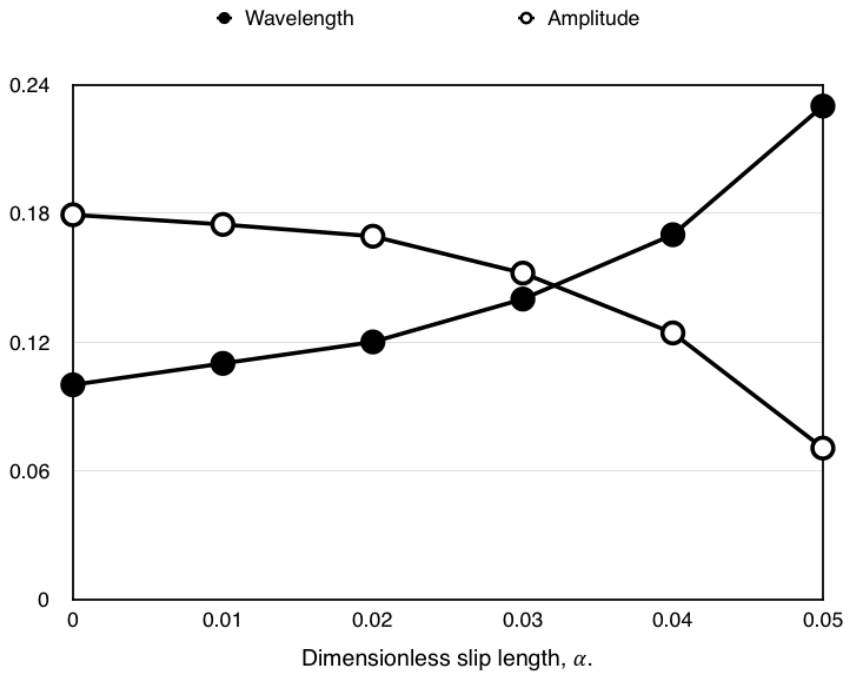
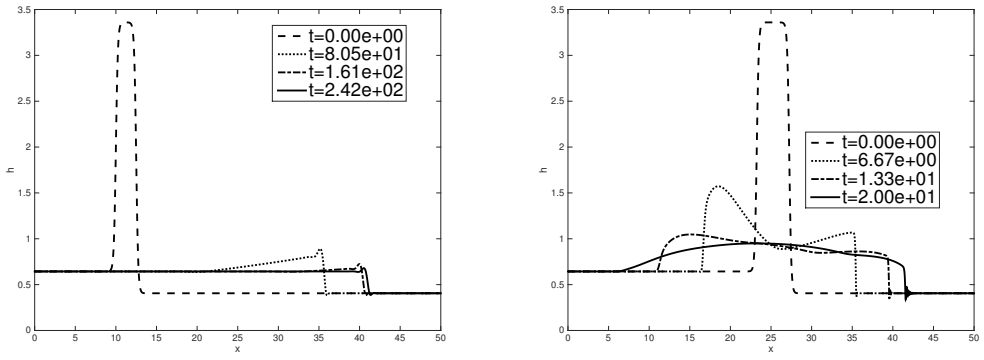


Figure 69.: Capillary wavelength increases and amplitude decreases with increasing slip length. $\theta = -45$, $\mathrm{Re}^* = 10$.



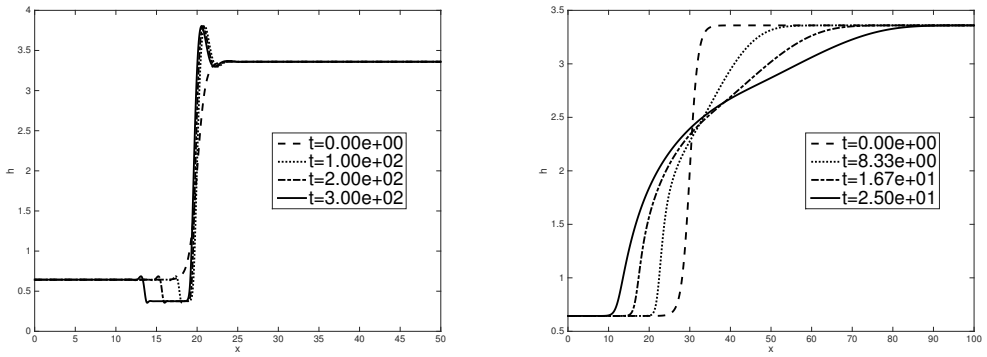
(a) $\mathrm{Re}^* = 0$ (b) $\mathrm{Re}^* = 10$

Figure 70.: Wave profiles. $\alpha = 0.05$, $h_l = h_2$, $h_m = h_3$, $h_r = h_1$.

velopment of the film. Again at $\mathrm{Re}^* = 0$, very little difference is observed in film profile development. When the film Reynolds number is increased to $\mathrm{Re}^* = 10$, the front travelling up the plane, in the increasing x-direction, significantly affects the capillary region when slip is included, with waves of reduced amplitude and increased wavelength. The downstream side of

the profile, towards the left-hand side of the domain, is much smoother in comparison to Figure 23b, with an almost non-existent front travelling down the plane. The trend is that over an extended period of time, the left hand side of the profile will tend towards the intermediate film thickness of $h = 0.6437$ and film profile as in Figure 70b.

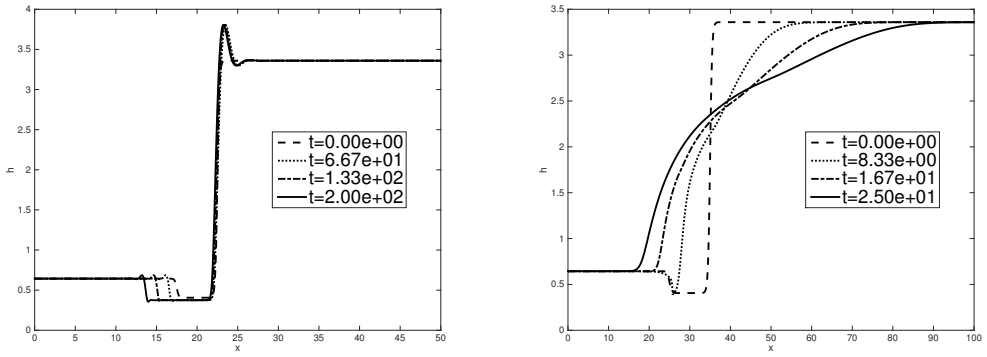
The two previous profiles in Figure 70 evolved into similar wave structures as when $\alpha = 0$ at $\mathrm{Re}^* = 0$. Slight differences were observed when inertia is included into the governing equations, although the overall structures of the profiles remained the same. In contrast, the profiles in figures 71-74 show the opposite. The equivalent profiles in figures 24a and 25a with $\alpha = 0$ and $\mathrm{Re}^* = 0$ evolve into a standing wave joining the intermediate and higher film depths. The equivalent profiles within the slip regime display a similar upward-facing standing wave, but with an additional tier at its base. The height of this tier in figures 71a and 72a is $h = 0.37$; this does not correspond to a solution of the cubic equation (4.0.7). This feature is similar to that observed in figures 26a and 27a, although in latter cases with different boundary conditions.



(a) $\mathrm{Re}^* = 0$ (b) $\mathrm{Re}^* = 10$

Figure 71.: Wave profiles. $\alpha = 0.05$, $h_l = h_2$, $h_r = h_3$.

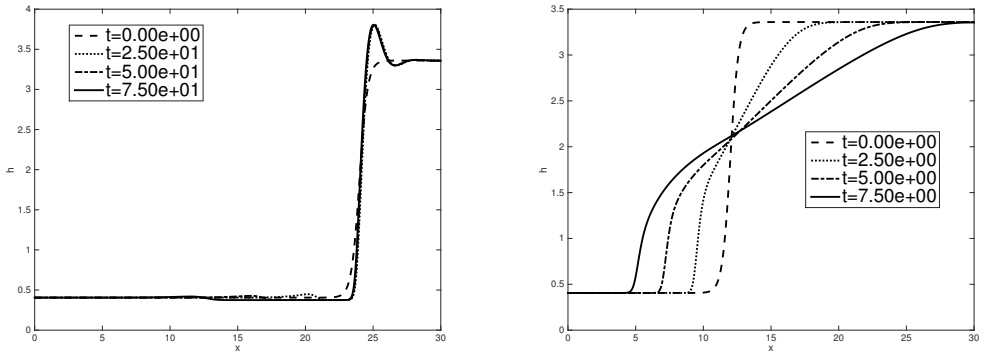
Profiles with equivalent initial and boundary conditions to figures 26 and 27 are seen in figures 73-74. The height of the tier formed is again $h = 0.37$, marginally lower than the lowest of the three conjugate heights. The consis-



(a) $\mathrm{Re}^* = 0$ (b) $\mathrm{Re}^* = 10$

Figure 72.: Wave profiles. $\alpha = 0.05$, $h_l = h_2$, $h_m = h_1$, $h_r = h_3$.

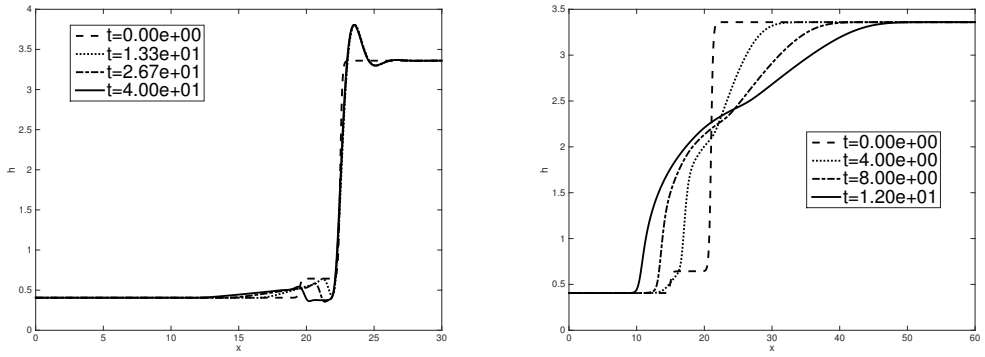
tency of the height of the newly-formed tier, from both two and three-tier initial profiles, indicates that this is a model feature, evolving independently of initial conditions and dependent on boundary conditions. With the film Reynolds number increased to $\mathrm{Re}^* = 10$, identical profile structures are observed both with and without the inclusion of the slip boundary condition.



(a) $\mathrm{Re}^* = 0$ (b) $\mathrm{Re}^* = 10$

Figure 73.: Wave profiles. $\alpha = 0.05$, $h_l = h_1$, $h_r = h_3$.

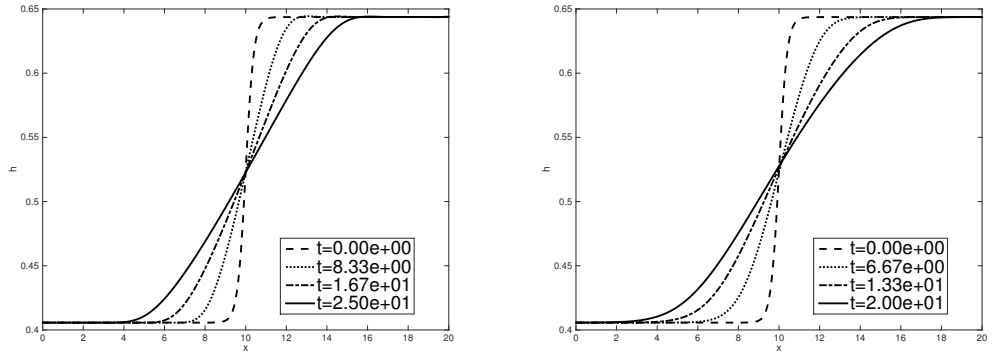
A further feature is rarefaction wave joining the lower and intermediate film depths, irrespective of whether $\alpha = 0$ or $\alpha = 0.05$. The inclusion of inertia has equivalent effect in both cases, with the rarefaction waves in figures 28b and 75b flattening slightly faster than their $\mathrm{Re}^* = 0$ counterparts.



(a) $\mathrm{Re}^* = 0$ (b) $\mathrm{Re}^* = 10$

Figure 74.: Wave profiles. $\alpha = 0.05$, $h_l = h_1$, $h_m = h_2$, $h_r = h_3$.

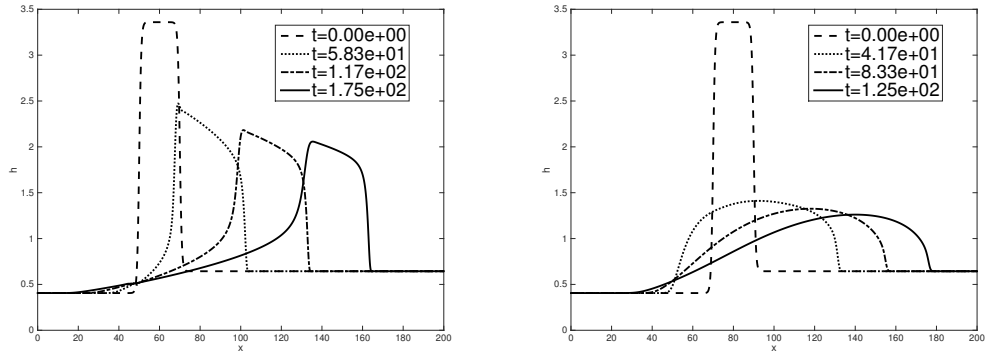
Comparison of film profiles in figures 28 and 29 with those in figures 75 and 76 identify common smoothing effects due to the inclusion of inertia.



(a) $\mathrm{Re}^* = 0$ (b) $\mathrm{Re}^* = 10$

Figure 75.: Wave profiles. $\alpha = 0.05$, $h_l = h_1$, $h_r = h_2$.

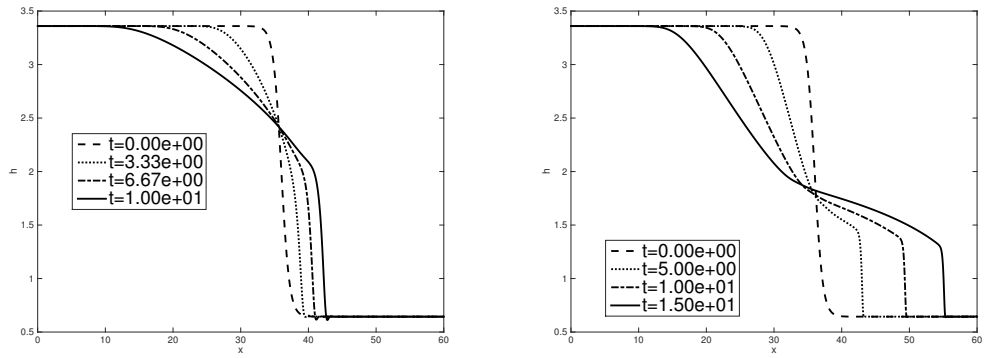
Figures 77-80 show wave profiles with slip conditions and are comparable to figures 30-33; these exhibit the formation of new fronts for increased values of the film Reynolds number. The non-inertial profiles with $\alpha = 0.05$ are found almost identical to their no-slip counterparts shown in the previous chapter. The profiles with $\mathrm{Re}^* = 10$ are similar in structure, but once again, the severity of the capillary region decreases with slip length and in the cases identified here, the capillary region is damped completely. With increasing slip length, the difference between the Nusselt heights h_1



(a) $\mathrm{Re}^* = 0$ (b) $\mathrm{Re}^* = 10$

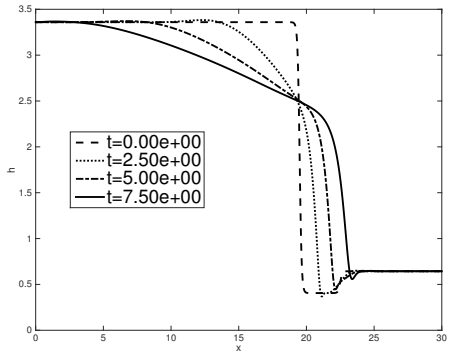
Figure 76.: Wave profiles. $\alpha = 0.05$, $h_l = h_1$, $h_m = h_3$, $h_r = h_2$.

and h_2 decreases, presenting less of a hydraulic jump for the fluid to contend with. This results in the decreased severity of the capillary region with increased slip length. The steepness of the main front remains and it can be observed that increased slip length has no effect in smoothing the profile in this instance.

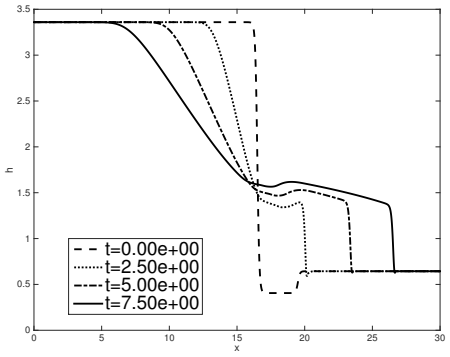


(a) $\mathrm{Re}^* = 0$ (b) $\mathrm{Re}^* = 10$

Figure 77.: Wave profiles. $\alpha = 0.05$, $h_l = h_3$, $h_r = h_2$.

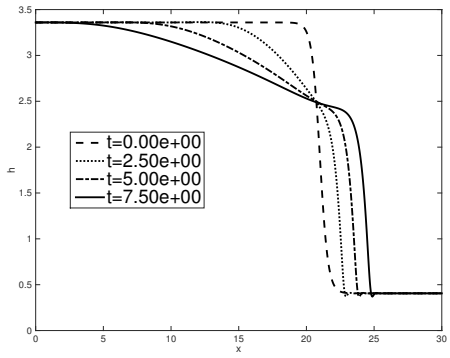


(a) $\mathrm{Re}^* = 0$

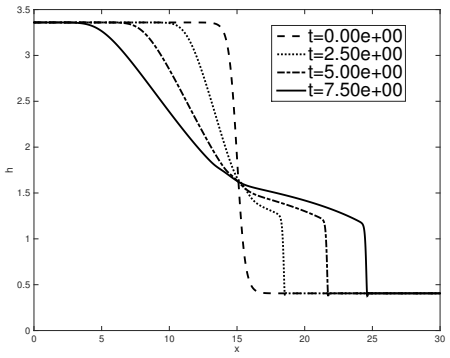


(b) $\mathrm{Re}^* = 10$

Figure 78.: Wave profiles. $\alpha = 0.05$, $h_l = h_3$, $h_m = h_1$, $h_r = h_2$.

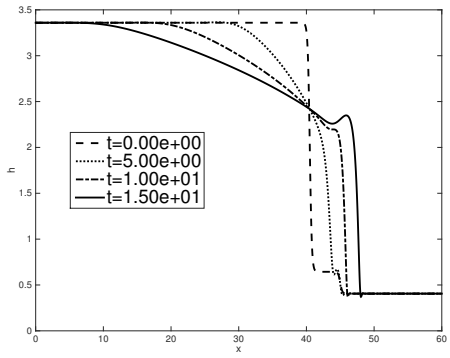


(a) $\mathrm{Re}^* = 0$

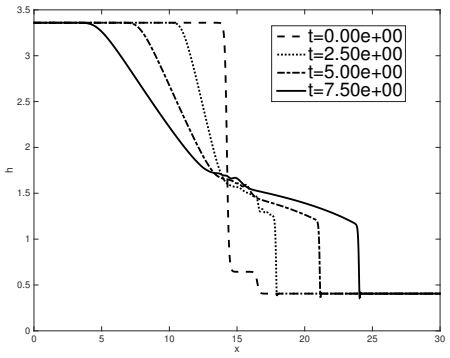


(b) $\mathrm{Re}^* = 10$

Figure 79.: Wave profiles. $\alpha = 0.05$, $h_l = h_3$, $h_r = h_1$.



(a) $\mathrm{Re}^* = 0$



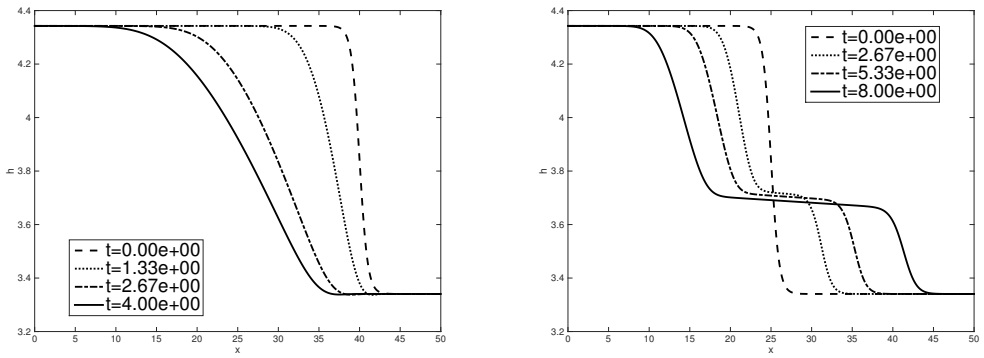
(b) $\mathrm{Re}^* = 10$

Figure 80.: Wave profiles. $\alpha = 0.05$, $h_l = h_3$, $h_m = h_2$, $h_r = h_1$.

4.1.2 *Film profiles from a single Nusselt solution*

Profiles with an increased dimensionless slip length of $\alpha = 0.1$ are now investigated. The cubic graph in Figure 66 confirms that at this value of α there is only one Nusselt solution, with value $h = 3.3405$. One boundary condition is fixed at the Nusselt height in the profiles in figures 81-82; for evaluation, the height of the other boundary is increased or decreased by 30% i.e. $h = 2.3384$ or $h = 4.3427$.

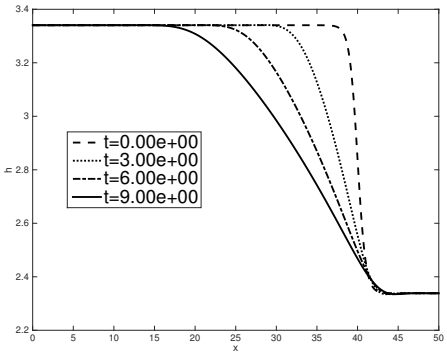
A common trend seen across the non-inertial ($\mathrm{Re}^* = 0$) profiles in figures 81-82 is the dominance of the right hand side boundary. The tier on the right hand side of the domain remains at a fixed height, whilst the fronts travel towards the left hand side boundary and reduce the height of the left hand tier. In some cases, such as in figures 81a and 82a, the wave structures are transient, whereas figures 83a and 84a depict standing wave structures retaining their shape whilst moving in the negative x-direction. The profiles which become standing wave structures have boundary conditions $h_r > h_l$, whilst those with $h_r < h_l$ continue to evolve.



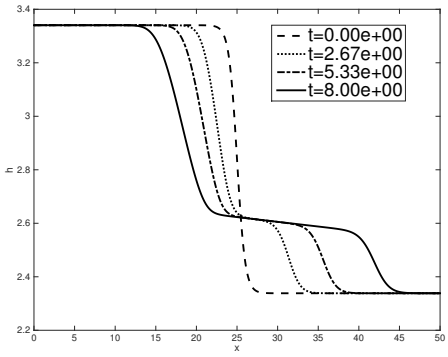
(a) $\mathrm{Re}^* = 0$ (b) $\mathrm{Re}^* = 10$

Figure 81.: Wave profiles. $\alpha = 0.1$, $h_l = 3.3405 + 30\%$, $h_r = 3.3405$.

Increasing the value of the reduced Reynolds number to $\mathrm{Re}^* = 10$, the formation of a secondary front is observed; such behaviour was previously seen in Section 3.3.2. The height of the tier which develops is unique to

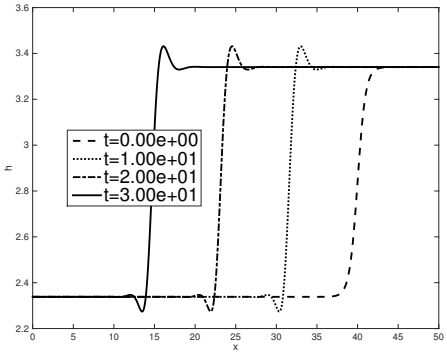


(a) $\mathrm{Re}^* = 0$

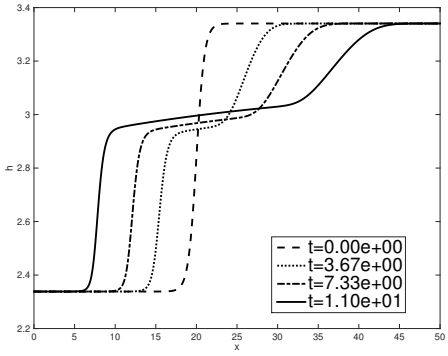


(b) $\mathrm{Re}^* = 10$

Figure 82.: Wave profiles. $\alpha = 0.1$, $h_l = 3.3405$, $h_r = 3.3405 - 30\%$.

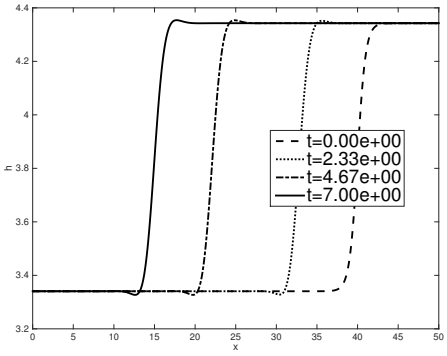


(a) $\mathrm{Re}^* = 0$

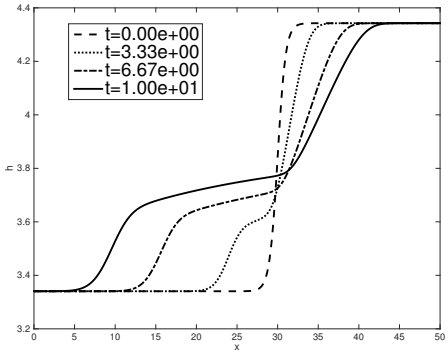


(b) $\mathrm{Re}^* = 10$

Figure 83.: Wave profiles. $\alpha = 0.1$, $h_l = 3.3405 - 30\%$, $h_r = 3.3405$.



(a) $\mathrm{Re}^* = 0$



(b) $\mathrm{Re}^* = 10$

Figure 84.: Wave profiles. $\alpha = 0.1$, $h_l = 3.3405$, $h_r = 3.3405 + 30\%$.

the selected boundary conditions, with $h \approx 3.7$ in Figure 81b, $h \approx 2.6$ in Figure 82b, $h \approx 3$ in Figure 83b and $h \approx 3.7$ in Figure 84b. The heights are approximate and not exact values due to the slope of the intermediate section which forms. The new tier, as opposed to the height of the right hand side boundary when $\mathrm{Re}^* = 0$, becomes dominant throughout the domain in these profiles. Outcomes imply that in this case inertia has a significant effect in these cases and modifies the profile structure and evolution substantially.

It is observed from figures 81-84 that the profiles in figures 81 and 82 are similar wave structures to each other, and those in Figure 83 and 84 are comparable. To aid with evaluation, velocity profiles of the flow are reconstructed and streamlines are produced for the two groups of wave structures, in a similar manner to Chapter 3.

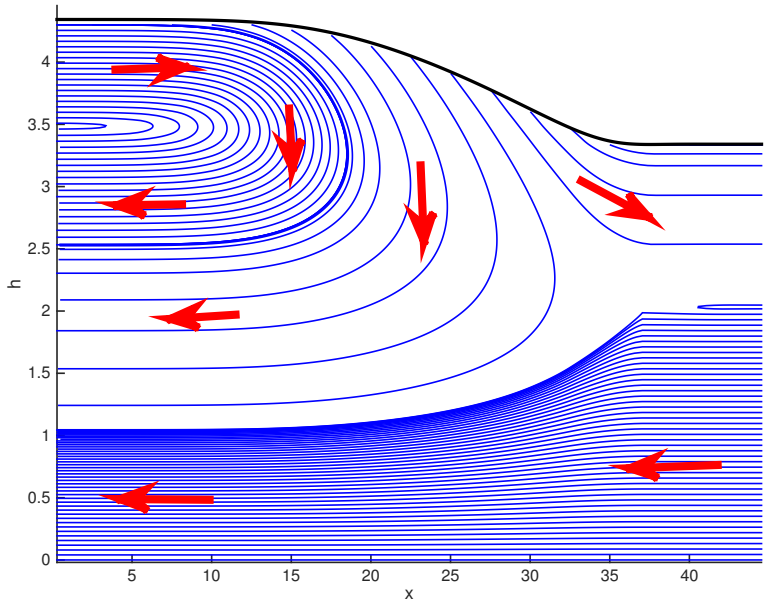
Figure 85 depicts streamlines constructed for both $\mathrm{Re}^* = 0$ and $\mathrm{Re}^* = 10$ profiles for the profiles in Figure 81, but an identical flow pattern is present in the profiles in Figure 82. The non-inertial flow in Figure 85a is considered first. A strong recirculation is present in the top-left region of the wave structure, with fluid entering from near the surface of the profile reversing in direction and exiting on the left hand side of the domain. Fluid from the surface of the wave front is transferred into the main part of the flow and exits to either the left-hand or right-hand side of the domain, dependent on its starting position within the domain. Below the recirculation region and the motion of the fluid particles initiating from the free surface, there is a base flow in the negative x-direction. The flux on the left hand side of the domain is $q = -3.78$, and on the right hand side of the domain, $q = -0.21$, indicating the there is a net flow of fluid out of the left hand side of the domain. This is consistent with the motion of the wave fronts as can be observed in figures 81 and 83.

The flow pattern when $\mathrm{Re}^* = 10$ is shown in Figure 85b. Strong similarities are observed with the non-inertial profile, notably the recirculation region present in the left hand side of the domain and a base flow in the

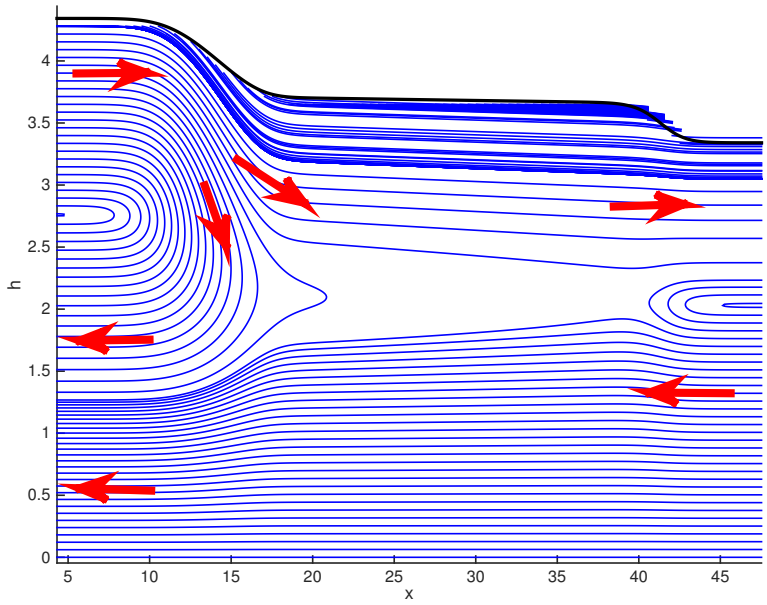
negative x-direction. A key difference is the strong flow in the positive x-direction just beneath the free surface. This is an important factor in the formation of the secondary front located at $x \approx 40$, with fluid being transferred from the left front to the right one. The pattern of streamlines is indicative of a advancing front, with particles from elsewhere within the fluid being transferred to the forefront of the structure. Of interest is the velocity profile through a recirculation region, which is further evaluated at $x = 5$ and $x = 45$, shown in Figure 86. The lower section of the velocity profile shows fluid velocities more negative than the wall speed, with the upper section showing fluid movement in the positive x-direction. The points corresponding to $u = 0$ on the velocity profiles are the centres of the recirculation regions, known as stagnation points.

Streamlines representative of the flow within wave structures in figures 83 and 84, with boundary conditions $h_l < h_r$, are given in Figure 87. The non-inertial flow in Figure 87a shows two recirculation regions, one on the left hand side of the domain and one on the right. The fluid near the plane is driven in the negative x-direction by the movement of the wall, whereas the fluid near the free surface travels in the positive x-direction due to the effects of the applied surface shear. Between these two layers, there is recirculation which results in stagnation points. At $\mathrm{Re}^* = 0$, there a positive fluid flux $q = 0.64$ to the left of the wave front, and a negative flux $q = -0.21$ to the right. The net flux is $q = 0.43$, meaning mass is being transferred into the domain and the front is seen advancing towards the left. This is consistent with the higher velocities of the fluid particles near the free surface.

The streamline plot in Figure 87b is illustrative of the profiles at $\mathrm{Re}^* = 10$. As previously, a base flow exists in the negative x-direction, whilst the flow near the free surface is in the positive direction, leading to the recirculation regions discussed for $\mathrm{Re}^* = 0$. Velocity profiles reconstructed at cross-sections taken at $x = 5$ and $x = 40$ in Figure 88 show recirculation regions. Streamlines depict fluid being removed from the right hand side wave front which leads to the receding wave front, as can be see from the



(a) $\mathrm{Re}^* = 0$



(b) $\mathrm{Re}^* = 10$

Figure 85.: Streamlines representative of fluid flow in wave structures corresponding to flow depicted in figures 81 and 82. $\alpha = 0.1$

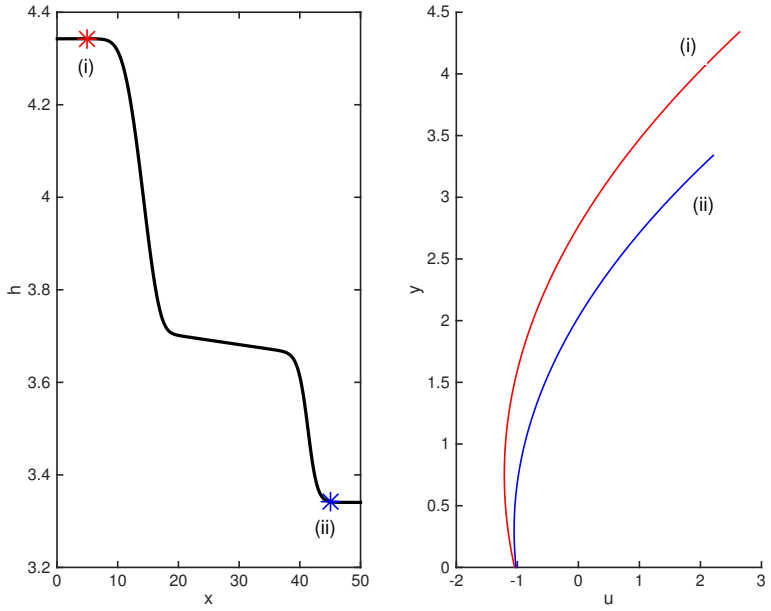
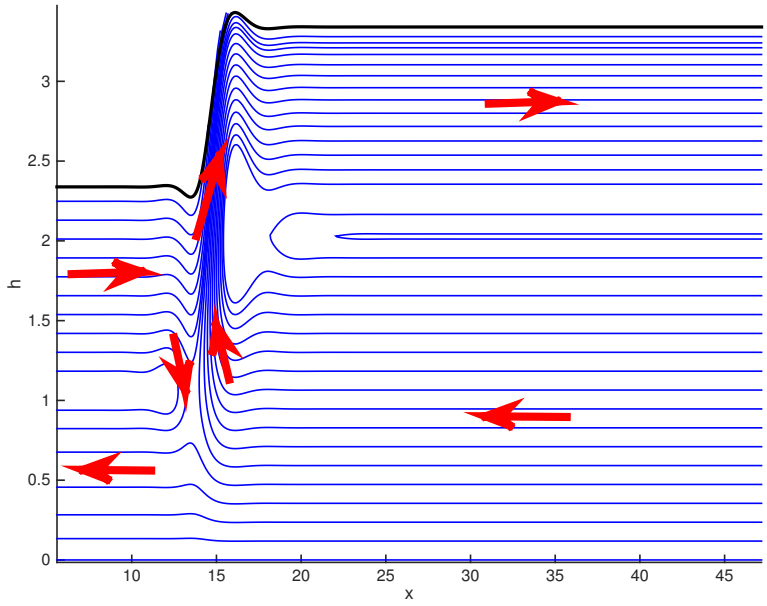


Figure 86.: Velocity profiles taken at cross-sections through the recirculation regions in Figure 85b.

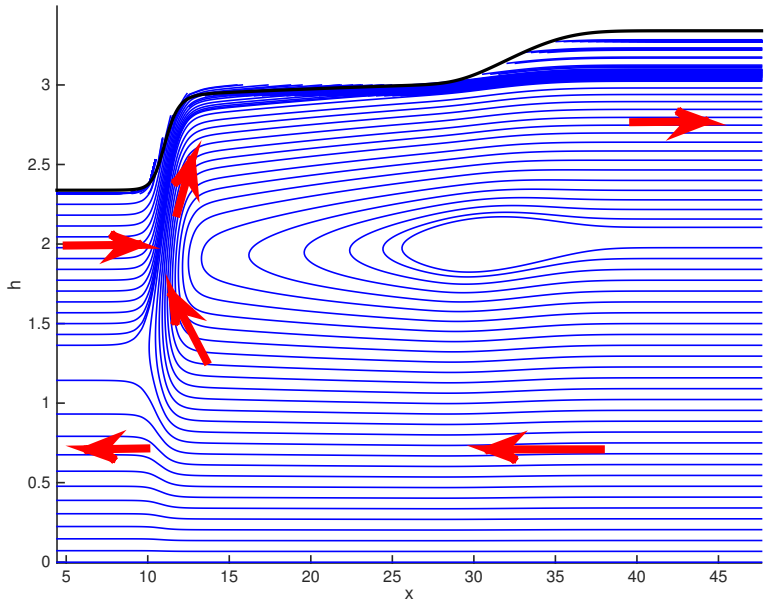
transient profiles given in figures 83b and 84b. The net flux in this case is $q = -0.15$, confirming fluid mass is overall removed from within the domain.

To further verify uniqueness of the heights of the new tier formed at $\mathrm{Re}^* = 10$, and overall shape of the wave structure at both $\mathrm{Re}^* = 0$ and $\mathrm{Re}^* = 10$, one boundary is retained at the Nusselt height and the height of the other boundary varied. The height of the boundary is changed by 30% of the Nusselt height and outcomes for variations of 10% and 20% are shown in Figure 89. Comparison is made with the transient profiles in Figure 81; the height of the right hand boundary is fixed at $h = 3.3405$, with the left hand boundary increased by a proportion.

The profiles in Figure 89 suggest that the structure of the waves is consistent with those in Figure 81. A 10% difference between the boundary heights leads to intermediate tier formation at a height of $h = 3.45$, a 20% difference forms a tier at $h = 3.56$ and a 30% difference, as seen in Figure



(a) $\mathrm{Re}^* = 0$



(b) $\mathrm{Re}^* = 10$

Figure 87.: Streamlines representative of fluid flow in wave structures depicted in figures 83 and 84. $\alpha = 0.1$

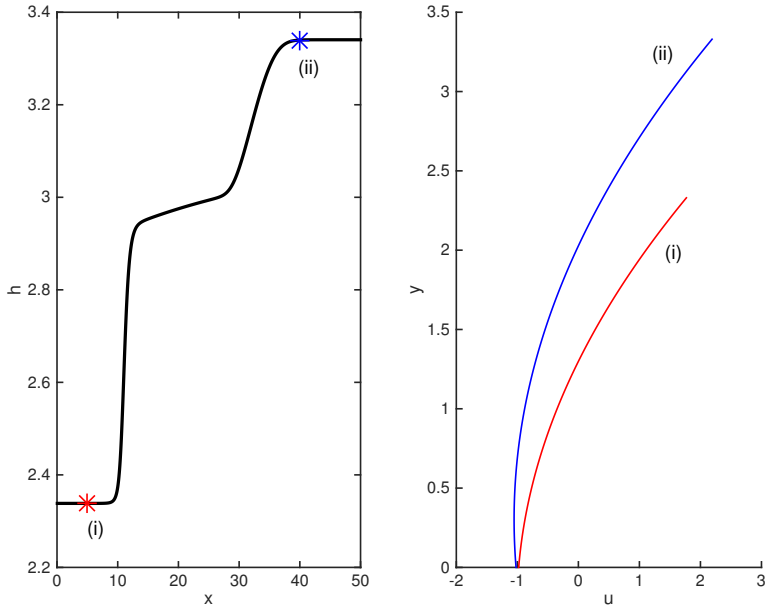
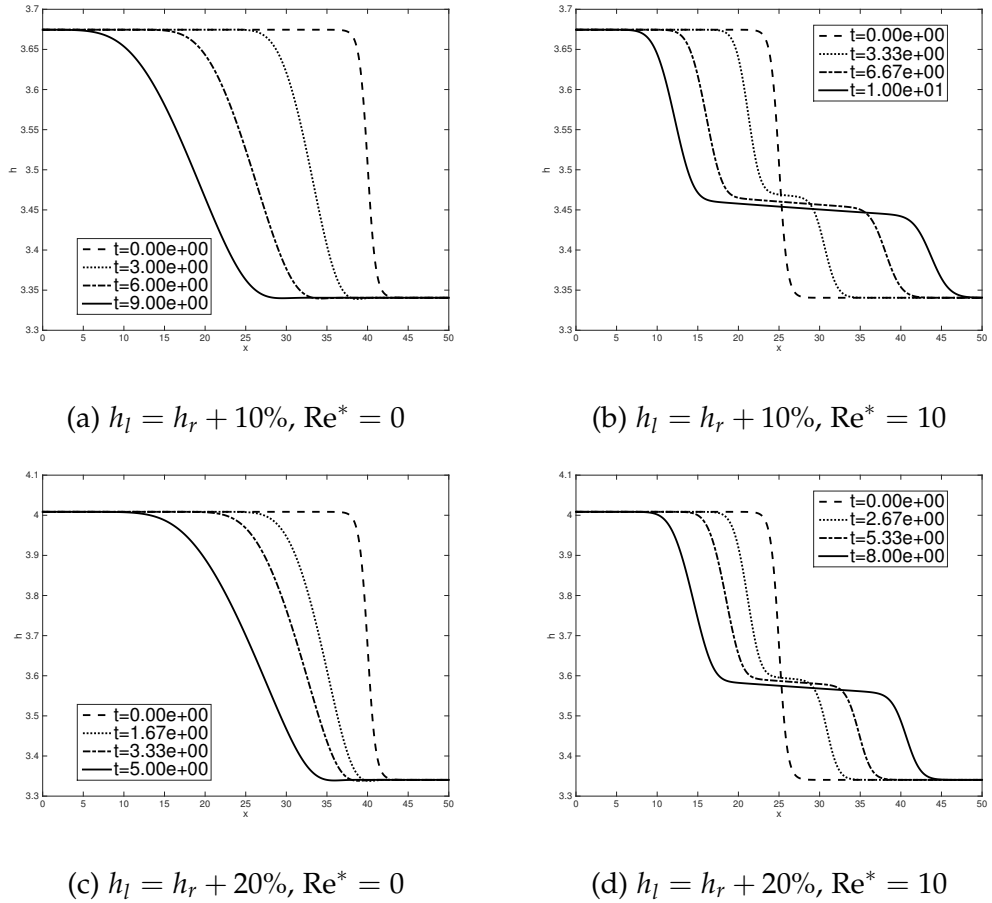


Figure 88.: Velocity profiles taken at cross-sections through the recirculation regions in Figure 87b.

81b, leads to a tier at $h = 3.68$. A conclusion is that tier formation observed is not independent of boundary conditions.



(a) $h_l = h_r + 10\%$, $\mathrm{Re}^* = 0$

(b) $h_l = h_r + 10\%$, $\mathrm{Re}^* = 10$

(c) $h_l = h_r + 20\%$, $\mathrm{Re}^* = 0$

(d) $h_l = h_r + 20\%$, $\mathrm{Re}^* = 10$

Figure 89.: Variations on the left hand boundary height whilst fixing the right hand boundary at the Nusselt height. $\alpha = 0.1$.

4.2 OVERVIEW OF THE CHAPTER

Within this chapter, the effect of a slip boundary condition was evaluated within the earlier no-slip formulation given in Chapter 2. Shear-driven flow was considered, acting in the opposite direction to gravity. Initial conditions were chosen as the conjugate height solutions of the cubic equation arising from considering a steady, uniform flow. Values of slip length α were limited by the number of solutions to this cubic equation, with too large a value allowing only one Nusselt height.

A notable effect of including moderate slip on the boundary between the fluid and the plane is the decrease in severity of the capillary region. With

increasing slip the wavelength of the capillary ripples was increased and the amplitude decreased. Wave structures with higher inertia ($\mathrm{Re}^* = 10$) were on the whole observed to be smoother at $\alpha = 0.05$ than with the no-slip condition. A key difference between the $\mathrm{Re}^* = 0$ profiles observed in figures 71-74 and those from the previous chapter, figures 24a and 25a, is the formation of a wave tier of height $h = 0.37$, which was not observed in the latter set of profiles. This was a feature present in profiles obtained at $\mathrm{Re}^* = 10$, when inertial terms are included. The physical justification behind the decrease in the severity of the capillary region is presumed to be due to the difference between the Nusselt heights. With increasing slip length, Nusselt heights h_1 and h_2 move closer together, as can be seen in Figure 66. This results is a smaller hydraulic jump for the fluid, and so the effects of the near-shock wave are reduced.

Increasing the slip length to $\alpha = 0.1$ has the effect of reducing the number of conjugate heights possible from three to just one unique solution of the cubic equation for constant flux (4.0.7). Taking initial profiles such that one boundary was fixed, the effects of inertia on a selection of these profiles was investigated. It was found that with the inclusion of inertia, an intermediate tier was formed, similar to those observed in Chapter 3. The height of the intermediate tier appears to be unique to the boundary conditions and the initial profile from which it evolves. The flow dynamics within the associated wave structures was investigated through the construction of streamlines and velocity profiles; recirculation regions were confirmed present within the flow, which result in the propagation of the intermediate tiers of fluid.

5

MODELLING OF SOLITARY WAVES ON AN INCLINED PLANE

This chapter considers the formation, structure and stability of solitary waves. Solitary waves within flow down an inclined plane are known to evolve from perturbations at the inlet. Typically these grow in amplitude into a series of near-identical repeating wave structures. Gjevik [19] notes that this happens for flows with sufficiently strong surface tension. In this chapter a mathematical model is developed that incorporates a surface tension parameter together with inertial effects which are later shown to play a key role in the stability of these wave structures.

Numerical implementation of the integral boundary layer model has some well-known criticisms concerning the overprediction of the amplitude of capillary ripples in solitary waves, as well as the point of onset of instability when assuming a quadratic velocity profile for the thin-film flow. To investigate solitary waves in greater detail, the quadratic and cubic models developed in sections 3.1 and 3.4 respectively are adapted to study the wave development on an inclined plane from an oscillating inlet boundary. The pulses produced at this boundary subsequently develop into the solitary waves to be studied.

Initially a gravity-driven flow is investigated within a fixed frame of reference by imposing a modified no-slip boundary condition

$$u = 0 \quad \text{on} \quad y = 0. \tag{5.0.1}$$

The boundary condition at the free surface is

$$\frac{\partial u}{\partial y} = 0 \quad \text{on} \quad y = h \tag{5.0.2}$$

and the definition of flux remains as

$$q = \int_0^h u \, \mathrm{d}y. \tag{5.0.3}$$

Assuming the streamwise velocity component of the flow to be of a quadratic form as

$$u = a_0 + a_1 y + a_2 y^2, \tag{5.0.4}$$

and satisfying the conditions (5.0.1-5.0.3) leads to the values of the quadratic coefficients a_i of the form

$$\begin{aligned} a_1 + 2a_2 h &= 0, \\ a_0 &= 0, \\ a_0 h + a_1 \frac{h^2}{2} + a_2 \frac{h^3}{3} &= q. \end{aligned} \tag{5.0.5}$$

The quadratic velocity profile coefficients, given by solving the equation set (5.0.5) are

$$\begin{aligned} a_0 &= 0, \\ a_1 &= \frac{3q}{h^2}, \\ a_2 &= -\frac{3q}{2h^3} \end{aligned} \tag{5.0.6}$$

and can be used to obtain expressions for $I_h = \frac{\partial}{\partial h} \int_0^h u \, \mathrm{d}y$ and $I_q = \frac{\partial}{\partial q} \int_0^h u \, \mathrm{d}y$ as

$$I_h = -\frac{6q^2}{5h^2} \tag{5.0.7}$$

and

$$I_q = \frac{12q}{5h}. \tag{5.0.8}$$

Alternatively, if a cubic velocity profile is assumed, of the form

$$u = b_0 + b_1 y + b_2 y^2 + b_3 y^3, \tag{5.0.9}$$

the cubic coefficients b_i are determined from

$$\begin{aligned} &b_1 + 2b_2h + 3b_3h^2 = 0, \\ &b_0 = 0, \\ &b_0h + b_1\frac{h^2}{2} + b_2\frac{h^3}{3} + b_3\frac{h^4}{4} = q, \\ &2b_3 + \lambda \sin\theta = 0, \end{aligned} \tag{5.0.10}$$

constraints arising from again satisfying conditions (5.0.1-5.0.3), with the additional condition of

$$0 = \frac{\partial^2 u}{\partial y^2} + \lambda \sin\theta. \tag{5.0.11}$$

Further details on the derivation of (5.0.11) are given in Section 3.4. This leads to modified values of the velocity profile coefficients for both quadratic and cubic cases. Values for the cubic profile coefficients are

$$\begin{aligned} b_0 &= 0, \\ b_1 &= \frac{\lambda h \sin\theta}{5} + \frac{12q}{5h^2}, \\ b_2 &= -\frac{\lambda \sin\theta}{2}, \\ b_3 &= \frac{4\lambda \sin\theta}{15h} - \frac{4q}{5h^4}, \end{aligned} \tag{5.0.12}$$

and the integral coefficients are

$$J_h = \frac{5\lambda^2 h^6 \sin^2\theta - 82h^3\lambda q \sin\theta - 3264q^2}{2625h^2} \tag{5.0.13}$$

and

$$J_q = -\frac{41h^3\lambda \sin\theta - 6528q}{2625h}. \tag{5.0.14}$$

J_h and J_q are defined in a similar fashion to I_h and I_q, with u now representing the cubic velocity profile instead.

Following the approach of earlier chapters the momentum equation becomes

$$\mathrm{Re}^* \left(\frac{\partial q}{\partial t} + I_h \frac{\partial h}{\partial x} + I_q \frac{\partial q}{\partial x} \right) = \lambda h \sin\theta - \frac{3q}{h^2} - \varepsilon\lambda h \frac{\partial h}{\partial x}\cos\theta + \frac{\varepsilon^3}{\mathrm{Ca}} h \frac{\partial^3 h}{\partial x^3} \tag{5.0.15}$$

for the quadratic velocity profile case, and

$$\mathrm{Re}^* \left(\frac{\partial q}{\partial t} + J_h \frac{\partial h}{\partial x} + J_q \frac{\partial q}{\partial x} \right) = \frac{4}{5} \lambda h \sin\theta - \frac{12q}{5h^2} - \varepsilon \lambda h \frac{\partial h}{\partial x} \cos\theta + \frac{\varepsilon^3}{\mathrm{Ca}} h \frac{\partial^3 h}{\partial x^3} \quad (5.0.16)$$

for the cubic velocity profile case. The continuity equation is

$$\frac{\partial h}{\partial t} + \frac{\partial q}{\partial x} = 0. \quad (5.0.17)$$

The mathematically assumed far field outlet boundary condition remains as

$$h = h_r,\, q = q_r \quad \text{as} \quad x \to \infty, \quad (5.0.18)$$

for wave structures far enough away from the outlet. The inlet boundary is adjusted to create the disturbance which then evolves into a solitary wave. An oscillating boundary with sinusoidal motion is imposed from an inlet boundary condition

$$h = h_l + A \sin(2\pi f t), \quad (5.0.19)$$

where A controls the amplitude of the oscillation and f the forcing frequency. The inlet flux, derived from assuming steady, uniform flow in (5.0.15) and (5.0.16), is defined as

$$q_l = \frac{1}{3} h_l^3 \lambda \sin\theta \quad (5.0.20)$$

and will vary with the height of the inlet boundary h_l.

5.1 VALIDATION AND COMPARISON WITH EXPERIMENTAL PROFILES

As an initial study the model is validated against existing experimental data to verify whether the physical features are being captured. The near-horizontal flow experiment detailed by Liu and Gollub [29] has repeatedly been the benchmark against which numerical simulations are compared. Liu and Gollub experiment with a mixture of 54% glycerine by mass, with a kinematic viscosity of 6.28 centistokes and a surface tension of 67 dyn/cm.

Glycerine has a density of 1.26 g/cm^3, which, as a 54% mixture, corresponds to $\rho = 1.13730$ g/cm^3 at 20^{o}C and $\rho = 1.13465$ g/cm^3 at 25^{o}C. A simple linear interpolation provides us with the density of the glycerine-water mixture $\rho = 1.13624$ g/cm^3, at 22^{o}C - the temperature at which the experiment is carried out. Scheid et al. [47] have produced an overlay of various numerical models highlighting a leading wave feature and preceding capillary region, a feature that appears periodically. In order to produce a plot of the current model against experimental data, parameters are taken from the same source [29].

Table 5 gives these parameters in units as they originally appear in [29], as well as their equivalent values in SI units, which are more useful for inclusion in our numerical simulation. Kinematic viscosity ν is the ratio of

Variable	**Original units**	**SI units**
Density (ρ)	1.13624 g/cm^3	1136.24 kg/m^3
Kinematic viscosity (ν)	6.28 cSt	6.28×10^{-6} m^2/s
Surface tension (σ)	67 dyn/cm	0.067 N/m

Table 5.: Parameters from [29] experiment in original and SI units.

the dynamic viscosity μ to the density of the fluid ρ. Therefore the dynamic viscosity is obtained by

$$\mu = \rho\nu = 7.1356 \times 10^{-3}\,\text{kg}\ \ \text{m}^{-1}\text{s}^{-1}, \tag{5.1.1}$$

again in SI units.

Liu et al. [29] define the Reynolds number as $\text{Re} = \frac{\rho U_0 h_0}{\mu}$ and the Weber number as $\text{W} = \frac{\sigma}{\rho g h_0^2 \sin\beta}$. For this particular experiment, the plane is almost horizontal, inclined at an angle $\theta = 6.4^\circ$, with dimensionless fluid parame-

ters Re = 29 and W = 35. From these values of h_0 and U_0, typical values of film thickness and film velocity, may be obtained.

$$h_0 = \sqrt{\frac{\sigma}{\rho g W \sin\beta}} = 1.24188 \times 10^{-3},$$
$$U_0 = \frac{\mu\,\mathrm{Re}}{\rho h_0} = 0.14665. \tag{5.1.2}$$

Using the dimensionless values h_0 and U_0, which correspond to H and U respectively, it is possible to obtain values for the parameters in the current model as

$$\mathrm{Re} = 29, \quad \lambda = 16.41132 \quad \text{and} \quad \mathrm{Ca} = 1.56184 \times 10^{-2}. \tag{5.1.3}$$

In this section the model has been derived under the assumption that $\varepsilon\,\mathrm{Re} \sim \mathcal{O}(1)$, leading to the value of the film depth-aspect ratio as $\varepsilon = 0.1$. This is also consistent with $\frac{\varepsilon^3}{\mathrm{Ca}} \sim \mathcal{O}(\varepsilon)$. The experiment is carried out on a plane of length 2 metres, which, in the dimensionless coordinate system measures as

$$x = \frac{\varepsilon}{H}\bar{x} = 161, \tag{5.1.4}$$

and can be used as a guide for the length of the numerical domain. In the coordinate direction perpendicular to the plane, Liu et al. [29] report on a film thickness of 1cm, with the approximate length a typical solitary wave structure being 10cm. This again is consistent with the assumption of $\varepsilon = 0.1$, and so enables direct comparison when transformed into a dimensionless coordinate system.

Numerical implementation of the oscillating inlet boundary height, for replication of the solitary waves observed in the experiment, is adapted from the constant sinusoidal motion in Equation (5.0.19). An inlet boundary is instead pulsed as the periodic positive half of a sine wave and then kept constant at $h = 1$ for the remainder of the cycle; as well as for a number of resting cycles. This periodic set of actions at the inlet boundary is used to control the motion of the perturbations travelling downstream. Liu and Gollub [29] note that in the evolution of sinusoidal inlet perturbations, the

initial waves separate and it is the primary peaks which grow to reach a constant amplitude. The frequency of the wave and number of resting cycles may be varied as required, with higher-frequency waves producing peaks which are closer together. A visual interpretation of the inlet boundary motion is given in Figure 90, where the height pulses from $h = 1$ to $h = 1.4$ for half a sine wave cycle, then return to rest for 2.5 cycles.

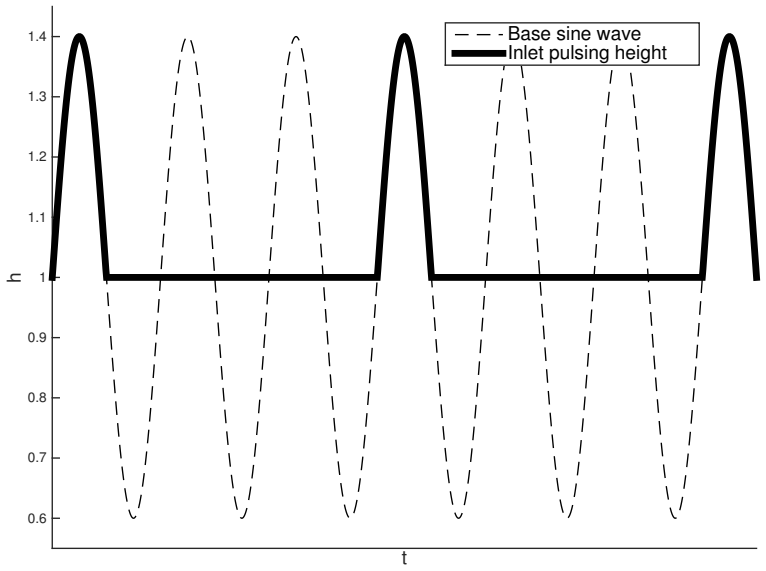


Figure 90.: Model pulsing input of inlet boundary disturbance.

In modelling this system in the extended length of domain required for solitary waves to form from the inlet perturbations, the overall number of solution nodes required is found to be significant. In order to reduce computational cost, both in terms of memory requirement as well as solution time, a numerical smoothing is utilised. The 5-point smoothing formula given by Longuet-Higgins et al. [31] as

$$\bar{f}_j = \frac{1}{32}\left(-f_{j-3} + 9f_{j-1} + 16f_j + 9f_{j+1} - f_{j+3}\right) \tag{5.1.5}$$

is used to damped numerical oscillations in calculations observed where numerically-based disturbances were much shorter than the wavelength of the capillary ripples which form.

Model parameters were taken as (5.1.3) and the inlet boundary pulsing as in Figure 90. Numerical calculations of the growth of the pulses showed development into fully-formed solitary waves, as shown in Figure 91. The leading wave, due to the lack of stabilisation by any structure preceding it, continues to grow whilst the following wave development remains more bounded in height. The perturbations at the inlet boundary are at an am-

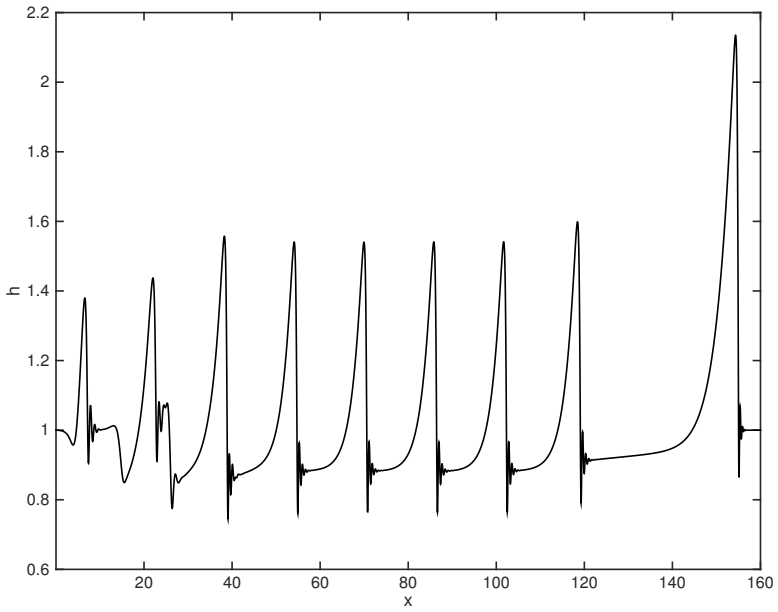


Figure 91.: Development of solitary waves replicating experiment by Liu et al. [29], with Re $= 29$.

plitude of 0.4, leading to an initial maximum height of $h = 1.4$. A rapid increase in this height is observed, with the main solitary waves settling at a height of $h \approx 1.5$. To further assess the capability of the model at capturing the film dynamics, validation is obtained by pulsing the inlet boundary to half the amplitude; this is shown for the wave profile in Figure 91. In Figure 92 it is observed that the pulses grow in height until they achieve a comparable height of $h \approx 1.5$, after which they form a set of near-identical solitary waves. The leading front is again seen not only growing to a much greater height, but also more rapidly due to the lack of stabilisation from downstream. It is noted that the height of the leading fronts cannot be com-

pared directly due to the increased length of domain in Figure 92. This is a result of a profile with a lower initial amplitude needing a both a longer domain and time to develop into a consistent set of solitary waves.

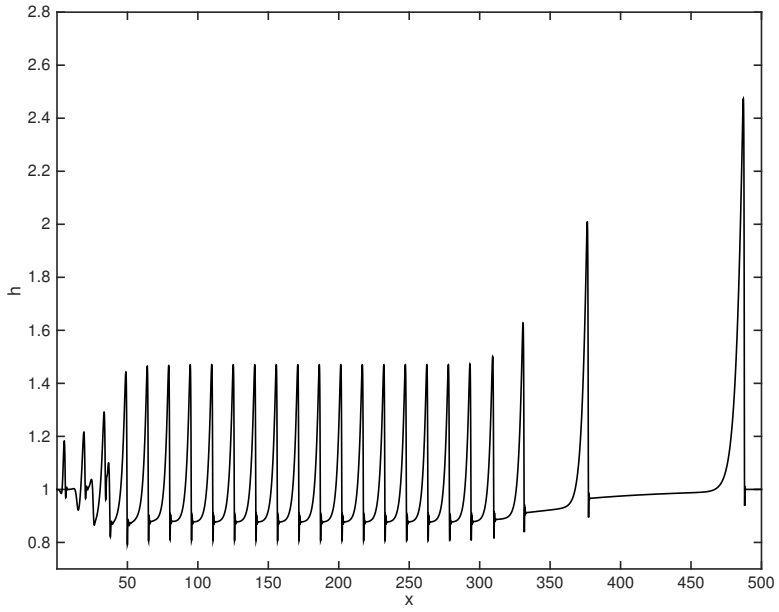


Figure 92.: Evolution of solitary waves from half the initial perturbation amplitude as in Figure 91, with Re $= 29$.

The simulation shown in Figure 91, which assumes a quadratic velocity profile is now compared to the model incorporating a cubic velocity profile. Numerically, this involves replacing momentum equation (5.0.15) with (5.0.16) and solving with the associated integral coefficients J_h and J_q. The continuity equation (5.0.17) and all boundary conditions remain unchanged. Figure 93 depicts an overlay of the experimental profile from [29] with the profiles obtained through both quadratic and cubic depth-averaged thin-film models. Good agreement is obtained with the experimental profile structure in both cases, with the cubic model producing capillary waves with marginally greater amplitude.

A verification of the numerical simulation is also performed to check whether the mesh density is sufficient to capture the features consistently. In Figure 94 two profiles are observed, one with the number of interior

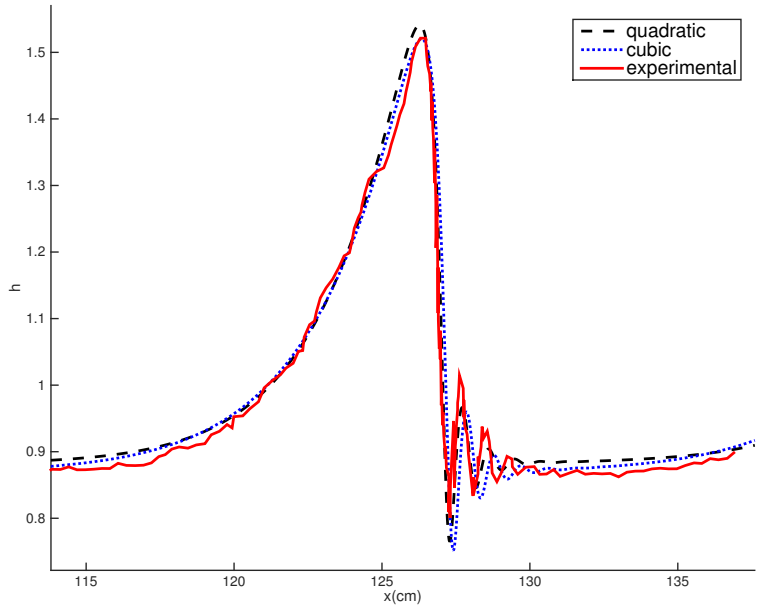


Figure 93.: Quadratic and cubic models compared against the experimental profile in [29], with Re = 29.

domain nodes as $n = 10000$ and the other with $n = 15000$; this confirms agreement.

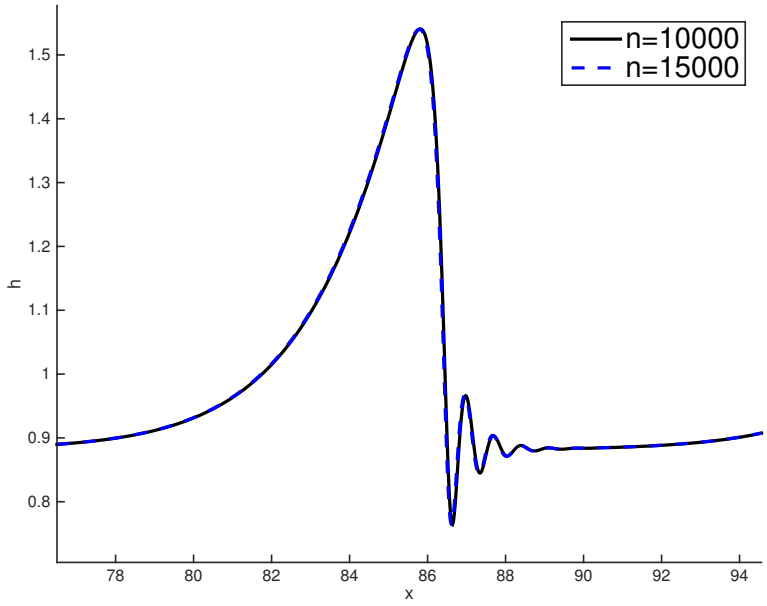


Figure 94.: Verification of solitary wave for node densities $n = 10000$ and $n = 15000$.

5.2 EFFECTS OF INCREASING REYNOLDS NUMBER OF SOLITARY WAVES

Retaining the values of λ and Ca from Liu and Gollub, the reduced Reynolds number is modified as a modelling experiment to investigate the effect of inertia on this particular solution. A point of particular interest is the stability of the solution, which, below a critical Reynolds number, produces a series of oscillations that decay, such as displayed in Figure 95 for $\mathrm{Re}^* = 0.1$. The stability characteristics of solitary waves are investigated in Section 5.3 in greater depth. For the purposes of this section, the left hand boundary is again perturbed in the manner described in Figure 90 and the fully-formed solitary wave structures are studied. The mass of fluid travelling ahead of the decaying perturbations in Figure 95 is due to this unsymmetrical perturbation method.

An increase in the film Reynolds number leads to the formation of solitary waves discussed above, together with the much smaller wavelength capillary waves. This is a much investigated feature by many authors, such

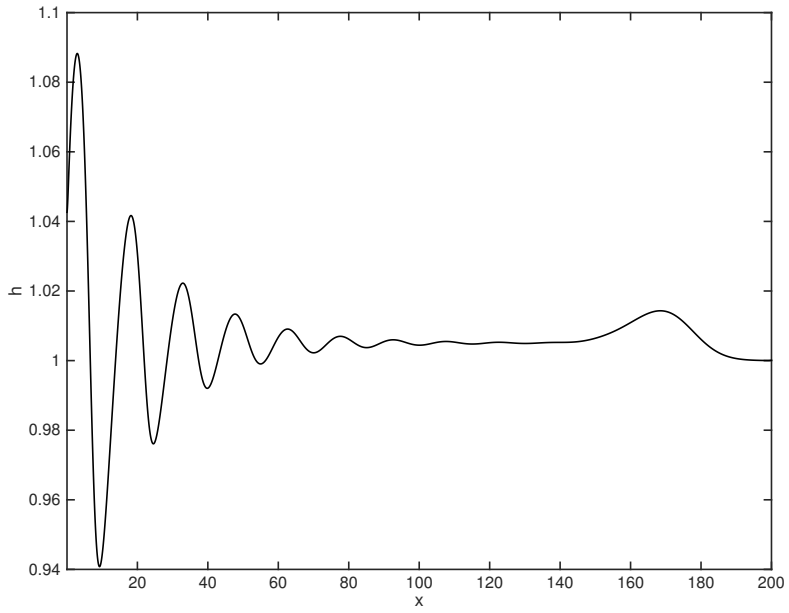
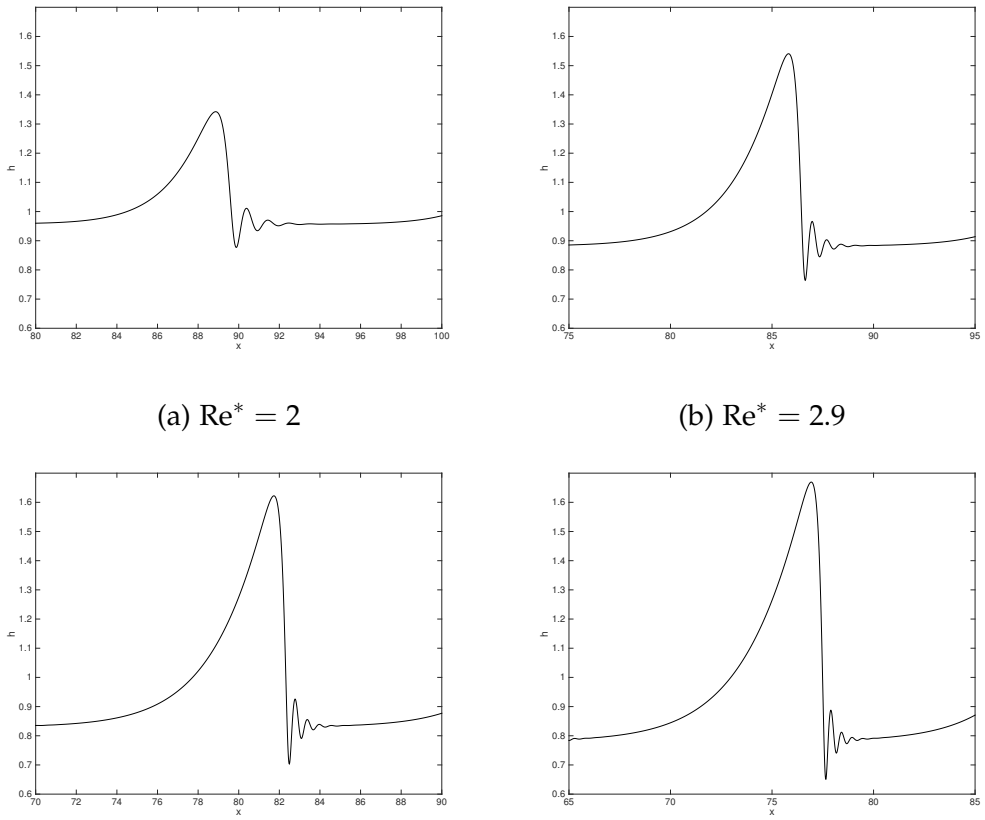


Figure 95.: Perturbations decay when the Reynolds number ($\mathrm{Re}^* = 0.1$) is below the critical threshold. The perturbations are initiated by pulsing at inlet boundary (see Figure 90).

as Ruyer-Quil et al. [40], who report that solitary waves form when the film Reynolds number is increased above a critical Reynolds number. In figures 96a-96d we observe the height of the primary peak increasing with Reynolds number, from $h_{\max} = 1.34$ at $\mathrm{Re}^* = 2$, to $h_{\max} = 1.67$ at $\mathrm{Re}^* = 5$. Along with the increase in the height of the main wave, the first capillary wave is seen increasing in amplitude by 73% whilst the wavelength decreases by 49%, exhibiting what can be viewed as a more severe capillary region with increasing inertial effects. Both of these observations are consistent with numerical simulations by Kandel et al. [22], although direct comparison cannot be made since these authors investigate solitary wave formation on an inclined porous surface.

Of interest is the flow dynamics within the capillary region, particularly at larger Reynolds numbers, which will give insight into the nature of fluid recirculation as reported by Scheid et al. [47]. A study of the velocity profiles at various points within the leading wave disturbance to the first



(a) $\mathrm{Re}^* = 2$

(b) $\mathrm{Re}^* = 2.9$

(c) $\mathrm{Re}^* = 3.8$

(d) $\mathrm{Re}^* = 5$

Figure 96.: Solitary wave structures for increasing Reynolds number.

peak of the first capillary wave are reconstructed. Taking a quadratic profile for streamwise flow velocity of the form in (5.0.4), with $a_0, \ldots, a_2$ as in (5.0.6), gives explicitly the expression

$$u = \frac{3q}{h^2}y - \frac{3q}{2h^3}y^2. \tag{5.2.1}$$

From (5.4.2), an expression for flow velocity perpendicular to the plane is derived, e.g. see Equations (3.3.2)-(3.3.5), and the subsequent velocity profiles shown in Figure 97 are recreated. All profiles are nonlinear, with the lowest point in the wave structure having the numerically determined analytical profile

$$u = 1.42y - 0.81y^2. \tag{5.2.2}$$

Figure 99 shows calculated velocity profiles for increased Reynolds number $\mathrm{Re}^* = 5$. The lowest point on the wave structure again corresponds

to the profile marked (i), which depicts an almost stagnant region, with the magnitudes of the fluid velocities close to zero. To assess the necessity of a higher order polynomial approximation for the streamwise velocity profile, we carry out the process above with the cubic profile $u = b_0 + b_1 y + b_2 y^2 + b_3 y^3$, with $b_0, \ldots, b_3$ as in (5.0.12). Figure 98 shows the profiles for a solitary wave when $\mathrm{Re}^* = 2$ and Figure 100 for $\mathrm{Re}^* = 5$.

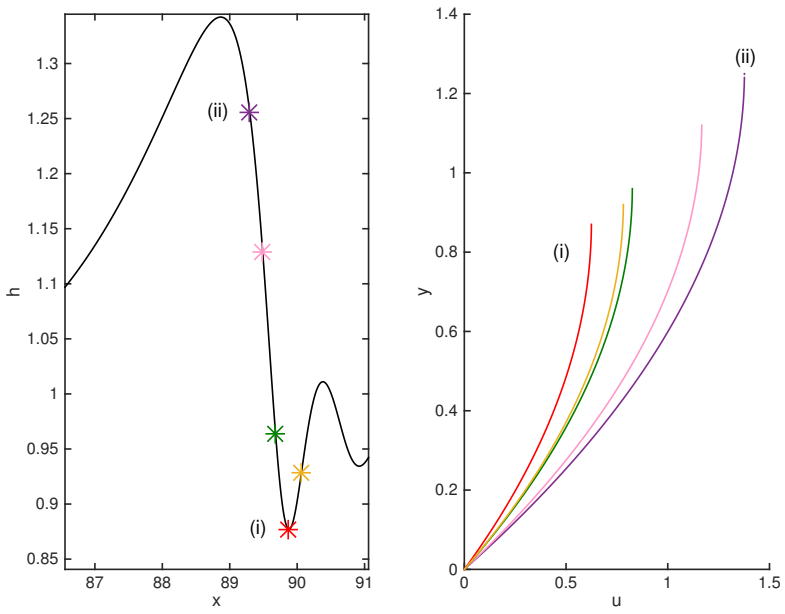


Figure 97.: Quadratic velocity profiles at various cross-sections. $\mathrm{Re}^* = 2$, $\theta = 6.4$.

When using the value of the Reynolds number $\mathrm{Re}^* = 2.9$ from experiments of Liu and Gollub [29], the quadratic velocity profile streamlines are obtained in Figure 101.Streamlines are relative to a moving frame of reference, with disturbances visible in the capillary region.

For near-horizontal flow, $\theta = 6.4$, similarly-shaped velocity profiles are observed on comparing quadratic against cubic polynomial assumptions. The effect of increasing the Reynolds number is seen in figures 99 and 100 for the quadratic and cubic respectively; the profiles marked (i) depict regions with very low fluid velocities. To investigate this region further, the angle of inclination of the plane is increased to $\theta = 90$, simulating vertical falling

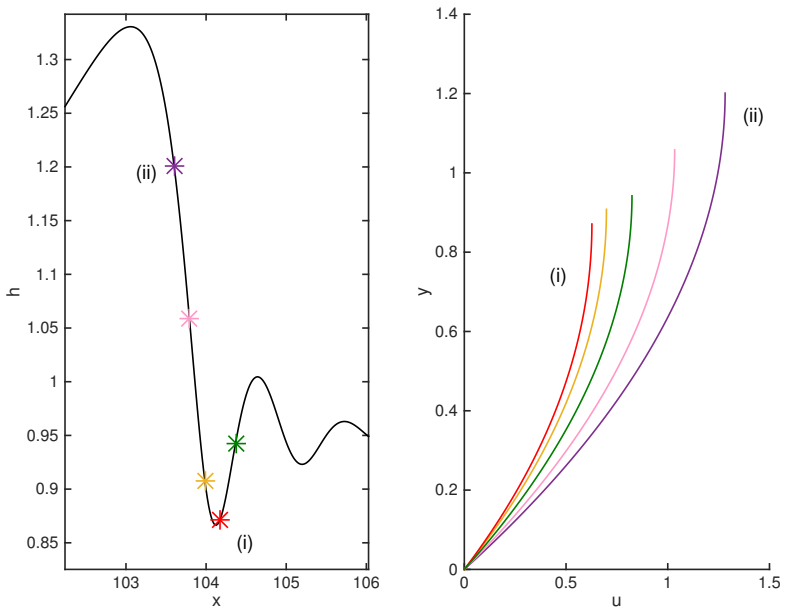


Figure 98.: Cubic velocity profiles at various cross-sections. $\mathrm{Re}^* = 2$, $\theta = 6.4$.

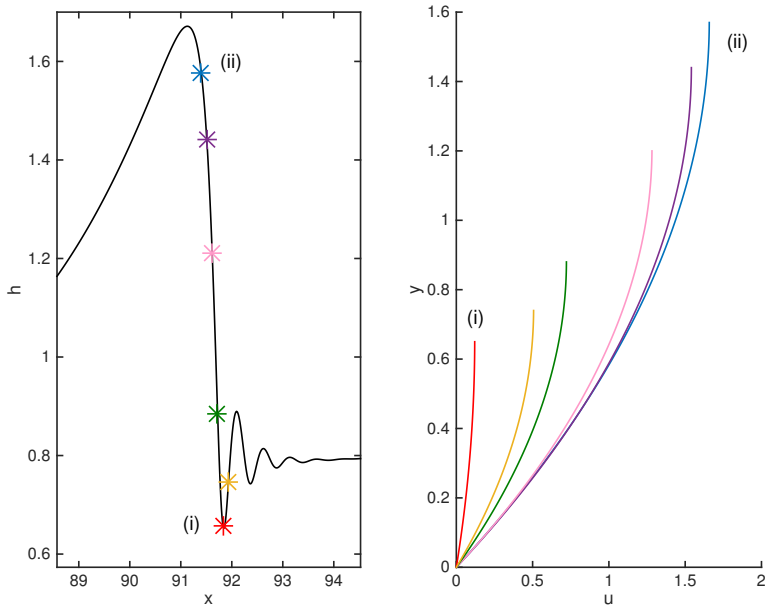


Figure 99.: Quadratic velocity profiles at various cross-sections. $\mathrm{Re}^* = 5$, $\theta = 6.4$.

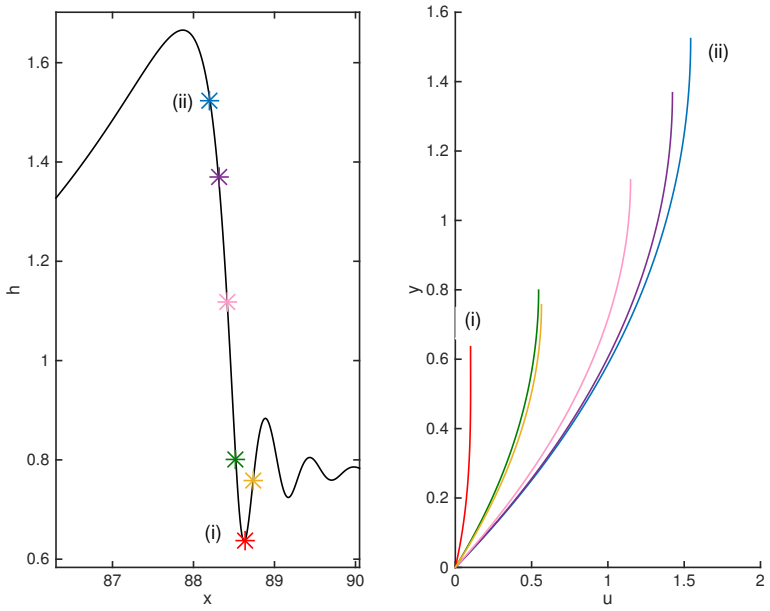


Figure 100.: Cubic velocity profiles at various cross-sections. $\mathrm{Re}^* = 5$, $\theta = 6.4$.

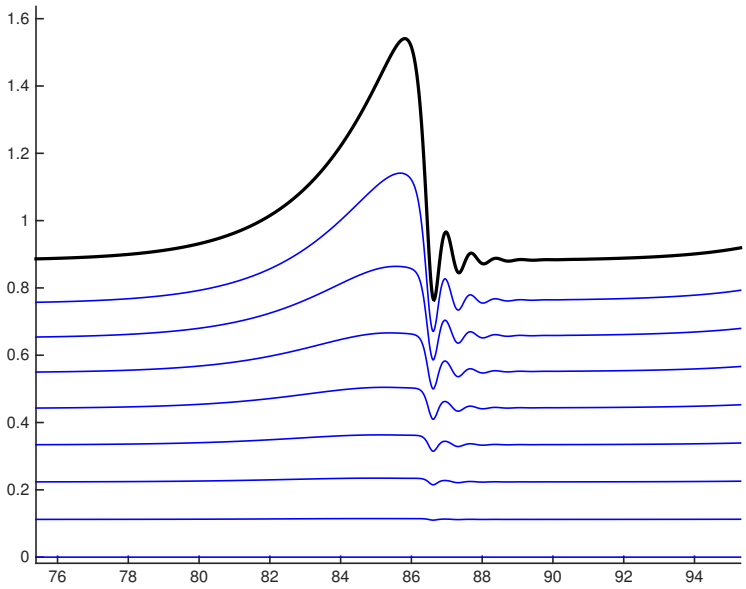


Figure 101.: Streamlines in moving frame of reference.

film; for comparison see Chang et al. [8] amongst others. Increasing the inclination has the effect of further increasing the height of the main wave

disturbance to $h_{\max} = 2.1$, as seen in Figure 102. The maximum amplitude of the capillary region, at $\mathrm{Re}^* = 5$ and $\theta = 90$, is 0.3559 and the wavelength of the first capillary wave is 0.31. This represents a 50% increase in amplitude and a 40% decrease in wavelength when compared to the equivalent profile at $\theta = 6.4$ in Figure 96d.

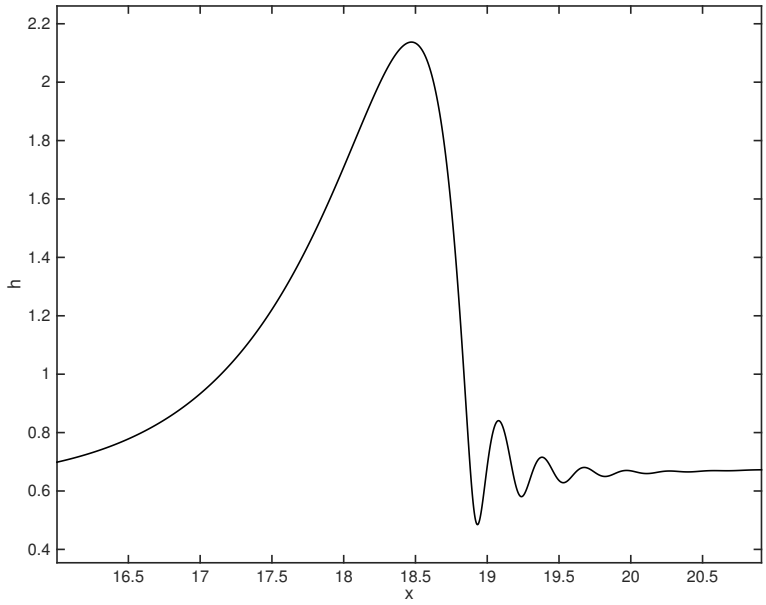


Figure 102.: Solitary wave and capillary region. $\mathrm{Re}^* = 5$, $\theta = 90$.

Recreating both quadratic and cubic velocity profiles for their respective solutions at $\theta = 90$, a significant difference is seen in the velocity profiles corresponding to the point of minimum thickness in the solitary wave. This is shown by the quadratic profile (i) in Figure 103, and the cubic profile (i) in Figure 104. Besides, the cubic profile shows more negative fluid velocities and has a non-parabolic shape.

Results suggest that the cubic polynomial better captures the flow pattern within the capillary region; velocity vectors are plotted at grid points created in this region. In Figure 105, a clearly defined pattern depicts fluid particles on one side of the capillary ripple recirculating to the opposite side of the trough. This results in the front moving in the downstream direction.

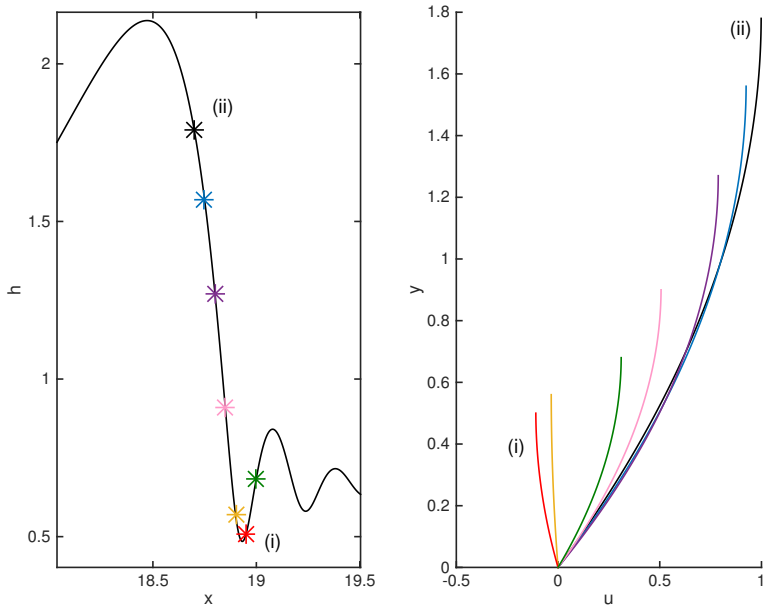


Figure 103.: Quadratic velocity profiles at various cross-sections. $\mathrm{Re}^* = 5$, $\theta = 90$.

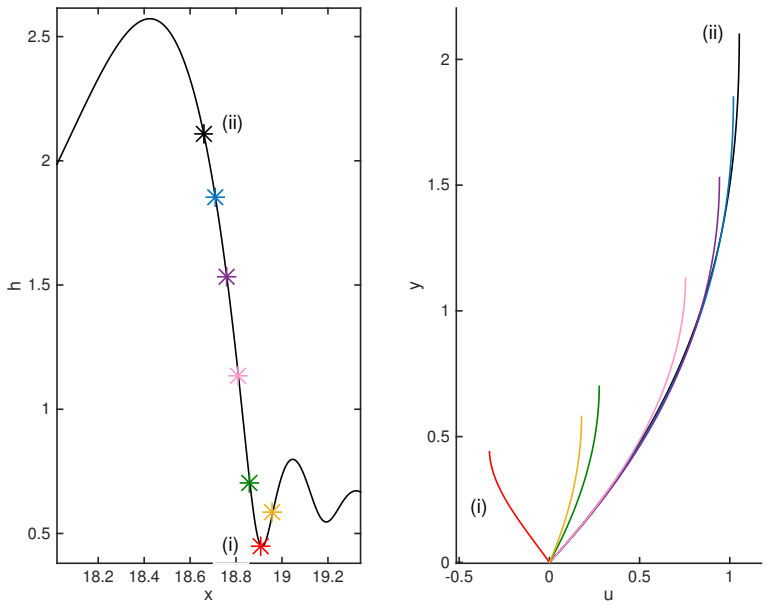


Figure 104.: Cubic velocity profiles at various cross-sections. $\mathrm{Re}^* = 5$, $\theta = 90$.

The recirculation region also shows within the preceding capillary wave, although with velocities much smaller in magnitude.

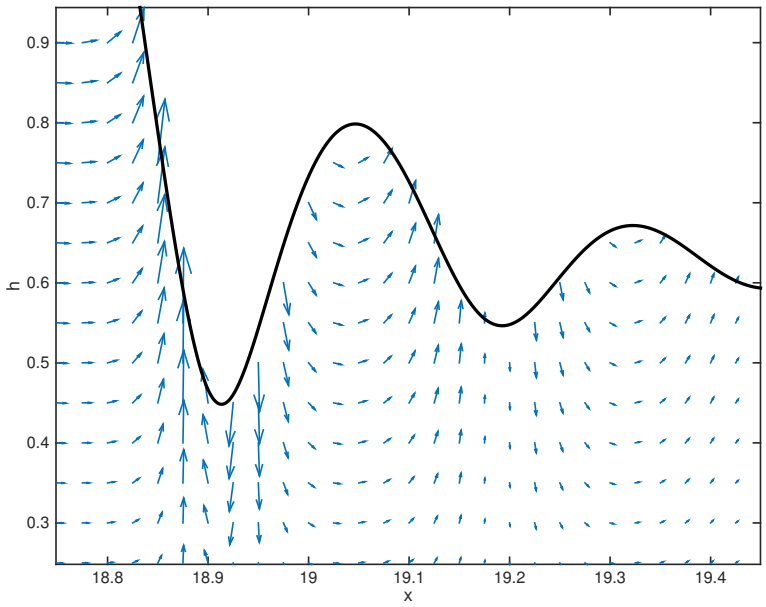


Figure 105.: Cubic velocity field in the capillary region showing recirculation. $\mathrm{Re}^* = 5$, $\theta = 90$

5.3 STABILITY CHARACTERISTICS OF SOLITARY WAVES

In this section the stability of inlet pulses is now considered. A noted criticism of the depth-averaged Shkadov model for thin-film flow is the accuracy with which the quadratic model predicts the onset of stability. Higher than actual Reynolds numbers appear as stable in a numerical simulation, whereas experimentally, perturbations grow into solitary waves, i.e. the stability threshold is believed to be overpredicted by the Shkadov model. A general cubic model has been developed within Section 3.4 as an alternative to the initial model assuming a quadratic velocity profile, and within the current chapter both have been adapted to simulate gravity-driven flow

on an inclined plane - flow in which perturbations have the potential to form into a series of solitary waves.

The perturbations are initiated at the inlet boundary at $x = 0$ using a sinusoidal boundary condition of the form in (5.0.19). Within this function, the frequency, f, is known to affect the stability of system, as is the Reynolds number and so these two parameters are varied. The values of the other parameters are kept at

$$\theta = 6.4, \quad \lambda = 16.41132 \quad \text{and} \quad \text{Ca} = 1.56184 \times 10^{-2}. \tag{5.3.1}$$

Figure 106 illustrates a range of near-horizontal profiles varying in Reynolds number and frequency. It can be seen from comparing figures 106a and 106b that increased inlet frequency has the effect of inducing stability. It is observed that with a frequency of $f = 0.2$, that the perturbations initially decay to an amplitude of 0.1 and remain at that height, whereas when $f = 0.3$, the perturbations decay exponentially back to the resting height of $h = 1$. The effect of increasing the Reynolds number can be deduced by comparing figures 106b and 106c, which share the same frequency $f = 0.3$. Stability is observed for $\text{Re}^* = 2$, with a reduced Reynolds number of $\text{Re}^* = 3$ destabilising the solution so that perturbations remain at an amplitude of 0.2. Subsequently the instability of the leading front causes it to increase in height, which then happens to the subsequent waves.

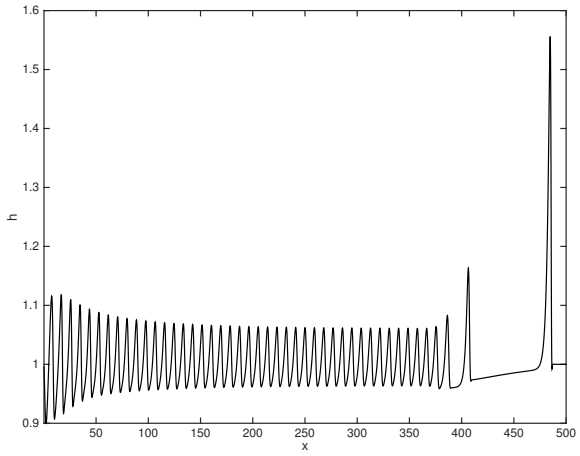
It is observed from the comparison of figures 106b and 106c that, for a frequency of $f = 0.3$, there is some critical Reynolds number R_c which dictates the stability of the system. In an endeavour to locate this critical Reynolds number for a range of frequencies, the Reynolds number and the inlet frequency are varied parametrically to create stability diagrams for both the quadratic and cubic numerical models.

As can be seen in Figure 107, there is close agreement between the two models when considering the shape of the stability curve, with both taking approximately the same characteristics for equivalent Re^* and f. The cubic model predicts onset of instability, as $f \to 0$, at a slightly lower reduced

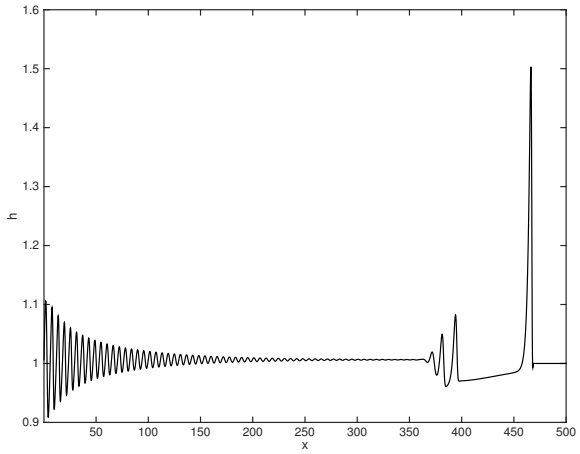
Reynolds number than the quadratic approximation model but no significant change from the quadratic depth-averaged model is observed. Data taken from a study by Ruyer-Quil et al. [40] suggests that the true critical Reynolds number for an almost zero inlet frequency, as calculated through experimental data, is approximately 20% lower than that predicted by the Shkadov model, which typically uses a quadratic approximation of the velocity profile. The cubic model is shown to be insufficient to improve upon the quadratic in the area of stability.

On inducing the wave structures, two different methods of initiation have been used:
(i) pulsing the inlet height once then holding for a fixed time interval before repeating, as illustrated in Figure 90;
(ii) the constant sinusoidal motion of inlet boundary which then evolves into the solitary waves.

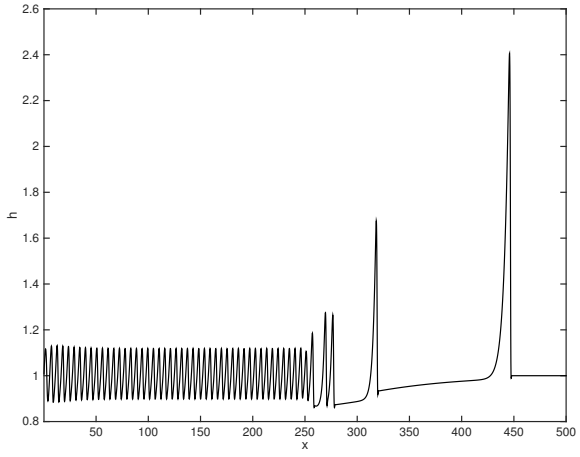
Another method of inducing solitary waves, utilised by Chang et al. [10], is to create white noise at the boundary which the propagates downstream and becomes the solitary waves we are attempting to recreate. This is observed in profiles where the inlet frequency is high enough for the perturbations to decay to what can be considered numerical noise. Further downstream, interactions on a much smaller lengthscale create solitary waves which are observed growing in amplitude. Figure 108 shows the initial perturbations decay to the resting height of $h = 1$. Numerical noise is present at a very much smaller amplitude and this leads to the evolution of solitary waves, similary to the solitary wave induction technique used by Chang et al. [10]. The leading front is significantly larger, due to the lack of stabilisation downstream whilst subsequent solitary waves settle at a height of $h = 1.1$.



(a) Unstable: $\mathrm{Re}^* = 2$, $f = 0.2$



(b) Stable: $\mathrm{Re}^* = 2$, $f = 0.3$



(c) Unstable: $\mathrm{Re}^* = 3$, $f = 0.3$

Figure 106.: Effect of increasing frequency and Reynolds number on stability.

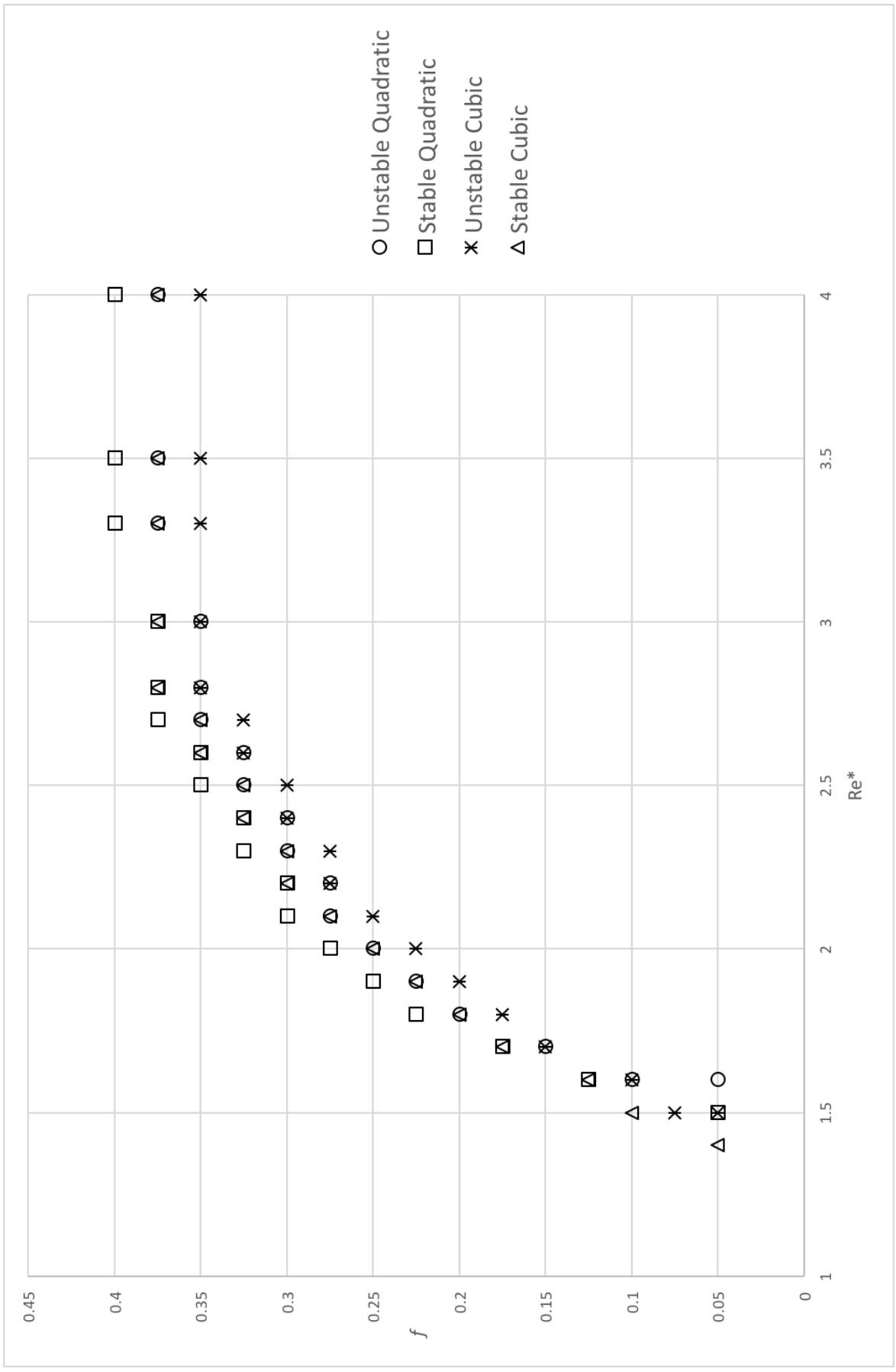
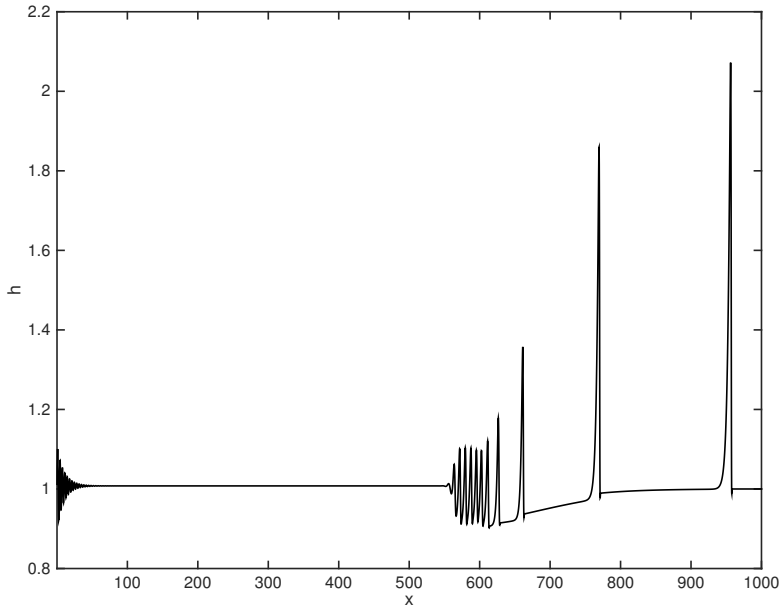
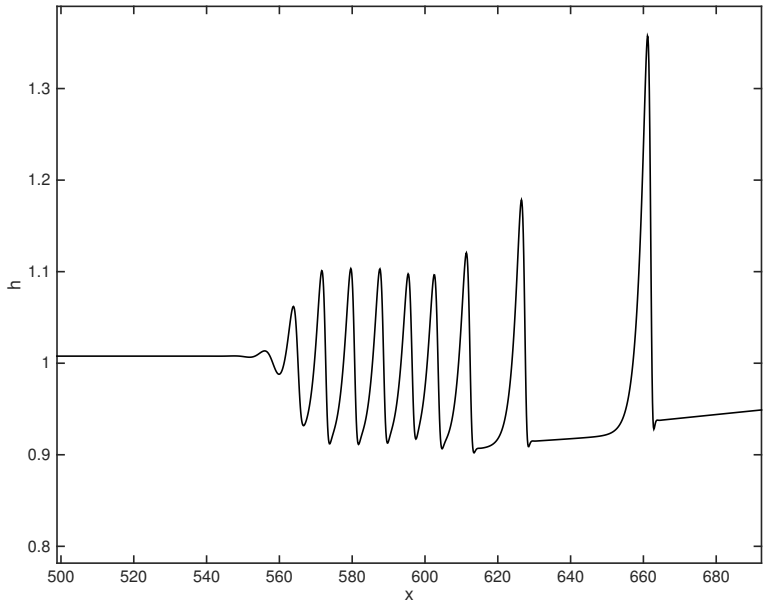


Figure 107.: Stability curves comparing Reynolds number and frequency for quadratic and cubic depth-averaged models.



(a) Overall profile



(b) Expanded view of solitary waves

Figure 108.: Decay of perturbations to numerical noise, which then evolves into a set of solitary waves. $\mathrm{Re}^* = 2.4$, $f = 0.5$.

5.4 SHEAR-IMPOSED SOLITARY WAVES

The stability of solitary waves with imposed surface shear is now investigated. Recent work by Samanta et al. [43] also looks at the effects of constant shear on solitary waves, up to moderate Reynolds numbers. The formulation given in Equations (5.0.1)-(5.0.17) is modified to include a surface shear parameter τ. This follows from the models in Chapter 3, but within a stationary frame of reference rather than moving with the wave structures. The no-slip boundary condition is imposed as in (5.0.1), but the boundary condition on the free surface becomes

$$\frac{\partial u}{\partial y} = \tau \quad \text{on} \quad y = h. \tag{5.4.1}$$

Again using the definition of flux $q = \int_0^h u \, \mathrm{d}y$ and a quadratic approximation for the velocity profile $u = a_0 + a_1 y + a_2 y^2$, the profile coefficients a_0, a_1 and a_2 are now subject to the constraints

$$\begin{aligned} &a_1 + 2a_2 h = \tau, \\ &a_0 = 0, \\ &a_0 h + a_1 \frac{h^2}{2} + a_2 \frac{h^3}{3} = q. \end{aligned} \tag{5.4.2}$$

The solution of (5.4.2) gives

$$\begin{aligned} a_0 &= 0, \\ a_1 &= -\frac{h^2\tau - 6q}{2h^2}, \\ a_2 &= \frac{3(h^2\tau - 2q)}{4h^3} \end{aligned} \tag{5.4.3}$$

to be inserted into the velocity profile, which is then used to find analytical expressions for the integral coefficients I_h and I_q as

$$\begin{aligned} I_h &= \frac{h^4\tau^2 + 2h^2 q\tau - 48q^2}{40h^2}, \\ I_q &= \frac{h^2\tau + 48q}{20h}. \end{aligned} \tag{5.4.4}$$

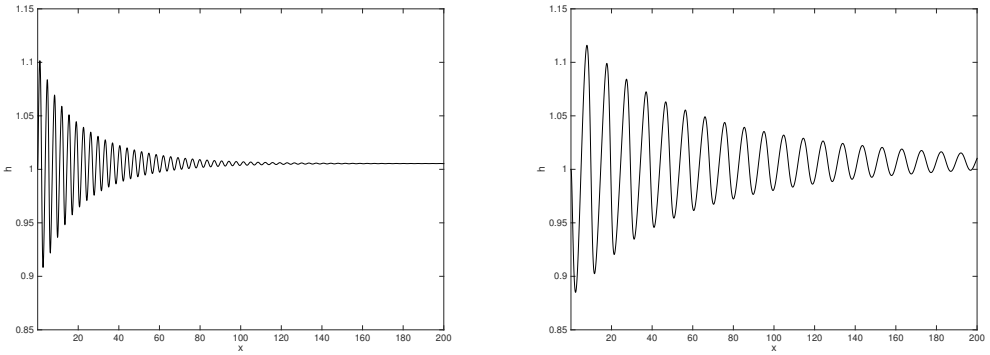
The momentum equation, with the revised velocity profile and integral coefficients, is now

$$\mathrm{Re}^* \left(\frac{\partial q}{\partial t} + I_h \frac{\partial h}{\partial x} + I_q \frac{\partial q}{\partial x} \right) = \lambda h \sin\theta + \tau + \frac{h^2\tau - 6q}{2h^2} - \varepsilon\lambda h \frac{\partial h}{\partial x}\cos\theta + \frac{\varepsilon^3}{\mathrm{Ca}} h \frac{\partial^3 h}{\partial x^3}, \tag{5.4.5}$$

The continuity equation and boundary conditions remain as in (5.0.17)-(5.0.19). The inlet flux, again derived from imposing steady, uniform flow on the momentum equation, is

$$q_l = \frac{1}{3}h_l^3 \lambda \sin\theta + \frac{1}{2}\tau h_l^2. \tag{5.4.6}$$

As in the previous section, the inlet frequency f and the film Reynolds number Re^* are varied to affect the stability of perturbations on the inlet. Additionally, the effect of shear on the system is investigated by imposing both positive and negative values of τ. Firstly the ability of positive shear to destabilise an initially stable set of perturbations is assessed. That is, at $\tau = 0$, the profile in Figure 109a is observed where sinusoidal perturbations at the inlet decay to the resting frequency. Comparatively, the perturbations in Figure 109b, besides having a longer wavelength, have a greatly reduced rate of decay due to the shear $\tau = 3$ applied in the downstream direction attempting to destabilise the solution.



(a) $\tau = 0$ (b) $\tau = 3$

Figure 109.: Decreased rate of decay of perturbations with shear applied in the downstream direction.

In order to better evaluate the effect of shear on the perturbations introduced at the inlet, the value of τ is increased incrementally from $\tau = 0$ and the maximum amplitude of the resulting solitary wave profiles is noted. This is done via the Matlab function *findpeaks*, which returns the values of the local maxima, along with the locations at which they occur. Using *findpeaks*, the plot in Figure 110 was produced, which shows the perturbations decaying less rapidly with increasing positive shear. Samanta et al. [43] note that the transition process of inlet perturbations into solitary waves becomes faster when shear is applied in the downstream direction. This corresponds to a positive surface shear parameter as illustrated in figures 109-110.

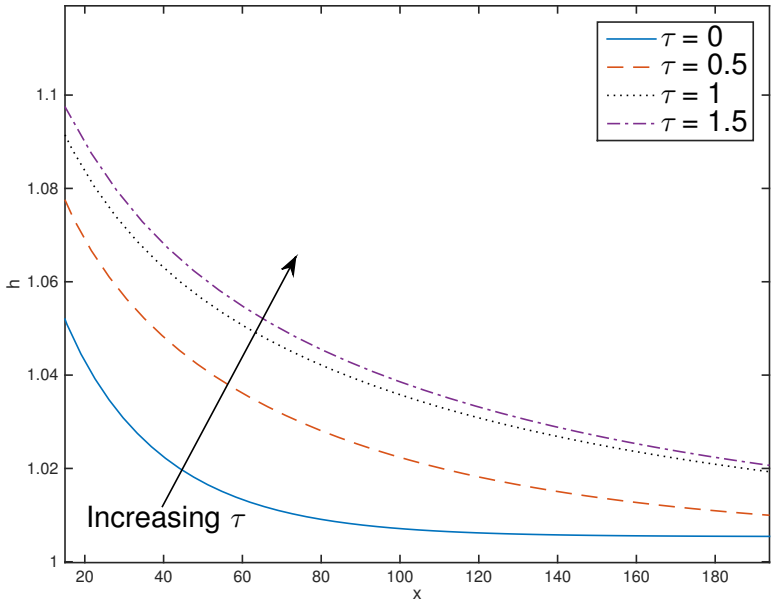
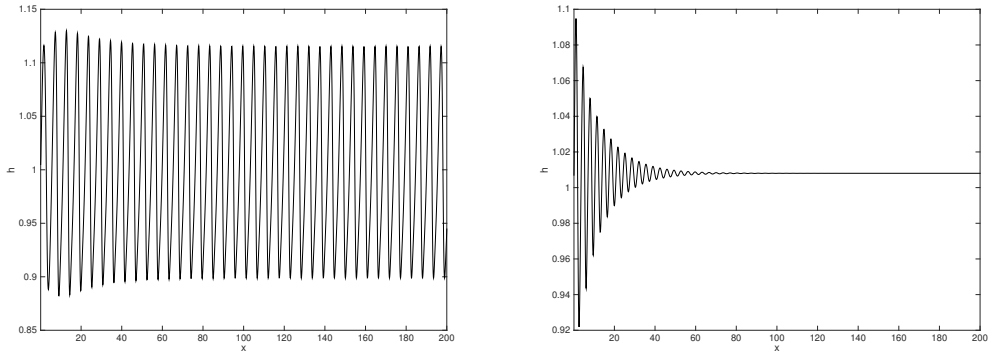


Figure 110.: Plot of local maxima for increasing τ.

The converse is now investigated, where an initially unstable set of perturbations are stabilised by the inclusion of surface shear. This time τ is negative, acting in the upstream direction, opposing gravity. In Figure 111a an unstable profile is observed when there is no surface shear acting. By imposing $\tau = -0.8$, the perturbations now decay to the resting height $h = 1$, as was the effect of increasing the inlet frequency in figures 106a-106b. Thus, shear in the opposing gravity is seen to be a stabilising factor in the evolu-



(a) $\tau = 0$ (b) $\tau = -0.8$

Figure 111.: Stabilisation of perturbations with shear applied in the upstream direction.

tion of solitary waves. This can be seen in Figure 112, which shows a plot of the local maxima at various values of $\tau \leq 0$. This is also consistent with work by Samanta et al. [43], in which negative shear is noted to turn solitary waves into sinusoidal motion similar to that at the inlet boundary.

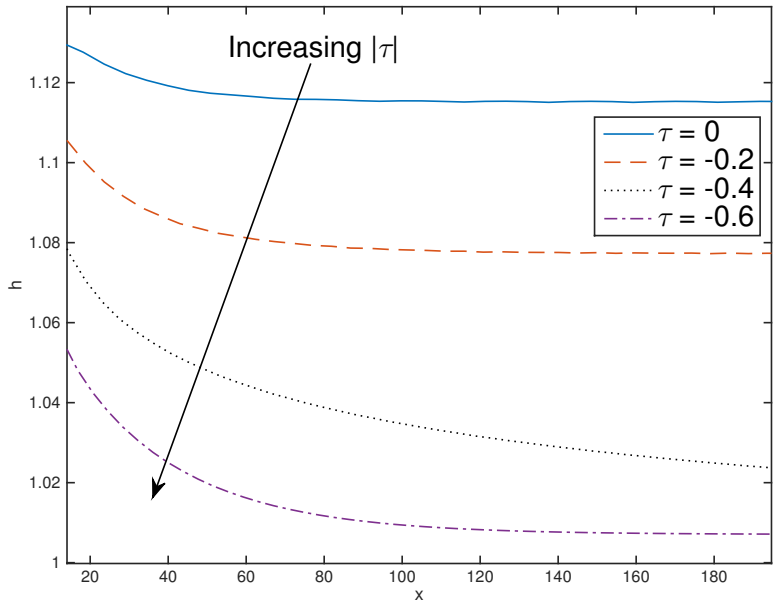
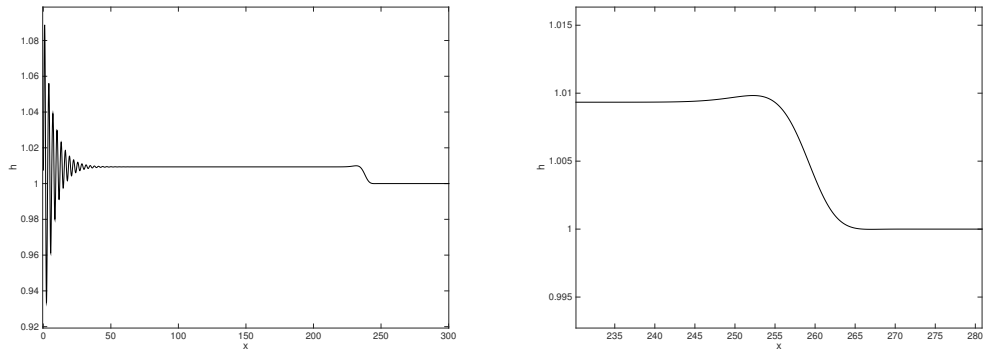


Figure 112.: Plot of local maxima for increasing $|\tau|$.

An interesting effect is observed when the value of shear is decreased further i.e. increased magnitude of shear in the negative direction. As before, the initial perturbations are stabilised by surface shear opposing the effects of gravity. However, an initial front, created by the displacement of mass when the perturbations are forced at the inlet, travels along the domain and retains its shape, as in Figure 113. When perturbations are introduced either side of the shock and the direction of decay is observed, this is classified as a downstream-travelling undercompressive wave. Further investigation to



(a) Overall profile (b) Expanded view of standing wave

Figure 113.: Moving front travelling downstream. $\tau = -1$, $\mathrm{Re}^* = 3$.

validate the formation of the moving wave profile was carried out by confirming that the height of the film on either side of the wave front, when substituted into the cubic expression

$$q = \frac{\lambda h^3}{3} \sin\theta + \frac{\tau h^2}{2}, \tag{5.4.7}$$

yields a value for film flux which matches that observed during the solution of the equation. Parameters $\lambda = 16.4113$ and $\theta = 6.4$ are chosen as in (5.3.1), with $\tau = -1$. The height of the film to the left of the wave front is $h^- = 1.009$, giving a film flux of $q^- = 0.1176$, and the film depth to the right of the front is $h^+ = 1$, corresponding to $q^+ = 0.1098$. Additionally, the speed of the propagation of the front is calculated by averaging across the position of a marker in the x-direction at several time intervals, giving the

dimensionless Lax speed calculated from the numerical solution as $S \approx 0.85$, also corresponding to the analytical expression in (1.2.5).

5.5 OVERVIEW OF THE CHAPTER

A mechanism for initiating solitary waves, as well as their structures and stability has been evaluated in this chapter. Analysis is based on the depth-averaged thin-film model developed in Chapter 2. Validation of results has been sought through mesh density checks, as well as comparison to experimental data produced by Liu and Gollub [29]. Modelling included a study of the evolution of variations in the amplitude of the inlet perturbations and the subsequent development of solitary waves. All validation suggested that this model was robust and solutions obtained are consistent with reported physical features.

This study includes the effect of inertia on a solitary wave structure. The film Reynolds number was found to have a direct effect on the height of the primary peak within the structure, as well as the amplitude and wavelength of the capillary waves at its base. This, physically, is presumed a result of fluid particles exhibiting a tendency to travel upwards within the primary peak of the solitary wave structure with increased inertia, causing it to attain a larger maximum height. Corresponding, as has been observed in earlier chapters, the larger hydraulic jump causes the capillary region to exhibit alrger amplitudes and shorter wavelengths. A consequence of increasing inertia within the model is to modify the flow dynamics within the capillary region. Both quadratic and cubic velocity profiles were reconstructed and the flow patterns analysed. At increased Reynolds numbers, the flow is near stagnant in the vicinity of the shallowest point of the wave structure. Illustrative examples are given in figures 97-100, which were profiles calculated at the near-horizontal angle of inclination $\theta = 6.4$. Increasing the angle of inclination showed the possibility of recirculation in the capillary region. Vertical falling film profiles were calculated, subsequently recreating both

quadratic and cubic velocity profiles in the capillary region. Recirculation regions were observed, corresponding to backflow in the capillary region as mentioned by Dietze et al. [15]. The recirculation occurred at the shallowest point of the profile and a significant difference between the quadratic and cubic velocity profile noted; the cubic approximation was able to resolve the recirculation in greater detail. Evaluation of the velocity field in the capillary region, illustrated in Figure 105, provided an aid to visualising the recirculating flow.

Further investigations were carried out to evaluate the stability of the inlet perturbations. A criticism of the existing Shkadov model, particularly when assuming a quadratic velocity profile, is its failure to correctly predict the onset of instability. Of interest is whether the cubic approximation developed is an improvement upon the quadratic model. A model comparison provides the stability curves in Figure 107 for both variations of the depth-averaged model. It is noted there is much overlap of the two stability curves, with the cubic not providing any significant advances to the stability characteristics over the quadratic depth-averaged model. One potential area in which the cubic model does improve understanding over the quadratic velocity profile is in the reconstruction of the flow dynamics in the capillary region. This is amplified for the vertical falling film behaviour shown in figures 103 and 104. The cubic velocity profile identifies slight deviation from the quadratic profile, with larger negative fluid velocities being observed. This is highlighted in the velocity vector map in Figure 105 which gives a better resolution of the backflow and recirculation properties within the capillary region of a solitary wave.

A final part of this chapter studies the effect of imposing surface shear on solitary waves and in particular on their stability. Results identify that positive shear has the effect of reducing the stability. Negative shear however, i.e. opposing gravity, stabilises what were initially unstable perturbations. When increasing the value of shear in the negative direction, the perturbations are seen to decay, but a downstream travelling front, similar to those

observed in Chapter 3, is formed. The shape of this front stays constant as viewed in the stationary frame of reference, classifying it as a standing wave structure formed as a balance between gravitational forces and the shearing airflow opposing gravity.

6

THESIS SUMMARY, CONCLUSIONS AND FUTURE WORK

Thin-film flow models are extensively used in modelling flows in industrial contexts. In many instances models are developed associated with Stokes flow ($\mathrm{Re} = 0$) or low Reynolds number flows, to identify characteristic film flow behaviour and potential wave structures. The development of newer industrial technologies may require the film flow to be associated with an increased Reynolds number. An extended formulation is provided in Chapter 2 for thin-film flow corresponding to moderate Reynolds number associated with highly sheared flows. Within this chapter the formulation allows the streamwise velocity profile to be represented by either a quadratic or cubic polynomial approximation. Model formulation uses a Kármán-Polhausen depth-averaging approach [23]; similar to a Shkadov model approach. Models importantly incorporate surface tension, inertial effects and gravity. In a study of flow with a balance of gravity and surface shear acting on the fluid, combinations of two or more uniform flow solutions for thin film flows on an inclined plane known as the Nusselt heights are derived [49]. For non-uniform flows and moderate Reynolds number, typically including wave motions, numerical solutions are obtained implicitly in the time variable, using a finite-difference spatial scheme with suitable upwinding applied.

Chapter 3 evaluates the effect of increasing Reynolds number on existing film solutions, potential new wave structures and the influence of capillary ripples. Initially a quadratic form of the streamwise velocity profile was assumed in Section 3.1 and the corresponding film profile solutions are

given in Section 3.3. Characteristic wave solutions for increasing Reynolds number were sought corresponding to shock structures linking conjugate heights at moderate angles of plane inclination. Initial numerical simulations were carried out neglecting inertial effects. This allowed effective comparison against pre-existing Stokes flow solutions. Detailed numerical calculations were carried out for increasing film inertia to moderate values characteristic of flows in aeroengine applications. Smoothing effects of inertia were observed in many instances, but with the capillary region exhibiting larger amplitude waves at higher Reynolds numbers. The smoothing is an expected consequence of introducing inertia into the model equations. The fluid within bore in the larger section the wave structure is more inclined to move in a smoother path with increasing inertia. This is illustrated when comparing Figures 20 and 21. A physical explanation for the behaviour of the capillary region at larger film Reynolds numbers is the inertial effect of the mass of fluid travelling up the plane, with an increased reluctance to change direction, and so the capillary region becomes more severe. Increasing surface shear was shown to decrease the amplitude of the capillary ripples, whilst increasing their wavelength. This was a consequence of the difference in the Nusselt heights h_1 and h_2 becoming smaller with increasing surface shear, as can be seen in Figure 10. A smaller hydraulic jump for the fluid to overcome means there is less cumulative effect at the base of the main wave structure and hence a less severe capillary region. Other initial profiles exhibited a new class of solutions where there was a new tier development at heights not part of the set of the classical Nusselt film heights. Perturbations were artificially introduced into the evolved film profiles and their propagation properties studied. This allows the classification of wave structures as compressive, undercompressive or rarefaction waves, or their reverse-facing equivalents. Solutions were also investigated at near-vertical angles of inclination and comparisons drawn between the two sets of film profiles. Some of the features observed under a Stokes flow assumption are eliminated when increasing the film Reynolds number. An inference is that

that the inclusion of inertia can have a significant effect on the evolution of the high-speed film profiles through the level of detail obtained within the capillary region as well as the formation of new wave features, and is a relevant improvement upon previous Stokes flow models. Many other wave profiles exhibited the more typical smoothing effects of increased inertia; such profiles obtained at the moderate and high angles of plane inclination were found to be comparable. An important outcome of the numerical simulation of various wave profiles, both at lower and higher angles of inclination, is the evolution of tiers at heights consistent across various initial conditions. The height of the tiers was consistent across the different forms of initial profile used, and ultimately indicated that the boundary conditions were the driving factor. Initial profiles with identical boundary conditions were found to develop into similarly structured waves, providing credible evidence that these waves structures are physically representative of the model.

Capillary ripples forming at the base of the leading wave front are extensively reported in previous literature and can be modelled within the Shkadov integral boundary layer model [23]. Potential exaggeration of the amplitude of these ripples is a known problem of the Shkadov model [51], possibly as a result of assuming a low-order velocity profile. In Section 3.4, the mathematical formulation is extended to include a cubic approximation of the velocity profile to better capture the flow characteristics, especially in regions of fluid recirculation. The evolution of shear-driven films with similarly structured initial profiles as those in Section 3.3 is also investigated. Analysis of the capillary region revealed no significant changes in structure, with only a marginal increase in the amplitude of the first capillary ripple when using a cubic velocity profile approximation. Streamlines and the velocity profiles at various points within a compressive standing wave structure were recreated and compared with those obtained when assuming a quadratic velocity profile. Equivalent velocity profiles were observed and the effects of including inertia within the governing equations were com-

parable. These indicate that at moderate angles of inclination, a quadratic velocity profile is sufficient to model shear-driven flow. The film Reynolds number was subsequently increased for the same compressive wave structure and the velocity profiles within the leading wave front and capillary region were also recreated. A feature included a recirculation region observed at the base of the primary peak of the wave structure, located at the shallowest point within the profile. Here, some fluid particles near the fluid-plane boundary travel with streamwise velocity more negative than the reference wall velocity. Other fluid particles towards the free surface were found to be travelling with a velocity more positive than the wall velocity. Translation into a stationary frame of reference identified some regions in which fluid particles are travelling in the upstream direction, and other regions where particles are moving in the downstream direction. Further investigations into the recirculation regions were carried out by again increasing the slope inclination from the moderate angle previously considered to a near-vertical angle. Again, reconstruction of the velocity profiles highlights fluid recirculation at the shallowest point of the film profile, between the primary peak and the first capillary ripple, but similar profiles are observed for both the quadratic and the cubic cases. The velocity profiles for the flow in the remainder of the wave structure, irrespective of whether the film Reynolds number is $\mathrm{Re}^* = 10$ or $\mathrm{Re}^* = 20$, or whether plane inclination $\theta = -45$ or $\theta = -80$, showed linear characteristics, with terms of quadratic or cubic order being comparatively small. Overall results using the cubic velocity profile for the wave structures investigated in detail within this chapter showed strong similarities with the quadratic profile assumed to obtain the results in Section 3.3.

The effects of introducing a slip boundary condition between the fluid and the plane is investigated in Chapter 4. The Nusselt heights which are solutions to a cubic equation involving a prescribed flux flowing through the system within a moving frame of reference were calculated for increasing slip length. At smaller values of slip length, solutions were observed

exhibiting similar wave features to those in Chapter 3 which were calculated assuming no slip at the fluid-plane boundary. Of note is the increase in wavelength and reduced amplitude (i.e. reduced overall severity) of the capillary region as a result of introducing a positive slip length into the formulation. As in Chapter 3, this is a consequence of the reduced magnitude of the hydraulic jump between h_1 and h_2 with increasing slip length. Two of the Nusselt heights are eliminated as solutions for a prescribed flux when increasing the slip length beyond a critical value, leaving one potential height for uniform flow. Applying this single Nusselt height as one of the boundary conditions, the height of the other boundary is varied and the evolution of film profiles unique to individual boundary conditions is observed. The inclusion of inertia in the solution of these film profiles was shown to have a significant effect, with two-tier profiles at a film Reynolds number $\mathrm{Re}^* = 0$, exhibiting three-tier characteristics when $\mathrm{Re}^* > 0$. To evaluate the detailed flow dynamics within the film further, streamlines plots and velocity profiles were reconstructed at various cross-sections within the flow. These give new insight to the evolution of wave structures including regions of recirculation; these were present, both in the non-inertial and the inertial cases.

Solitary wave motion on an inclined plane was investigated in Chapter 5, with forced periodic perturbations at the inlet evolving into repeating wave structures dependent on the value of the Reynolds number as well as the inlet frequency. Initial calculations are made at comparable parameter values to experimental data for validation, with both quadratic and cubic velocity profiles considered. The effects of increasing film Reynolds number on the solitary wave structures were analysed. It was found that increasing Reynolds number increases the height of the main solitary wave, as well as increasing prominence and amplitude of the capillary region. The increased height of the capillary wave, as discussed in more detail in Chapter 5, is inferred to be a result of the flow's increasing reluctance to change direction, as is expected with increasing inertia (see Figure 101). Within

this section velocity profiles were calculated from within the solitary wave for both quadratic and cubic profiles. In common with Chapter 3, there was strong similarity between the two models at all film Reynolds numbers for which solutions were obtained. Following this, stability characteristics of solitary waves were investigated; an increase in inlet frequency was shown to have a stabilising effect, whilst an increase in film Reynolds number destabilises perturbations. Stability curves are drawn for both quadratic and cubic models. A detailed comparison suggests that the cubic model has a similar critical Reynolds number to the quadratic model and does not address the concern of the quadratic model of overpredicting the threshold of instability. Investigation of vertically-falling solitary waves, revealed that at higher angles of inclination, the cubic velocity profiles deviate much more significantly from the quadratic profile than previously observed. Stronger fluid recirculation exists in the capillary region from using a cubic velocity profile. It is here, where the film depth is shallowest, that it is advantageous to use a higher order flow velocity approximation as a greater knowledge of the flow dynamics could influence the choice of model for simulation of engineering applications. In the majority of the remainder of the flow, strong similarities exist. A final section of this chapter investigates the effect of surface shear on solitary wave stability. It was found that with increasing shear in the positive direction, an initially stable set of perturbations becomes less stable; wave disturbances took longer to decay to the resting height. Applying an increasing magnitude of surface shear in the negative direction is shown to have a stabilising effect. On increasing the magnitude of the negative shear further, we observe a standing wave structure travelling along the plane, similar to those found in Chapter 3.

Numerically, there have been significant challenges to be overcome to produce the film profiles and solutions presented in this thesis. Notably, the capillary region has proved significant in dictating the mesh density requirements. The governing equations used a finite difference approximations on a uniformly spaces grid. The wavelength of the capillary ripples has been

substantially smaller than that of the larger wave structures and has led to the requirement for a large number of solution nodes. An area of future development of the research in this thesis might be to simulate flow on a three-dimensional surface. In the context of an aeroengine bearing chamber, axial film flow disturbances may be present with the added momentum of droplets as they impact upon the film. Mathematical model formulation in a three-dimensional context will further the understanding of thin-film flows and wave structures, with potential for finger and ridge formation, as observed in some experimental work [52]. The Kármán-Polhausen depth-averaging method with the adoption of a quadratic velocity profile has proved sufficiently accurate in the majority of cases investigated within this study. The finite difference numerical approach may need to be revised for numerical simulation of three-dimensional flow as the computational requirement would increase substantially. A simulation such as that in Figure 17b typically required in the order of $10,000$ nodes, and so requiring approximately $20,000$ equations to be solved at each timestep in the independent variables h_i and q_i. Scaling this into a three-dimensional geometry and taking into account the additional independant variable for flux in the cross-stream direction indicates that a uniform mesh would be costly. An alternative would be to employ a variably mesh structure. Techniques such as radial basis function generated finite differences, as detailed by Flyer et al. [16], would be an option to overcoming some of the computational requirements of a static, uniform mesh as currently utilised.

The depth-averaged model proposed in this thesis, together with the finite difference numerical implementation, has been able to obtain solutions for an extended range of Reynolds numbers for which the thin-film approximation is valid. Variations of the initial mathematical model such as the characteristics of the fluid-plane interface, the assumed velocity profile and gravity-driven solitary waves, with shear selectively applied, were investigated in comparison with the initial set of wave structures observed. Across

all variations of the initial model, inertia was found to have an important, and in many cases significant effect on the evolution of wave structures.

A

ANALYTICAL JACOBIAN FORMULATION

As in Section 2.4, the Jacobian matrix for the system of equations to be solved is of the form

$$\mathbf{J} = \begin{pmatrix} \frac{\partial \mathcal{C}_1}{\partial h_1} & \cdots & \frac{\partial \mathcal{C}_1}{\partial h_{n-1}} & \frac{\partial \mathcal{C}_1}{\partial q_1} & \cdots & \frac{\partial \mathcal{C}_1}{\partial q_{n-1}} \\ \vdots & \ddots & \vdots & \vdots & \ddots & \vdots \\ \frac{\partial \mathcal{C}_{n-1}}{\partial h_1} & \cdots & \frac{\partial \mathcal{C}_{n-1}}{\partial h_{n-1}} & \frac{\partial \mathcal{C}_{n-1}}{\partial q_1} & \cdots & \frac{\partial \mathcal{C}_{n-1}}{\partial q_{n-1}} \\ \frac{\partial \mathcal{M}_1}{\partial h_1} & \cdots & \frac{\partial \mathcal{M}_1}{\partial h_{n-1}} & \frac{\partial \mathcal{M}_1}{\partial q_1} & \cdots & \frac{\partial \mathcal{M}_1}{\partial q_{n-1}} \\ \vdots & \ddots & \vdots & \vdots & \ddots & \vdots \\ \frac{\partial \mathcal{M}_{n-1}}{\partial h_1} & \cdots & \frac{\partial \mathcal{M}_{n-1}}{\partial h_{n-1}} & \frac{\partial \mathcal{M}_{n-1}}{\partial q_1} & \cdots & \frac{\partial \mathcal{M}_{n-1}}{\partial q_{n-1}} \end{pmatrix}. \tag{A.0.1}$$

$\mathcal{C}_i$ and $\mathcal{M}_i$ for $i = 1, \ldots, n-1$ refer to the discretised continuity and momentum equations respectively at the i^{th} node. These are given as

$$\mathcal{C}_i = \frac{\partial h}{\partial t}(x_i) + \frac{\partial q}{\partial x}(x_i) \tag{A.0.2}$$

and

$$\mathcal{M}_i = \mathrm{Re}^* \left(\frac{\partial q}{\partial t}(x_i) + I_{h,i} \frac{\partial h}{\partial x}(x_i) - I_{q,i} \frac{\partial h}{\partial t}(x_i) \right) + A_i \frac{\partial h}{\partial x}(x_i) + B_i + C_i \frac{\partial^3 h}{\partial x^3}(x_i). \tag{A.0.3}$$

A_i, B_i and C_i are groups of coefficients evaluated at the i^{th} node, defined as

$$\begin{aligned} A_i &= \varepsilon \lambda h_i \cos\theta, \\ B_i &= \lambda h_i \sin\theta - \tau + \left. \frac{\partial u}{\partial y} \right|_{y=0} (x_i), \\ C_i &= -\frac{\varepsilon^3}{\mathrm{Ca}} h_i. \end{aligned} \tag{A.0.4}$$

The discrete integral coefficients $I_{h,i}$ and $I_{q,i}$ depend upon the assumed velocity profile chosen to represent the flow in the longitudinal direction, as does the term $\frac{\partial u}{\partial y}(x_i)\Big|_{y=0}$. Upwinding on the term $I_{h,i}\frac{\partial h}{\partial x}(x_i)$ is variable, with $I_{h,i}$ taking either positive or negative values, and so will require two difference cases; A_i is always positive, assuming $h_i > 0$ and in line with the values of the other parameters considered, and therefore requires no variations of the formulation. The spatial derivative terms thus, further to the detail in Section 2.4.2, are given as

$$\begin{aligned}
I_{h,i}\frac{\partial h}{\partial x}(x_i) &= I_{h,i}\left(\frac{3h_i - 4h_{i-1} + h_{i-2}}{2\Delta x} + \mathcal{O}(\Delta x^2)\right) \quad \text{if} \quad I_{h,i} < 0, \\
I_{h,i}\frac{\partial h}{\partial x}(x_i) &= I_{h,i}\left(\frac{-h_{i+2} + 4h_{i+1} - 3h_i}{2\Delta x} + \mathcal{O}(\Delta x^2)\right) \quad \text{if} \quad I_{h,i} > 0, \\
\frac{\partial q}{\partial x}(x_i) &= \frac{-q_{i-1} + q_{i+1}}{2\Delta x}, \\
\frac{\partial^3 h}{\partial x^3}(x_i) &= \frac{h_{i-2} + 2h_{i-1} - 2h_{i+2} + h_{i+2}}{2\Delta x^3},
\end{aligned} \tag{A.0.5}$$

for interior nodes not affected directly by the boundary conditions. The temporal terms are discretised as

$$\begin{aligned}
\frac{\partial h}{\partial t} &= \frac{h^{k+1} - h^k}{\Delta t}, \\
\frac{\partial q}{\partial t} &= \frac{q^{k+1} - q^k}{\Delta t},
\end{aligned} \tag{A.0.6}$$

where the superscripts refer to terms evaluated at times t^{k+1} and t^k. Since an implicit Euler method is used, the remainder of the terms without a superscript are also evaluated at t^{k+1}.

Using the above definitions, the discrete derivatives of (A.0.2)-(A.0.3) can be written as required for the Jacobian matrix (A.0.1). The full formulations are given below, with any unspecified entries of the matrix assumed to be zero.

$$\frac{\partial \mathcal{C}_i}{\partial h_i} = \frac{1}{\Delta t} \qquad \text{for} \quad i = 1, \ldots, n-1. \tag{A.0.7}$$

$$
\begin{aligned}
\frac{\partial \mathcal{C}_1}{\partial q_1} &= -\frac{2}{3\Delta x}, \\
\frac{\partial \mathcal{C}_1}{\partial q_2} &= \frac{2}{3\Delta x}, \\
\left\{ \frac{\partial \mathcal{C}_i}{\partial q_{i-1}} \right. &= -\frac{1}{2\Delta x}, \\
\left. \frac{\partial \mathcal{C}_i}{\partial q_{i+1}} \right\} &= \frac{1}{2\Delta x} \qquad \text{for} \quad i = 2, \ldots, n-2, \\
\frac{\partial \mathcal{C}_n - 1}{\partial q_{n-2}} &= -\frac{1}{2\Delta x}.
\end{aligned}
\tag{A.0.8}
$$

Note that for simplicity, the notation used here is $\frac{\partial h}{\partial t}(x_i) = \frac{\partial h}{\partial t}_i$, and similarly for spatial derivatives. If $I_{h,i} > 0$

$$
\begin{aligned}
\frac{\partial \mathcal{M}_1}{\partial h_1} &= \mathrm{Re}^* \left(-\frac{\partial I_{q,1}}{\partial h_1}\frac{\partial h}{\partial t}_1 - \frac{1}{\Delta t} I_{q,1} + \frac{\partial I_{h,1}}{\partial h_1}\frac{\partial h}{\partial x}^+_1 + \frac{2}{\Delta x} I_{h,1} \right) \\
&\quad + \frac{\partial A_1}{\partial h_1}\frac{\partial h}{\partial x}^+_1 + \frac{2}{\Delta x} A_1 + \frac{\partial B_1}{\partial h_1} + \frac{\partial C_1}{\partial h_1}\frac{\partial^3 h}{\partial x^3}_1 - \frac{1}{2\Delta x^3} C_1, \\
\frac{\partial \mathcal{M}_1}{\partial h_2} &= -\frac{1}{\Delta x^3} C_1, \\
\frac{\partial \mathcal{M}_1}{\partial h_3} &= \frac{1}{2\Delta x^3} C_1, \\
\frac{\partial \mathcal{M}_2}{\partial h_1} &= -\frac{2}{\Delta x}\,\mathrm{Re}^*\, I_{h,2} - \frac{2}{\Delta x} A_2 + \frac{1}{\Delta x^3} C_2, \\
\frac{\partial \mathcal{M}_2}{\partial h_2} &= \mathrm{Re}^* \left(-\frac{\partial I_{q,2}}{\partial h_2}\frac{\partial h}{\partial t}_2 - \frac{1}{\Delta t} I_{q,2} + \frac{\partial I_{h,2}}{\partial h_2}\frac{\partial h}{\partial x}^+_2 + \frac{3}{2\Delta x} I_{h,2} \right) \\
&\quad + \frac{\partial A_2}{\partial h_2}\frac{\partial h}{\partial x}^+_2 + \frac{3}{2\Delta x} A_2 + \frac{\partial B_2}{\partial h_2} + \frac{\partial C_2}{\partial h_2}\frac{\partial^3 h}{\partial x^3}_2, \\
\frac{\partial \mathcal{M}_2}{\partial h_3} &= -\frac{1}{\Delta x^3} C_2, \\
\frac{\partial \mathcal{M}_2}{\partial h_4} &= \frac{1}{2\Delta x^3} C_2, \\
\left\{ \frac{\partial \mathcal{M}_i}{\partial h_i - 2} \right. &= \frac{1}{2\Delta x}\,\mathrm{Re}^*\, I_{h,i} + \frac{1}{2\Delta x} A_i - \frac{1}{2\Delta x^3} C_i, \\
\frac{\partial \mathcal{M}_i}{\partial h_{i-1}} &= -\frac{2}{\Delta x}\,\mathrm{Re}^*\, I_{h,i} - \frac{2}{\Delta x} A_i + \frac{1}{\Delta x^3} C_i, \\
\frac{\partial \mathcal{M}_i}{\partial h_i} &= \mathrm{Re}^* \left(-\frac{\partial I_{q,i}}{\partial h_i}\frac{\partial h}{\partial t}_i - \frac{1}{\Delta t} I_{q,i} + \frac{\partial I_{h,i}}{\partial h_i}\frac{\partial h}{\partial x}^+_i + \frac{3}{2\Delta x} I_{h,i} \right) \\
&\quad + \frac{\partial A_i}{\partial h_i}\frac{\partial h}{\partial x}^+_i + \frac{3}{2\Delta x} A_i + \frac{\partial B_i}{\partial h_i} + \frac{\partial C_i}{\partial h_i}\frac{\partial^3 h}{\partial x^3}_i, \\
\frac{\partial \mathcal{M}_i}{\partial h_{i+1}} &= -\frac{1}{\Delta x^3} C_i, \\
\frac{\partial \mathcal{M}_i}{\partial h_{i+2}} &= \frac{1}{2\Delta x^3} C_i \Bigg\} \qquad \text{for} \quad i = 3, \ldots, n-3, \\
\frac{\partial \mathcal{M}_{n-2}}{\partial h_{n-4}} &= \frac{1}{2\Delta x}\,\mathrm{Re}^*\, I_{h,n-2} + \frac{1}{2\Delta x} A_{n-2} - \frac{1}{2\Delta x^3} C_{n-2}, \\
\frac{\partial \mathcal{M}_{n-2}}{\partial h_{n-3}} &= -\frac{2}{\Delta x}\,\mathrm{Re}^*\, I_{h,n-2} - \frac{2}{\Delta x} A_{n-2} + \frac{1}{\Delta x^3} C_{n-2}, \\
\frac{\partial \mathcal{M}_{n-2}}{\partial h_{n-2}} &= \mathrm{Re}^* \left(-\frac{\partial I_{q,n-2}}{\partial h_{n-2}}\frac{\partial h}{\partial t}_{n-2} - \frac{1}{\Delta t} I_{q,n-2} + \frac{\partial I_{h,n-2}}{\partial h_{n-2}}\frac{\partial h}{\partial x}^+_{n-2}, + \frac{3}{2\Delta x} I_{h,n-2} \right) \\
&\quad + \frac{\partial A_{n-2}}{\partial h_{n-2}}\frac{\partial h}{\partial x}^+_{n-2} + \frac{3}{2\Delta x} A_{n-2} + \frac{\partial B_{n-2}}{\partial h_{n-2}} + \frac{\partial C_{n-2}}{\partial h_{n-2}}\frac{\partial^3 h}{\partial x^3}_{n-2} - \frac{1}{6\Delta x^3} C_{n-2}, \\
\frac{\partial \mathcal{M}_{n-2}}{\partial h_{n-1}} &= -\frac{1}{3\Delta x^3} C_{n-2},
\end{aligned}
$$

$$
\begin{aligned}
\frac{\partial \mathcal{M}_{n-1}}{\partial h_{n-3}} &= \frac{1}{2\Delta x}\,\mathrm{Re}^*\, I_{h,n-1} + \frac{1}{2\Delta x} A_{n-1} - \frac{1}{2\Delta x^3} C_{n-1},\\
\frac{\partial \mathcal{M}_{n-1}}{\partial h_{n-2}} &= -\frac{2}{\Delta x}\,\mathrm{Re}^*\, I_{h,n-1} - \frac{2}{\Delta x} A_{n-1} + \frac{7}{6\Delta x^3} C_{n-1},\\
\frac{\partial \mathcal{M}_{n-1}}{\partial h_{n-1}} &= \mathrm{Re}^* \left(-\frac{\partial I_{q,n-1}}{\partial h_{n-1}} \frac{\partial h}{\partial t}_{n-1} - \frac{1}{\Delta t} I_{q,n-1} + \frac{\partial I_{h,n-1}}{\partial h_{n-1}} \frac{\partial h}{\partial x}^{+}_{n-1} + \frac{3}{2\Delta x} I_{h,n-1} \right)\\
&\quad + \frac{\partial A_{n-1}}{\partial h_{n-1}} \frac{\partial h}{\partial x}^{+}_{n-1} + \frac{3}{2\Delta x} A_{n-1} + \frac{\partial B_{n-1}}{\partial h_{n-1}} + \frac{\partial C_{n-1}}{\partial h_{n-1}} \frac{\partial^3 h}{\partial x^3}_{n-1} - \frac{2}{3\Delta x^3} C_{n-1}.
\end{aligned}
\tag{A.0.9}
$$

$$
\frac{\partial \mathcal{M}_i}{\partial q_i} = \mathrm{Re}^* \left(\frac{1}{\Delta t} - \frac{\partial I_{q,i}}{\partial q_i} \frac{\partial h}{\partial t}_{i} + \frac{\partial I_{h,i}}{\partial q_i} \frac{\partial h}{\partial x}^{+}_{i} \right) + \frac{\partial B_i}{\partial q_i} \qquad \text{for} \quad i = 1, \ldots, n-1.
\tag{A.0.10}
$$

If $I_{h,i} < 0$

$$
\begin{aligned}
\frac{\partial \mathcal{M}_1}{\partial h_1} &= \mathrm{Re}^* \left(-\frac{\partial I_{q,1}}{\partial h_1} \frac{\partial h}{\partial t}_1 - \frac{1}{\Delta t} I_{q,1} + \frac{\partial I_{h,1}}{\partial h_1} \frac{\partial h}{\partial x}_1^- - \frac{3}{2\Delta x} I_{h,1} \right) \\
&\quad + \frac{\partial A_1}{\partial h_1} \frac{\partial h}{\partial x}_1^+ + \frac{2}{\Delta x} A_1 + \frac{\partial B_1}{\partial h_1} + \frac{\partial C_1}{\partial h_1} \frac{\partial^3 h}{\partial x^3}_1 - \frac{1}{2\Delta x^3} C_1, \\
\frac{\partial \mathcal{M}_1}{\partial h_2} &= \frac{2}{\Delta x} \mathrm{Re}^* \, I_{h,1} - \frac{1}{\Delta x^3} C_1, \\
\frac{\partial \mathcal{M}_1}{\partial h_3} &= -\frac{1}{2\Delta x} \mathrm{Re}^* \, I_{h,1} + \frac{1}{2\Delta x^3} C_1, \\
\frac{\partial \mathcal{M}_2}{\partial h_1} &= -\frac{2}{\Delta x} A_2 + \frac{1}{\Delta x^3} C_2, \\
\frac{\partial \mathcal{M}_2}{\partial h_2} &= \mathrm{Re}^* \left(-\frac{\partial I_{q,2}}{\partial h_2} \frac{\partial h}{\partial t}_2 - \frac{1}{\Delta t} I_{q,2} + \frac{\partial I_{h,2}}{\partial h_2} \frac{\partial h}{\partial x}_2^- - \frac{3}{2\Delta x} I_{h,2} \right) \\
&\quad + \frac{\partial A_2}{\partial h_2} \frac{\partial h}{\partial x}_2^+ + \frac{3}{2\Delta x} A_2 + \frac{\partial B_2}{\partial h_2} + \frac{\partial C_2}{\partial h_2} \frac{\partial^3 h}{\partial x^3}_2, \\
\frac{\partial \mathcal{M}_2}{\partial h_3} &= \frac{2}{\Delta x} \mathrm{Re}^* \, I_{h,2} - \frac{1}{\Delta x^3} C_2, \\
\frac{\partial \mathcal{M}_2}{\partial h_4} &= -\frac{1}{2\Delta x} \mathrm{Re}^* \, I_{h,2} + \frac{1}{2\Delta x^3} C_2, \\
\left\{ \frac{\partial \mathcal{M}_i}{\partial h_i - 2} \right. &= \frac{1}{2\Delta x} A_i - \frac{1}{2\Delta x^3} C_i, \\
\frac{\partial \mathcal{M}_i}{\partial h_{i-1}} &= -\frac{2}{\Delta x} A_i + \frac{1}{\Delta x^3} C_i, \\
\frac{\partial \mathcal{M}_i}{\partial h_i} &= \mathrm{Re}^* \left(-\frac{\partial I_{q,i}}{\partial h_i} \frac{\partial h}{\partial t}_i - \frac{1}{\Delta t} I_{q,i} + \frac{\partial I_{h,i}}{\partial h_i} \frac{\partial h}{\partial x}_i^- - \frac{3}{2\Delta x} I_{h,i} \right) \\
&\quad + \frac{\partial A_i}{\partial h_i} \frac{\partial h}{\partial x}_i^+ + \frac{3}{2\Delta x} A_i + \frac{\partial B_i}{\partial h_i} + \frac{\partial C_i}{\partial h_i} \frac{\partial^3 h}{\partial x^3}_i, \\
\frac{\partial \mathcal{M}_i}{\partial h_{i+1}} &= \frac{2}{\Delta x} \mathrm{Re}^* \, I_{h,i} - \frac{1}{\Delta x^3} C_i, \\
\left. \frac{\partial \mathcal{M}_i}{\partial h_{i+2}} \right. &= \frac{1}{2\Delta x} \mathrm{Re}^* \, I_{h,i} + \frac{1}{2\Delta x^3} C_i \Big\} \qquad \text{for} \quad i = 3, \ldots, n-3, \\
\frac{\partial \mathcal{M}_{n-2}}{\partial h_{n-4}} &= \frac{1}{2\Delta x} A_{n-2} - \frac{1}{2\Delta x^3} C_{n-2}, \\
\frac{\partial \mathcal{M}_{n-2}}{\partial h_{n-3}} &= -\frac{2}{\Delta x} A_{n-2} + \frac{1}{\Delta x^3} C_{n-2}, \\
\frac{\partial \mathcal{M}_{n-2}}{\partial h_{n-2}} &= \mathrm{Re}^* \left(-\frac{\partial I_{q,n-2}}{\partial h_{n-2}} \frac{\partial h}{\partial t}_{n-2} - \frac{1}{\Delta t} I_{q,n-2} + \frac{\partial I_{h,n-2}}{\partial h_{n-2}} \frac{\partial h}{\partial x}_{n-2}^- - \frac{4}{3\Delta x} I_{h,n-2} \right) \\
&\quad + \frac{\partial A_{n-2}}{\partial h_{n-2}} \frac{\partial h}{\partial x}_{n-2}^+ + \frac{3}{2\Delta x} A_{n-2} + \frac{\partial B_{n-2}}{\partial h_{n-2}} + \frac{\partial C_{n-2}}{\partial h_{n-2}} \frac{\partial^3 h}{\partial x^3}_{n-2} - \frac{1}{6\Delta x^3} C_{n-2}, \\
\frac{\partial \mathcal{M}_{n-2}}{\partial h_{n-1}} &= \frac{4}{3\Delta x} \mathrm{Re}^* \, I_{h,n-2} - \frac{1}{3\Delta x^3} C_{n-2},
\end{aligned}
$$

$$
\begin{aligned}
\frac{\partial \mathcal{M}_{n-1}}{\partial h_{n-3}} &= \frac{1}{2\Delta x} A_{n-1} - \frac{1}{2\Delta x^3} C_{n-1}, \\
\frac{\partial \mathcal{M}_{n-1}}{\partial h_{n-2}} &= -\frac{1}{2\Delta x} \operatorname{Re}^* I_{h,n-1} - \frac{2}{\Delta x} A_{n-1} + \frac{7}{6\Delta x^3} C_{n-1}, \\
\frac{\partial \mathcal{M}_{n-1}}{\partial h_{n-1}} &= \operatorname{Re}^* \left(-\frac{\partial I_{q,n-1}}{\partial h_{n-1}} \frac{\partial h}{\partial t}_{n-1} - \frac{1}{\Delta t} I_{q,n-1} + \frac{\partial I_{h,n-1}}{\partial h_{n-1}} \frac{\partial h}{\partial x}^{-}_{n-1} + \frac{1}{2\Delta x} I_{h,n-1} \right) \\
&\quad + \frac{\partial A_{n-1}}{\partial h_{n-1}} \frac{\partial h}{\partial x}^{+}_{n-1} + \frac{3}{2\Delta x} A_{n-1} + \frac{\partial B_{n-1}}{\partial h_{n-1}} + \frac{\partial C_{n-1}}{\partial h_{n-1}} \frac{\partial^3 h}{\partial x^3}_{n-1} - \frac{2}{3\Delta x^3} C_{n-1}.
\end{aligned}
\tag{A.0.11}
$$

$$
\frac{\partial \mathcal{M}_i}{\partial q_i} = \operatorname{Re}^* \left(\frac{1}{\Delta t} - \frac{\partial I_{q,i}}{\partial q_i} \frac{\partial h}{\partial t}_{i} + \frac{\partial I_{h,i}}{\partial q_i} \frac{\partial h}{\partial x}^{-}_{i} \right) + \frac{\partial B_i}{\partial q_i} \qquad \text{for} \quad i = 1, \ldots, n-1.
\tag{A.0.12}
$$

BIBLIOGRAPHY

[1] Alekseenko, S.V., Nakoryakov, V.Y. and Pokusaev, B.G., 1985. *Wave formation on a vertical falling liquid film.* AIChE Journal, 31(9), pp.1446-1460.

[2] Alves, M.A., Oliveira, P.J. and Pinho, F.T., 2003. *A convergent and universally bounded interpolation scheme for the treatment of advection.* International Journal for Numerical Methods in Fluids, 41(1), pp.47-75.

[3] Bailey, N.Y., Cliffe, K.A., Hibberd, S. and Power, H., 2014. *Dynamics of a parallel, high-speed, lubricated thrust bearing with Navier slip boundary conditions.* IMA Journal of Applied Mathematics, p.hxu053.

[4] Benilov, E.S., 2014. *Depth-averaged model for hydraulic jumps on an inclined plate.* Physical Review E, 89(5), p.053013.

[5] Benny, D.J., 1966. *Long waves in liquid film.* J. Math and Phys, 45, pp.150-155.

[6] Bertozzi, A.L., Münch, A. and Shearer, M., 1999. *Undercompressive shocks in thin film flows.* Physica D: Nonlinear Phenomena, 134(4), pp.431-464.

[7] Broyden, C.G., 1965. *A class of methods for solving nonlinear simultaneous equations.* Mathematics of Computation, 19(92), pp.577-593.

[8] Chang, H.C., 1987. *Evolution of nonlinear waves on vertically falling films—a normal form analysis.* Chemical Engineering Science, 42(3), pp.515-533.

[9] Chang, H., 1994. *Wave evolution on a falling film.* Annual Review of Fluid Mechanics, 26(1), pp.103-136.

[10] Chang, H.C., Demekhin, E.A. and Saprikin, S.S., 2002. *Noise-driven wave transitions on a vertically falling film.* Journal of Fluid Mechanics, 462, pp.255-283.

[11] Guoding, C., Hengchao, S.U.N. and Jun, W., 2011. *Research into configuration and flow of wall oil film in bearing chamber based on droplet size distribution.* Chinese Journal of Aeronautics, 24(3), pp.355-362.

[12] L. Chen, 2006. *Finite difference methods.* [online] Available at: https://www.math.uci.edu/ chenlong/226/FDM.pdf.

[13] Cheng, M. and Chang, H.C., 1995. Competition between subharmonic and sideband secondary instabilities on a falling film. Physics of Fluids (1994-present), 7(1), pp.34-54.

[14] Craster, R.V. and Matar, O.K., 2009. *Dynamics and stability of thin liquid films.* Reviews of modern physics, 81(3), p.1131.

[15] Dietze, G.F., Leefken, A. and Kneer, R., 2008. *Investigation of the backflow phenomenon in falling liquid films.* Journal of Fluid Mechanics, 595, pp.435-459.

[16] Flyer, N., Lehto, E., Blaise, S., Wright, G.B. and St-Cyr, A., 2012. *A guide to RBF-generated finite differences for nonlinear transport: Shallow water simulations on a sphere.* Journal of Computational Physics, 231(11), pp.4078-4095.

[17] Fornberg, B., 1988. *Generation of finite difference formulas on arbitrarily spaced grids.* Mathematics of computation, 51(184), pp.699-706.

[18] Gatapova, E.Y. and Kabov, O.A., 2008. *Shear-driven flows of locally heated liquid films.* International Journal of Heat and Mass Transfer, 51(19), pp.4797-4810.

[19] Gjevik, B., 1970. *Occurrence of Finite-Amplitude Surface Waves on Falling Liquid Films.* Physics of Fluids, 13(8), pp.1918-1925.

[20] Gorse, P., Busam, S. and Dullenkopf, K., 2006. *Influence of operating condition and geometry on the oil film thickness in aeroengine bearing chambers.* Journal of Engineering for Gas Turbines and Power, 128(1), pp.103-110.

[21] Jahn, I.H., 2012. *Shear driven films inside cylinders.* In Proceedings of the 18th Australasian Fluid Mechanics Conference, pp.549-552.

[22] Kandel, H.N. and Pascal, J.P., 2013. *Inclined fluid-film flow with bottom filtration.* Physical Review E, 88(5), p.052405.

[23] Kay, E.D., Hibberd, S. and Power, H., 2013. *Inertial effects at moderate Reynolds number in thin-film rimming flows driven by surface shear.* Physics of Fluids, 25(10), p.102108.

[24] Kay, E.D., 2013. *A depth-averaged model for non-isothermal rimming flow driven at the surface by droplet impact.* (Doctoral dissertation, University of Nottingham).

[25] Kay, E.D., Hibberd, S. and Power, H., 2015. *Non-isothermal rimming flow with the effects of surface shear and droplet impact.* Physics of Fluids, 27(12), p.122105.

[26] Kofman, N., Mergui, S. and Ruyer-Quil, C., 2014. *Three-dimensional instabilities of quasi-solitary waves in a falling liquid film.* Journal of Fluid Mechanics, 757, pp.854-887.

[27] Kondic, L., 2003. *Instabilities in gravity driven flow of thin fluid films.* SIAM Review, 45(1), pp.95-115.

[28] Levy, R. and Shearer, M., 2005. *Kinetics and nucleation for driven thin film flow.* Physica D: Nonlinear Phenomena, 209(1), pp.145-163.

[29] Liu, J. and Gollub, J.P., 1994. *Solitary wave dynamics of film flows.* Physics of Fluids, 6(5), pp.1702-1712.

[30] Liu, R. and Liu, Q., 2009. *Instabilities of a liquid film flowing down an inclined porous plane.* Physical Review E, 80(3), p.036316.

[31] Longuet-Higgins, M.S. and Cokelet, E.D., 1976, July. *The deformation of steep surface waves on water. I. A numerical method of computation.* In Proceedings of the Royal Society of London A: Mathematical, Physical and Engineering Sciences (Vol. 350, No. 1660, pp. 1-26). The Royal Society.

[32] Malamataris, N.A., Vlachogiannis, M. and Bontozoglou, V., 2002. *Solitary waves on inclined films: Flow structure and binary interactions.* Physics of Fluids, 14(3), pp.1082-1094.

[33] Münch, A., 2002. *The thickness of a Marangoni-driven thin liquid film emerging from a meniscus.* SIAM Journal on Applied Mathematics, 62(6), pp.2045-2063.

[34] Nguyen, L.T. and Balakotaiah, V., 2000. *Modeling and experimental studies of wave evolution on free falling viscous films.* Physics of Fluids, 12(9), pp.2236-2256.

[35] O'brien, S.B.G. and Schwartz, L.W., 2002. *Theory and modeling of thin film flows.* Encyclopedia of Surface and Colloid Science, 5283.

[36] Oliveira, P.J., Pinho, F.T.D. and Pinto, G.A., 1998. *Numerical simulation of non-linear elastic flows with a general collocated finite-volume method.* Journal of Non-Newtonian Fluid Mechanics, 79(1), pp.1-43.

[37] Pascal, J.P., 1999. *Linear stability of fluid flow down a porous inclined plane.* Journal of Physics D: Applied Physics, 32(4), p.417.

[38] Prokopiou, T., Cheng, M. and Chang, H.C., 1991. *Long waves on inclined films at high Reynolds number.* Journal of fluid mechanics, 222, pp.665-691.

[39] Pumir, A., Manneville, P. and Pomeau, Y., 1983. *On solitary waves running down an inclined plane.* Journal of Fluid Mechanics, 135, pp.27-50.

[40] Ruyer-Quil, C. and Manneville, P., 1998. *Modeling film flows down inclined planes.* The European Physical Journal B-Condensed Matter and Complex Systems, 6(2), pp.277-292.

[41] Ruyer-Quil, C. and Manneville, P., 2000. *Improved modeling of flows down inclined planes.* The European Physical Journal B-Condensed Matter and Complex Systems, 15(2), pp.357-369.

[42] Sadiq, I.M.R. and Usha, R., 2008. *Thin Newtonian film flow down a porous inclined plane: stability analysis.* Physics of Fluids, 20(2), p.022105.

[43] Samanta, A., 2014. *Shear-imposed falling film.* Journal of Fluid Mechanics, 753, pp.131-149.

[44] Samanta, A., Goyeau, B. and Ruyer-Quil, C., 2013. *A falling film on a porous medium.* Journal of Fluid Mechanics, 716, pp.414-444.

[45] Samanta, A., Ruyer-Quil, C. and Goyeau, B., 2011. *A falling film down a slippery inclined plane.* Journal of Fluid Mechanics, 684, pp.353-383.

[46] Scheid, B., Ruyer-Quil, C., Thiele, U., Kabov, O.A., Legros, J.C. and Colinet, P., 2005. *Validity domain of the Benney equation including the Marangoni effect for closed and open flows.* Journal of Fluid Mechanics, 527, pp.303-335.

[47] Scheid, B., Ruyer-Quil, C. and Manneville, P., 2006. *Wave patterns in film flows: modelling and three-dimensional waves.* Journal of Fluid Mechanics, 562, pp.183-222.

[48] Shkadov, V.Y., 1967. *Wave flow regimes of a thin layer of viscous fluid subject to gravity.* Fluid Dynamics, 2(1), pp.29-34.

[49] Shuaib, N.H., Power, H., Hibberd, S. and Simmons, K., 2006. *A numerical study of wave structures developed on the free surface of a film flowing on inclined planes and subjected to surface shear.* International Journal for Numerical Methods in Engineering, 68(7), pp.755-789.

[50] Sivapuratharasu, M., Hibberd, S., Hubbard, M.E. and Power, H., 2016. *Inertial effects on thin-film wave structures with imposed surface shear on an inclined plane.* Physica D: Nonlinear Phenomena, 325, pp.86-97.

[51] Tihon, J., Serifi, K., Argyriadi, K. and Bontozoglou, V., 2006. *Solitary waves on inclined films: their characteristics and the effects on wall shear stress.* Experiments in Fluids, 41(1), pp.79-89.

[52] Thoroddsen, S.T. and Mahadevan, L., 1996. *Shark-teeth pattern in coating flow inside a horizontally rotating cylinder.* Physics of Fluids (1994-present), 8(9), pp.S10-S10.

[53] Tushkanov, D.A. and Shkadov, V.Y., 2006. *Nonlinear waves in a liquid film on a near-horizontal surface.* Fluid Dynamics, 41(3), pp.330-342.

[54] Usha, R. and Millet, S., 2013. *Thin film flow down a porous substrate in the presence of an insoluble surfactant: Stability analysis.* Physics of Fluids, 25(2), p.022101.

[55] Weinstein, S.J. and Ruschak, K.J., 2004. *Coating flows.* Annual Review of Fluid Mechanics, 36, pp.29-53.

[56] Williams, J., 2009. *Thin film rimming flow subject to droplet impact at the surface* (Doctoral dissertation, University of Nottingham).

[57] Yu, L.Q., Wasden, F.K., Dukler, A.E. and Balakotaiah, V., 1995. *Nonlinear evolution of waves on falling films at high Reynolds numbers.* Physics of Fluids (1994-present), 7(8), pp.1886-1902.